Mean flow analysis and pressure evaluation by means of PIV in transonic baseflow

Yang Yue

December 13th, 2012

Master of Science Thesis

TU Delft Delft University of Technology

Mean flow analysis and pressure evaluation by means of PIV in transonic baseflow

Master of Science Thesis

For the degree of Master of Science in Aerodynamics at Delft University of Technology

Yang Yue

December 13, 2012

Faculty of Aerospace Engineering (AE) · Delft University of Technology

Delft University of Technology
Department of
Aerodynamics

The undersigned hereby certify that they have read and recommend to the Faculty of Aerospace Engineering (AE) for acceptance a thesis entitled

Mean flow analysis and pressure evaluation by means of PIV in transonic baseflow

by

Yang Yue

in partial fulfillment of the requirements for the degree of

Master of Science Aerodynamics

Dated: December 13, 2012

Supervisor(s):

dr.ir. F.F.J. Schrijer

K.P. Lynch, MSc

Reader(s):

prof.dr.ir. F. Scarano

dr.ir. B.W. van Oudheusden

Abstract

During atmospheric ascent, flow separation at the base of launch vehicles gives rise to aerodynamic buffeting across the surface of the nozzle (baseflow buffeting). As a result the nozzle experiences fluctuating loads that cause large bending moments which need to be accounted for during its design. Baseflow buffeting prevents the use of new more efficient nozzle designs. Hence current research is geared towards gaining a better understanding of the phenomenon so that an effective means of reducing the intensity of buffeting can be developed. In order to contribute to the ongoing research the current project explores the potential of studying baseflow with a newly emerging technique which attempts to evaluate pressure from PIV data.

The aim of this project is first to characterize the mean velocity field in the wake of a typical rocket base in transonic flow using Particle Image Velocimetry (PIV). Then the possibilities will be explored of utilizing the obtained PIV data to evaluate the pressure field. The wind tunnel experiments are carried out on a model rocket at Mach 0.7. The Reynolds number based on the diameter of the model is equal to $Re_D = 1.3 \cdot 10^6$. Furthermore, three test configuration of the model base are considered: a) blunt base, b) afterbody extending up to $L/D = 1.2$, c) afterbody extending up to $L/D = 2.0$. The mean velocity fields obtained from the PIV experiment show good agreement with literature. The mean reattachment point of the free shear layer appears to be at $x/D \approx 1$ and the maximum backflow velocity reaches $35\% - 40\%$ of the free stream velocity. In addition the secondary corner vortex can be discerned in the data. Previous studies carried out at TU Delft were unable to discover this secondary vortex. The current project however has confirmed the existence of the phenomenon.

In addition to characterizing the mean velocity field, the corresponding pressure field is computed numerically using the PIV data as input. A Poisson formulation for the pressure in terms of velocity is derived from the Reynolds averaged Navier-Stokes equations. This is solved using a numerical Poisson solver which uses PIV data to provide all the velocity terms. The results are validated with data obtained from pressure ports on the model as well as CFD solutions of Deck and Thorigny [2007] and Weiss et al. [2009]. Good agreement between the results is found. The maximum difference in C_p between the current results and the CFD data occurs in the center of the recirculation zone and is found to be 17% with respect to the

total C_p range in the wake. Between the solution generated by the Poisson solver and the pressure port data a maximum difference of 12% is observed.

The outcome of the experiments suggests that the current approach of evaluating pressure with PIV data is a good alternative to either a purely numerical or experimental study and that it can be applied to highly turbulent compressible flows with good results . The advantages of this approach over a CFD study is that input data is obtained from an actual physical measurement and the relative ease of changing variables and configurations in between experiments. Compared to traditional experimental methods for pressure measurements such as pressure ports, the advantage is that instead of the pressure only being determined at specific locations on the model surface, a complete pressure field is obtained at once. Furthermore the advantage over a pitot probe or rake is evidently that the technique is non-intrusive. A natural follow-up to the project would be to attempt obtaining instantaneous pressure fields with PIV. The ability to resolve instantaneous pressure fields can aid us in gaining new insights concerning the dynamic behavior of the flow. As a result perhaps more targeted attempts can then be made to reduce the buffeting loads occurring at the base of a launch vehicles.

Table of Contents

List of Figures

List of Tables

Preface

The present work embodies the final result of my graduation project carried out in the Aerodynamics Department at the Faculty of Aerospace Engineering. In Chapter 1 the reader is introduced to the thesis topic centered around transonic baseflow. We will take a brief look at recent history to uncover the event that initiated the research into a certain phenomenon which ultimately lead to the writing of this thesis. Chapter 2 provides an overview of the most important findings over the decades that have added to our understanding of transonic baseflow. Chapter 3 discusses the working principles of the experimental techniques used during the project. Chapter 4 continues with a description of the experimental apparatus used and how the experiments were set up. The results obtained from the experiments are analyzed and discussed in the following chapters. While in Chapter 5 the main focus is placed on characterizing the velocity field, Chapter 6 deals with the evaluation of the pressure. Finally the conclusions of the project are presented in Chapter 7 as well as some recommendations for future research.

Furthermore I would like to take this opportunity to acknowledge the people who have helped me and contributed to this thesis one way or another.

First and foremost I would like to thank my supervisors Ferry Schrijer and Kyle Lynch who were always readily available for advice and guidance during the project. Ferry, you have done a wonderful job in guiding me through this whole process, providing me with lots of feedback and suggestions, which is something I really appreciate. Kyle, we spent quite some time at the wind tunnel tinkering with the equipment and I learned a lot from you. Thank you for all your energy and optimism which kept me going even when the experiments did not always go as smoothly as one might hope for. I hope you will continue working with the same drive as you have shown while supervising me and wish you all the best with the remainder of your PhD.

In addition I would like to express my gratitude towards the technicians who were of great help in making the experiments possible: Eric de Keizer who is always capable of throwing in a couple of jokes to lighten the mood. Frits Donker Duyvis who has a knack for finding missing tools and equipment. Peter Duyndam who is so approachable and always carried out my requests on short notice. And Nico van Beek the department's IT guy.

I would also like to thank Bas van Oudheusden and Daniele Ragni for the advice they have given me on implementing the pressure computation algorithm. Fulvio Scarano for the occasional nudge in the right direction when he saw me frowning at my acquired data in the wind

tunnel control room. And Rogier Giepman, who at the time was working with the ST-15 next door, for the pleasant chatter as well as interesting discussions in between our own wind tunnel runs.

Finally I thank my family and my girlfriend Penelope for their boundless love and support.

These final months of being a student have turned out to be quite memorable to me. In writing this thesis I have experienced all sorts of feelings ranging from general excitement to utter frustration and at times downright confusion. But the feeling that prevails at the end of it all is that I can look back with a smile as I reflect on everything I have learned from this whole experience and the people around me.

Chapter 1

Motivation

The research for this thesis is performed in the context of a phenomenon known as 'aerodynamic buffeting'. In this very first chapter the reader is introduced to the phenomenon and the accompanying engineering problems as well as shown how these things relate to the current project. Furthermore the project is described and at the end of the chapter the goals are defined.

1.1 Historical background

Figure 1.1: Photo of a Junkers F13, the world's first all-metal passenger aircraft, manufactured in Germany after World War I *(Courtesy of 1000aircraftphotos.com)*.

On July 21, 1930 a Junkers F13 commercial airplane (Figure 1.1) with on-board two pilots and four passengers mysteriously crashed in Meopham, England. Eyewitnesses reported hearing a sound like an explosion and after looking up seeing the airplane fall apart before hitting the ground. The crew and passengers were all killed. The following investigation into the exact cause of the accident led to the discovery of a phenomenon that was termed (aerodynamic)

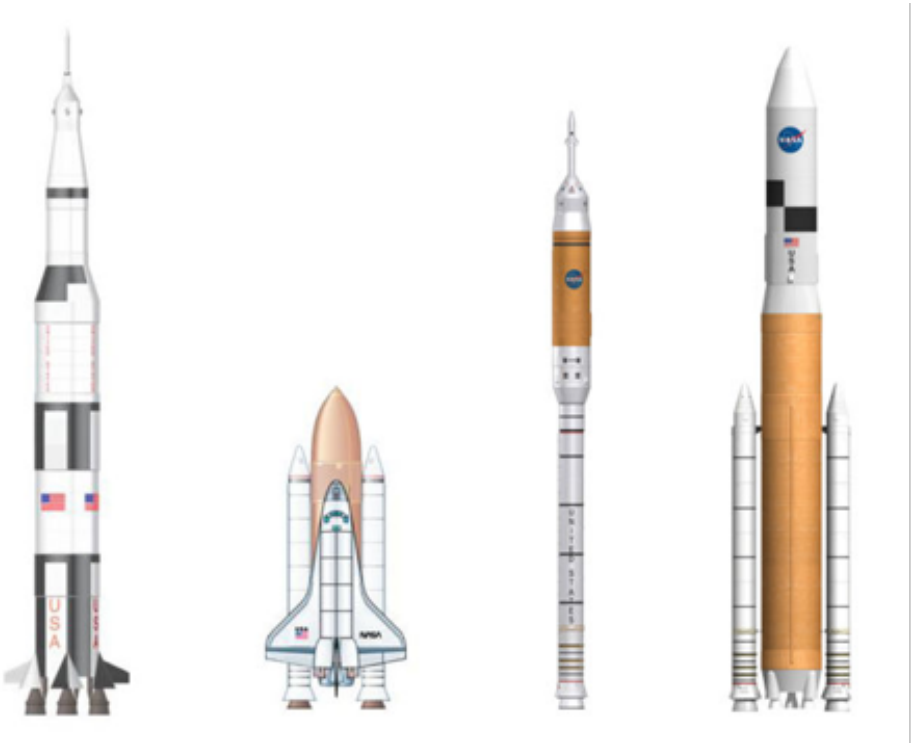

Figure 1.2: Several NASA launchers (from left to right): Saturn V, Space Shuttle and the proposed Ares I and Ares V *(Courtesy of NASA)*.

'buffeting' by the British Aeronautical Research Committee. Historically, this was the first instance to which the usage of the term can be tracked (Fung [2002]). Buffeting is defined as the repeated loading of a structure by an unsteady aerodynamic flow and generally it is associated with separation of the boundary layer and the subsequent transition to turbulent flow (Cole et al. [1970]). Under certain circumstances it can excite structural resonances that lead to structural failure as was the case in the Meopham accident. Ever since that event, the buffeting problem was something that airplane designers had to cope with. Although it was originally discovered in the aeronautics field, space engineers encountered similar problems at the dawn of the spaceflight era. It appeared that launch vehicles were also capable of experiencing buffet loads in the transonic portion of their flight regime in the lower atmosphere. The buffeting problem led to a series of launch vehicles failures because the phenomenon had been overlooked in the design of those early vehicles Rainey [1965]. Even though launch vehicles are generally long, slender configurations, they often exhibit local variations in cross-sectional area that can be quite abrupt which encourages flow separation(Figure 1.2). Hence during flight these geometric features on the launch vehicle can cause unsteady flow separation, which in turn is responsible for the buffeting phenomenon. For instance at the base of the launcher where the engine nozzle is located, it is very difficult to avoid flow separation. The resulting buffet loads manifest themselves as dynamic pressure fluctuations acting on the surface of the nozzle. These side loads can cause large bending moments to the nozzle.

Already in the early 1960's when the buffeting problem on launchers had just been recognized, research indicated that the nature of buffeting was highly configuration dependent i.e. the intensity of the dynamic buffet loads and the frequency content are very much a function

of the geometric shape of the vehicle that produces the separated flow. This also gives rise to one of the major problems in the prediction of buffet loads during the design of launch vehicles. Due to the wide variety in launcher configurations and geometries, (because of varying mission requirements and payload sizes), the available buffeting data are often not readily applicable to any new vehicle in the preliminary design stage. Therefore, whenever a new launch vehicle is developed, extensive testing and simulation is needed by making use of wind tunnel experiments, Computational Fluid Dynamics (CFD) tools and in-flight measurements to assess the new design in terms of buffet characteristics. To this day, the buffeting phenomenon is not fully understood, hence an effective means to counter it cannot be found. As a consequence, the general design philosophy employed by spacecraft engineers is to avoid buffet loads through the use of favorable geometric configurations. In case this is not possible, buffeting has to be accounted for in the structural design such that the vehicle can withstand the dynamic loads that occur throughout its entire flight envelope.

1.2 Problem definition

Buffet loads can occur on various locations on the launch vehicle. The current project however will be confined to the buffeting problem at the base of launch vehicles. As was explained in Section 1.1, unsteady flow separation at the base of launchers during atmospheric ascent gives rise to buffeting loads across the surface of the nozzle. These fluctuating side loads can cause large bending moments to the nozzle fulcrum as illustrated in Figure 1.3. Note that buffeting loads are actually fluctuating pressure distributions along the surface of the nozzle and that the force vector depicted in Figure 1.3 is merely a resultant force at some instant in time. It is not surprising that in order for the nozzle to be able to sustain these loads, restrictions are imposed on its size, shape and minimum weight. A given nozzle carries with it a certain minimum weight for it to withstand the large buffet loads it experiences in flight, because its weight is directly related to its stiffness. Making it larger, to increase propulsion efficiency, will typically increase the bending moments acting on the nozzle fulcrum. Hence to warrant structural integrity weight needs to be added to the nozzle. In turn, this weight penalty could undermine the gain in propulsion efficiency of installing a larger nozzle.

A present-day illustration of the above is the case of Ariane5 (Figure 1.3). This is a heavy-lift launch vehicle developed under the authority of the European Space Agency (ESA) and has been Europe's workhorse for delivering satellites into orbit since the late 1990's. On the original Ariane5 as well as on all subsequent versions, buffet loads at the base of the vehicle were found to be an obstacle in improving propulsion performance. Proposals for a performance enhancing nozzle include large area-ratio nozzles and mechanical extendable nozzles. These nozzles however have a larger nozzle length. This makes them more sensitive to buffet loads because of the larger moment generated around the fulcrum. In addition to structural failure, strong buffeting can cause flow separation inside the nozzle, consequently deteriorating performance (Wong et al. [2005]).

Buffeting is therefore recognized as a critical issue with regard to improving propulsion performance of today's launchers. It prevents the use of more efficient nozzles, because these nozzles cannot meet the structural requirements without becoming too heavy.

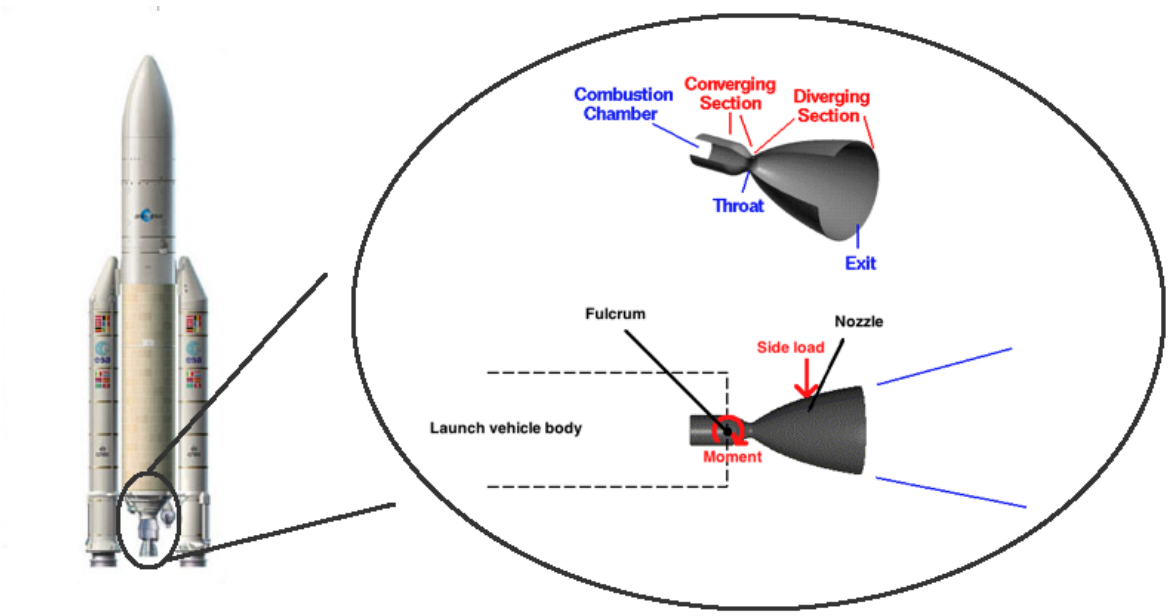

Figure 1.3: (left) ESA's Ariane5 launch vehicle. (right) The generic shape required for a typical launcher nozzle and illustration of forces acting on the nozzle as a result of buffeting. *(adapted from http://www.grc.nasa.gov/ and http://www.esa.int/).*

1.3 Project description

Past research into the flow properties of baseflow buffeting has been performed using both computational as well as experimental approaches. Each approach has its own advantages and disadvantages. Numerical computation methods nowadays can reach adequate accuracies. However it can be computationally expensive to reach such accuracies, depending on the complexity of the flow and the required model. The flow encountered in baseflow buffeting is highly unsteady and turbulent, which requires turbulence models. Three important models are Reynolds averaged Navier-Stokes (RANS), Large eddy simulation (LES) and Direct numerical simulation (DNS). RANS which is the oldest approach to turbulence modeling, solves the flow in terms of time-averaged flow quantities. This method although computationally the cheapest of the three, does not provide instantaneous values of the flow variables. LES on the other hand does provide a time resolved solution by considering the largest and most important turbulence scales in the flow. The smallest scales of the flow are filtered out and their influence is modeled, which greatly reduces the computational cost that would be required to resolve them. DNS avoids modeling as much as possible by resolving the entire range of turbulent length scales. This approach yields a solution closest to the actual flow but is also extremely expensive compared to RANS and LES.

An alternative to CFD is wind tunnel tests, which have the advantage that the actual physical system is being measured i.e. little is lost to mathematical modeling. Therefore in large projects a wind tunnel test is always required as final validation of a design. Furthermore, they are relatively efficient when it comes to testing multiple flow configurations which only requires an adjustment to the positioning of the wind tunnel model. So far experimental methods to evaluate pressure has typically relied on the use of pressure ports/transducers inside wind tunnel models. This however does not provide pressure data in the flow away from the model surface. A pressure probe or even a whole rake of pressure sensors can of course be placed in the flow, however this will interfere with the flow.

Particle Image Velocimetry (PIV) offers a good alternative for pressure sensors being a non-intrusive method that is able to capture a whole flowfield as opposed to only a single point in the flow. However it does not measure the pressure directly, since it only measures particle motion. When using PIV, pressure is to be determined by solving the Navier-Stokes equations where velocity and acceleration are known measured variables. In recent years attempts have been made to determine the pressure field from PIV data and the results are promising van Oudheusden et al. [2007], Van Oudheusden [2008], De Kat et al. [2008], Ragni et al. [2009], De Kat and Van Oudheusden [2010].

The aim of this project is first to characterize the mean velocity field in the wake of a typical rocket base in transonic flow using PIV. Then we will explore the possibilities of utilizing the obtained PIV data to reconstruct the pressure field. Application of this approach has already shown good results in Ragni et al. [2009] where the flow around an airfoil was considered. The flow around the airfoil could for the most part be considered steady and isentropic however. Therefore the effect of turbulent stresses were omitted in the computation. It still remains to be seen whether it is possible to resolve the pressure field in a highly turbulent flow such as encountered in the current project. Hence with the current project an attempt is made to compute the mean pressure field from the RANS equations to assess the applicability of evaluating pressure from PIV data in compressible turbulent flows such as encountered in baseflows.

Thus In order to contribute to the ongoing research the current project explores the potential of studying baseflow with a newly emerging technique which attempts to evaluate pressure from PIV data. In short the aims of the project are two-fold:

- Characterize the mean velocity field of transonic baseflow using PIV.
- Evaluate the mean pressure field using the PIV data as input and assess the efficacy of this approach.

Chapter 2

Flow characteristics

Many studies have been performed in the last couple of decades that contribute to our understanding of the baseflow buffeting phenomenon. To this day the phenomenon is not fully understood and there is still much to learn. Yet serious attempts have already been made in recent years to reduce buffeting. This chapter provides an overview of the most important findings over the decades that have added to our understanding of transonic baseflow. Emphasis is placed on characterizing the flow, although at the end of the chapter some examples are given of recent attempts made to reduce buffeting.

2.1 Flow geometry

Afterbodies of spacecraft launchers come in all kinds of shapes and configurations. In order to effectively study afterbody flows, it is therefore necessary to define a generic shape that can represent the various kinds of existing afterbodies. A well-known and widely studied flow is the so called Backward Facing Step (BFS) flow which is depicted in Figure 2.1. This benchmark flow displays the characteristic features that also occur around launcher afterbodies and can therefore be regarded as a convenient simplification of afterbody flow. In other

Figure 2.1: Geometry for BFS flow.

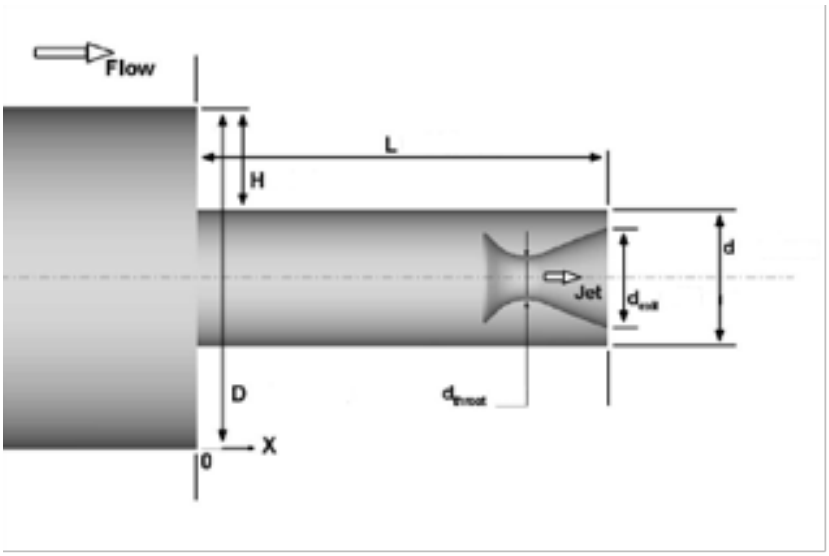

Figure 2.2: Geometry of axisymmetric BFS flow with nozzle (Deck and Thorigny [2007]).

words, our knowledge on BFS flows can be applied to afterbody flows. It must be noted though, that due to the two-dimensional nature of the geometry, some three-dimensional effects that occur in real baseflows are omitted (e.g. streamline convergence). Therefore researchers who are specifically interested in afterbody flows have extended the BFS to three dimensions. This corresponds to revolving the BFS geometry around an axis of symmetry with finite downstream extension of the inner cylinder. The resulting geometry while still being generic, resembles the afterbody shape of a launcher (Figure 2.2). In actual experiments sometimes also the presence of an exhaust jet is simulated, in which case a nozzle needs to be installed. It is the most basic geometry in literature used to model three-dimensional axisymmetric afterbodies. In this report this geometry is referred to as axisymmetric BFS (with finite extension). Apart from varying geometric parameters, there are two distinctive test cases: with or without the presence of a supersonic propulsive jet which exits through the nozzle. Regarding the separated flow there are also two categories to be distinguished: with or without downstream reattachment on the afterbody. These cases have been studied by Deprés et al. [2004]. Another study, performed by Meliga and Reijasse [2007b], Meliga and Reijasse [2007a], accounts for the presence of two boosters. In addition to the BFS, some researchers choose to use a different geometry for studying the flow around afterbodies, e.g. the boat-tailed afterbody (Kumar et al. [2002]).

2.2 Flow topology

In order to get an understanding of turbulent afterbody flows, it is instructive to start by considering the simplest model: the two-dimensional BFS flow. The flow is viewed in terms of mean values and fluctuations with respect to the mean. Figure 2.3 and Figure 2.4 depict the typical mean flow topology for the BFS when the oncoming flow is subsonic and supersonic respectively. The obvious distinguishing feature between the two, is the presence of expansion and compression waves in the latter. But otherwise the two cases are quite similar. Upstream

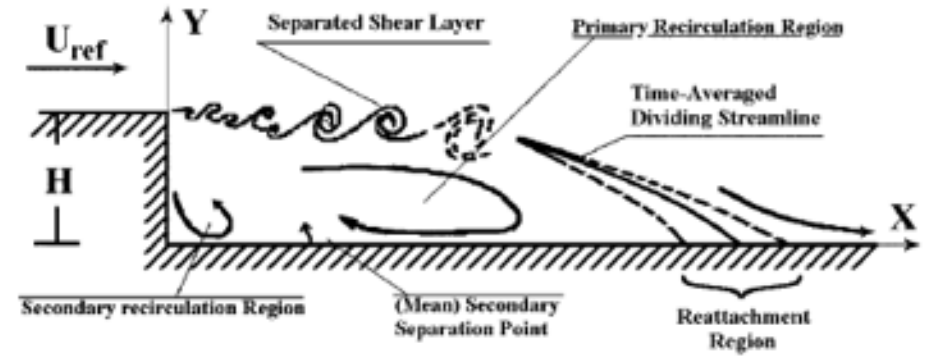

Figure 2.3: Flow topology of subsonic BFS flow (Spazzini et al. [2001]).

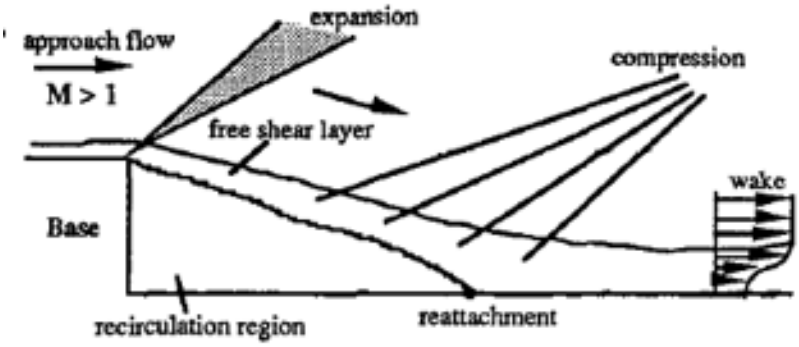

Figure 2.4: Flow topology of supersonic BFS flow (Herrin and Dutton [1995]).

of the base corner ($x < 0$) a turbulent boundary layer has formed. As soon as it reaches the base corner, the abrupt change in the geometry causes the boundary layer to separate. The boundary layer turns into a free shear mixing layer, exhibiting a Kelvin-Helmholtz instability (Deck and Thorigny [2007]) and divides the flow into an outer inviscid flow and an inner recirculation region, also known as the recirculation bubble. This region under the shear layer is completely isolated from the outside flow as the shear layer reattaches again on the afterbody downstream. The unsteadiness of the flow manifests itself in the periodic growth and decay of the recirculation bubble, moving the shear layer outward and inward respectively. This phenomenon hence is commonly referred to in literature as 'shear layer flapping'. Consequently there is no single reattachment point of the shear layer as it fluctuates over time due to the flapping. Hence reattachment is typically defined in terms of its time-averaged location. Among researchers there is not yet full agreement on the exact mechanism and cause of this flapping behavior. However existing theories usually involve the instantaneous imbalance between massflux out of the recirculation bubble due to entrainment by the shear mixing layer and that reinjected into the bubble at reattachment. Within the recirculation bubble there are two characteristic counter-rotating vortices discernable: A large clockwise vortex (primary vortex) and as some studies have indicated, a smaller counter-clockwise vortex (secondary vortex) in the corner (Spazzini et al. [2001], Deck and Thorigny [2007], Bitter et al. [2010]), which has been observed in both subsonic and supersonic cases.

2.3 Role of free-stream Mach number as flow parameter

An important aspect of afterbody/BFS flows is the behavior of the free shear layer originating from the separation point. Hence it seems natural that in BFS flow the same flow parameter is used as in free shear layers. In free shear layers, the convective Mach number M_c has been identified as the compressibility parameter. It is a Mach number defined with respect to a reference frame that is moving with the large-scale structures in the flow (Elliott and Samimy [1990]). In other words it is the Mach number corresponding to the convective velocity of a characteristic large scale structure in the flow. The two streams of a free shear layer have the same convective Mach number if their specific heat ratios are equal. In that case M_c can be calculated with

$$M_c = \frac{U_1 - U_c}{a_1} \tag{2-1}$$

where U_c is the convective velocity of the large-scale structures in the flow and is given by

$$U_c = \frac{a_1 U_2 + a_2 U_1}{a_1 + a_2} \tag{2-2}$$

U_1, U_2 and a_1, a_2 denote the free-stream velocities and speeds of sound of the upper and lower streams respectively. The above can be extended to BFS flows, since the attached boundary layer becomes a free shear layer after separation. Note however, that with regard to BFS flows, there is no real free-stream velocity in the lower stream, which is actually the turbulent recirculation bubble bounded by the afterbody. Nonetheless it should be possible to define an effective free-stream velocity for the recirculation bubble. As noted from equations (2-1) and (2-2), the convective Mach number depends on the free-stream conditions of both the upper and lower stream. But in case of the BFS flow, the only free-stream conditions that can be directly controlled are those in the upper stream to which the lower stream conditions respond accordingly. Hence it is also valid and more convenient to use the free-stream Mach number of the upper stream as the flow parameter for afterbody/BFS flows even though it is not equal to the convective Mach number. It is assumed that the effective lower stream velocity is only weakly dependent on the upper stream velocity or Mach number M_1. Consequently, according to the equations, an increase in M_1 which shall be referred to as M_∞ from here on, corresponds to an increase in M_c. This conclusion makes it possible to easily extend findings from studies regarding 'real' free shear layers where M_c was used as the compressibility parameter, to BFS flows where M_∞ is typically the relevant parameter by determining an empirical relation between M_c in free shear layers and M_∞ in afterbody/BFS flows.

As observed in many studies an increase in the free-stream Mach number of a BFS flow generally elongates the recirculation bubble in streamwise direction, such that reattachment moves further downstream as well. The exception is when the Mach number changes from subsonic to supersonic as is shown in Meliga et al. [2007]. In their experiment they observed that as they increased M_∞ from 0.9 to 1.3, the reattachment length seemed to be shortened. This was caused by the presence of expansion waves at the base corner for the supersonic case, which initially turn the shear layer towards the wall. As the oncoming Mach number is further increased, the reattachment length will move downstream again. Higher Mach numbers also correspond to smaller growth rate of the shear layer and lower levels of turbulence (Herrin and Dutton [1994]; Elliott and Samimy [1990]).

2.4 Properties of the plane mixing layer

The free shear layer originating from the separated boundary layer at the step, curves downwards towards the wall where it reattaches. The first half of the shear layer is still relatively far from the wall and therefore unaffected by its presence. Due to this, the first part of the shear layer exhibits behavior similar to the well-known plane mixing layer. It must be kept in mind though that the flow speed on the lower side is highly turbulent because of the recirculation region, as opposed to the typical plane mixing layer where the upper and lower streams are uniform and parallel but with different velocities. Because of the similarity between the two shear layers, it is instructive to consider some aspects of plane mixing layers that more or less carry over to the separated/reattaching shear layer in BFS flow.

A widely studied aspect of plane mixing layer is the spreading rate, which is defined as the rate of increase of the shear layer thickness with streamwise distance. It appears that the shear layer spreads linearly i.e. the spreading rate is constant. The value of this constant is connected to the convective Mach number as is shown in Figure 2.5 where results from different studies have been compiled. It seems that the spreading rate decreases with convective Mach number. It must be noted that this linear behavior of spreading is observed in fully developed (i.e. self-similar) shear layers. Mehta and Westphal [1986] defined three criteria to evaluate the onset of the fully developed region of a shear layer: (1) The mixing layer thickness grows linearly with the streamwise distance; (2) the shape of the mean velocity profile is independent of downstream distance when scaled by the local mixing layer thickness; and (3) the profiles of all turbulence quantities are independent of streamwise location when scaled by the mixing layer thickness; in particular, peak values of the turbulence stresses should be independent of the streamwise location. The initial shear layer in BFS flow right after separation still needs to develop, meaning that the constant spreading rate is expected to be found some distance downstream of the point of separation. Near reattachment, the shear layer obviously cannot be regarded as a free shear layer as the influence of the wall is not negligible anymore. Cherry et al. [1984] found, in their investigation on separating/reattaching shear layers, that this linear shear layer growth continues relatively unaffected by the reattachment process up to 60% of the reattachment length. Furthermore, Deck and Thorigny [2007] observed an exponential growth of the shear layer thickness right after separation when the shear layer still needs to develop, which is in agreement with linear stability theory applied to plane mixing layers. This exponential behavior was exhibited from the origin of the shear layer up to approximately 20% of the reattachment length.

From these findings it can hence be expected that for BFS flows, a linear spreading rate of the shear layer should be found in the region between 20% and 60% of the reattachment length. The next figures illustrate the flow field properties around a typical plane mixing layer. Figure 2.6 shows the mean velocity profile, Figure 2.7a shows the turbulent intensity profile where y^* is a vorticity thickness similarity parameter. Figure 2.7b and Figure 2.7c show the lateral turbulence intensity and Reynolds shear stress profile of a free shear layer respectively.

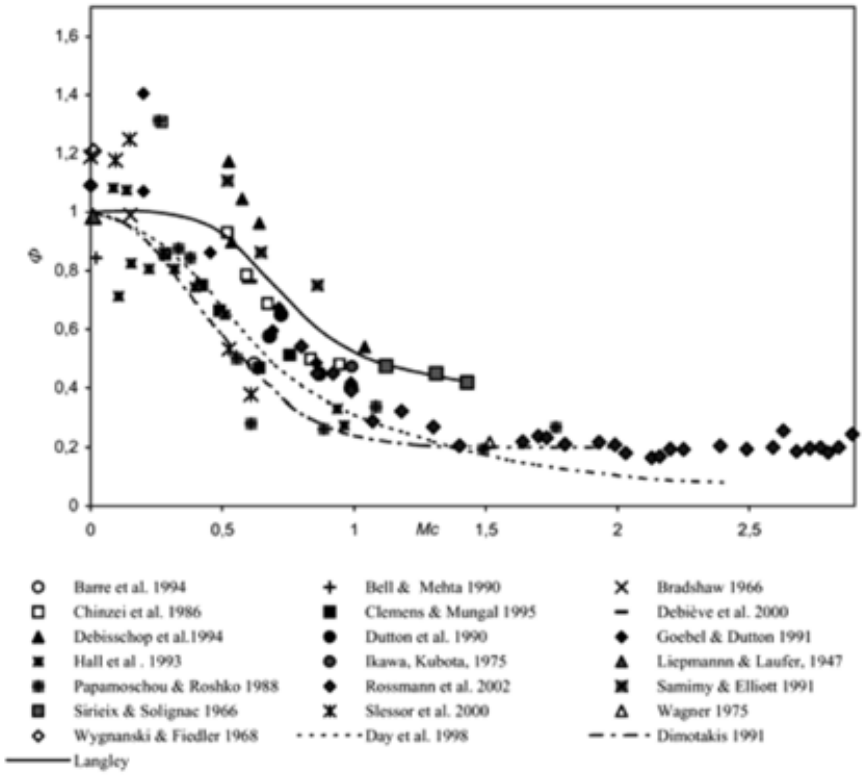

Figure 2.5: Normalized spreading rate of supersonic mixing layers as function of convective Mach number (Smits and Dussauge [2006]).

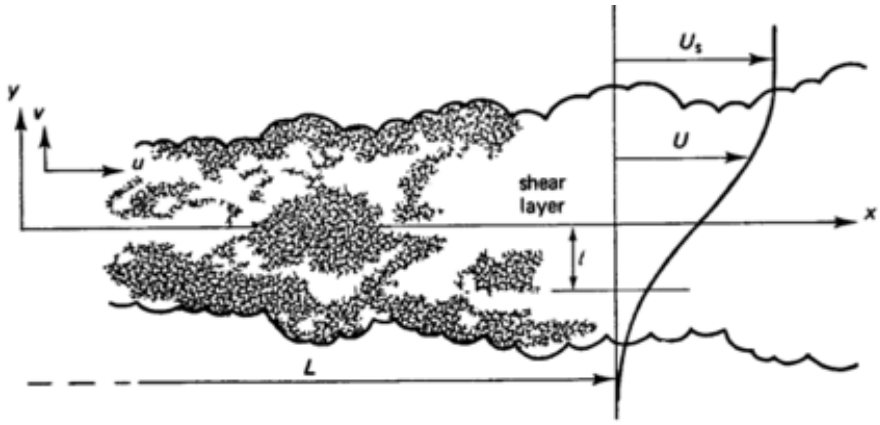

Figure 2.6: Typical velocity profile in a plane-mixing layer (Tennekes and Lumley [1972]).

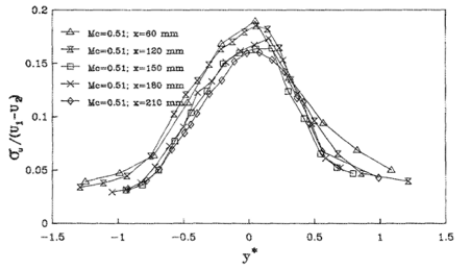

(a) Streamwise turbulence intensity in the developing and fully developed regions.

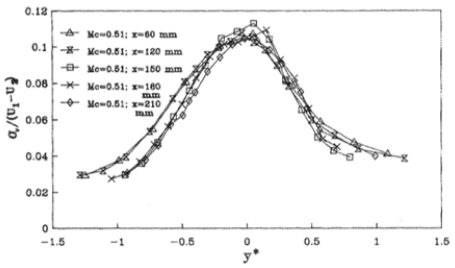

(b) Lateral turbulence intensity in the developing and fully developed regions.

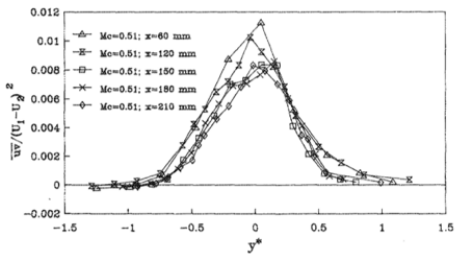

(c) Reynolds shear stress in the developing and fully developed regions.

Figure 2.7: Turbulence properties across a plane mixing-layer (Elliott and Samimy [1990])

2.5 Wall pressure distribution

From a practical engineering perspective, the focus has been obtaining an accurate description of the time-dependent wall pressure distribution, since this allows the computation of the loads acting on the afterbody. Weiss et al. [2009] performed a numerical simulation (see Figure 2.8) of compressible subsonic axisymmetric BFS flow without jet, where the shear layer reattaches near the end of the afterbody. They extracted the wall pressure distribution and compared it with available experimental data. As can be seen in Figure 2.9 the results regarding the mean pressure coefficient are in excellent agreement with those found by Meliga and Reijasse [2007b] and Deprés et al. [2004]. The mean pressure coefficient C_p, is defined as

$$C_p = \frac{\overline{p} - p_\infty}{\frac{1}{2}\rho_\infty V_\infty^2} \tag{2-3}$$

where $\overline{p}$ denotes the time-averaged pressure. It starts decreasing upstream of the separation point, showing the influence of the recirculation region. The flow in the region just upstream of separation is accelerated such that the pressure is adjusted to match the lower base pressure at $x = 0$. The pressure continues to decrease in streamwise direction until approximately halfway along the recirculation bubble after which a strong recompression of the flow occurs and C_p increases again. The maximum value $C_{p,max}$ is reached downstream of the mean reattachment point at $x/L_r \approx 1.15$ where L_r is the reattachment length. The pressure fluctuation coefficient

$$C_{p,rms} = \frac{p'_{rms}}{\frac{1}{2}\rho_\infty V_\infty^2} \tag{2-4}$$

where p'_{rms} is the root-mean-square (RMS) value of the pressure fluctuation, shows a steady increase until it reaches a plateau just upstream of the mean reattachment point. This again is supported by the findings of Meliga and Reijasse [2007b]. Hudy et al. [2003] reasoned that the growth of $C_{p,rms}$ in streamwise direction, which increases rapidly at about $x/L_r \approx 0.5$, is likely to be due to the organized shear layer structures that grow stronger as they move closer to the wall.

Furthermore it is common in literature to perform a spectral analysis of the fluctuations in order to identify the aerodynamic phenomena that might be responsible for the unsteadiness. The wall pressure spectra show different dominating frequencies, depending on the streamwise location in the region of circulation. Like many others, Meliga et al. [2007] found that near the point of separation, the dominant frequency corresponds to a Strouhal number based on the reattachment length $Str_{Lr} \approx 0.1$. This is shown in Figure 2.10a, which depicts the power density spectra for various streamwise locations.

Note that the spectra are plotted in linear/log axes. As a consequence, the value on the y-axis becomes the power spectral density S_{xx} multiplied by the Strouhal number Str_{Lr} because

$$C_{p.rms}^2 = \int_0^\infty S_{xx}(Str)\,\mathrm{d}Str = \int_0^\infty Str \cdot S_{xx}(Str)\,\mathrm{d}\log Str \tag{2-5}$$

This frequency is attributed to the flapping motion of the shear layer which reflects the overall recirculation bubble growth/decay dynamics. Going further downstream, the higher frequencies become more dominant. When $x/D = 0.72$ (D corresponds to base diameter) is reached, which corresponds to the point just upstream of where reattachment begins, a

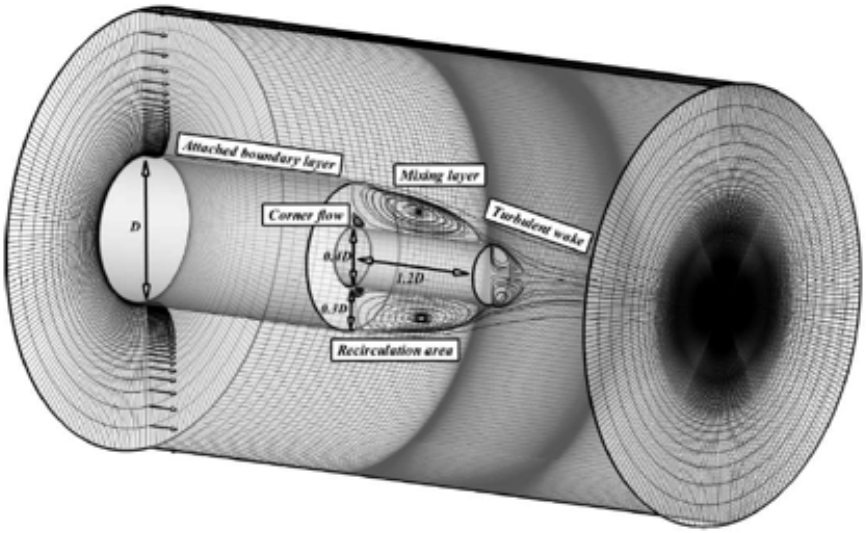

Figure 2.8: Mesh of axisymmetric BFS flow (Weiss et al. [2009]).

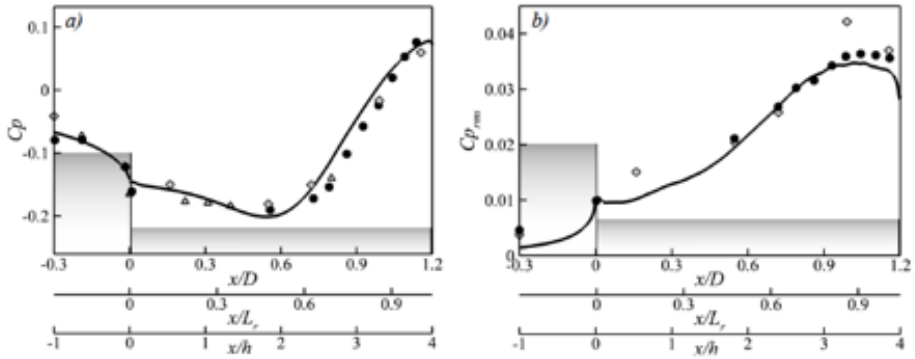

Figure 2.9: Mean streamwise pressure distribution(left) and rms values (right), -: Weiss et al. [2009]; •: Meliga and Reijasse [2007b]; ◇: Deprés et al. [2004] (source: Weiss et al. [2009]).

peak centered around $Str_{Lr} \approx 0.2$ appears. The peak can be linked to the shedding of large-scale turbulent structures. At the end of the body where reattachment occurs, the frequency spectra exhibit a broad peak with a weakly defined maximum around $Str_{Lr} \approx 0.6$, related to characteristic frequency of the vortical structures in the shear layer. Thus the following characteristic frequencies have been observed and linked to the baseflow buffeting phenomenon.

- $\boldsymbol{Str_{Lr} \approx Str_D \approx 0.1}$; Shear layer flapping; most prevalent near separation.
- $\boldsymbol{Str_{Lr} \approx Str_D \approx 0.2}$; Shedding of large-scale turbulent structures; most prevalent halfway along circulation bubble.
- $\boldsymbol{Str_{Lr} \approx Str_D \approx 0.6}$; Vortical structures within shear layer; most prevalent in reattachment region.

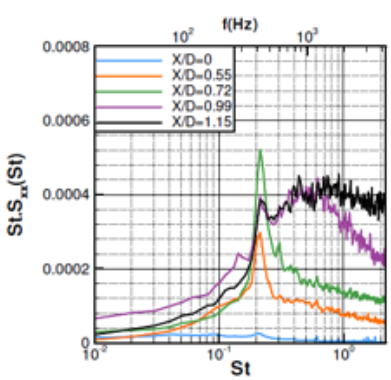

(a) Power density spectra of wall pressure at various streamwise locations for $M_\infty = 0.7$.

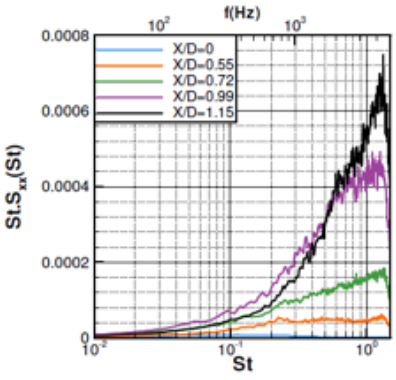

(b) Power density spectra of wall pressure at various streamwise locations for for $M_\infty = 1.3$.

Figure 2.10: Power density spectra of the wall pressure (Meliga et al. [2007]).

In addition to the streamwise evolution of the pressure distribution, also the azimuthal coherence is useful to obtain insight into the buffeting phenomenon. This method to analyze coherent structures in the flow around axisymmetric bodies, was first proposed by Fuchs et al. [1979] and later adopted by many others. The complex coherence function may be defined as

$$C = C_r + iC_i = \frac{S_{12}(r, X, \phi_1, \Delta\phi, f)}{\sqrt{S_{11}(r, X, \phi_1, f)S_{22}(r, X, \phi_2, f)}} \tag{2-6}$$

where S_{12} is the cross-spectral density being a function of the radial position r, streamwise location X, reference azimuthal angle ϕ_1, azimuthal angle between correlation points $\Delta\phi = \phi_2 - \phi_1$ and the signal frequency f. Note that $|C| = \gamma$ is the classical coherence function. The axisymmetric BFS flow allows for a number of assumptions to be made that simplify the complex coherence function. The first assumption is that of homogeneity in azimuthal direction, which means that the azimuthal coherence or cross-spectral density is independent of the reference angle ϕ_1:

$$S_{12} = S_{12}(r, X, \Delta\phi, f) \tag{2-7}$$

Another assumption is that the flow has no mean swirl. Hence the disturbances exhibit no particular helical propagation in streamwise direction. This results in a symmetry condition:

$$S_{12}(-\Delta\phi) = S_{12}(\Delta\phi) \tag{2-8}$$

and implies that

$$C_i = 0 \tag{2-9}$$

such that in this case the coherence function consists only of a real part. Finally, the axisymmetric flow should have 2π periodicity with respect to $\Delta\phi$. This allows the real coherence function C_r to be constructed from azimuthal modes using Fourier decomposition:

$$C_r = C_r(\Delta\phi, f) = \sum_{m=0}^{\infty} C_{r,m}(f)\cos(m\Delta\phi) \tag{2-10}$$

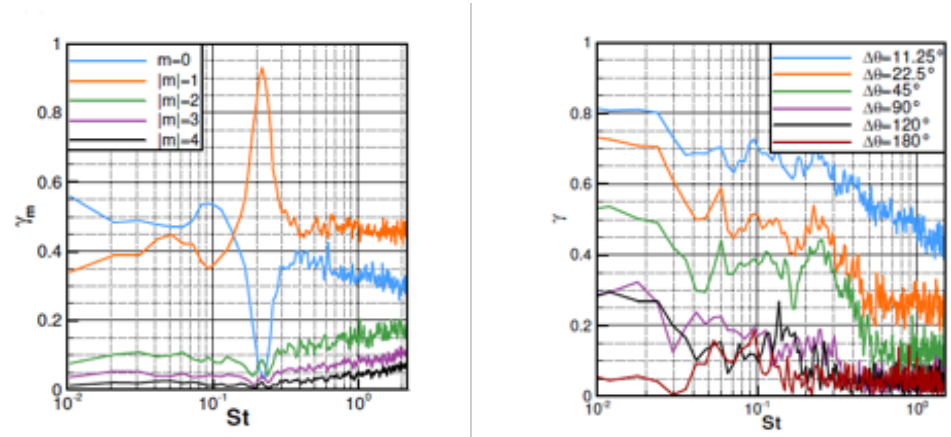

(a) Coherence spectra of first five azimuthal modes at X/D=0.72 for $M_\infty = 0.7$.

(b) Coherence function for various azimuthal angles for $M_\infty = 1.3$.

Figure 2.11: Coherence in the recirculation area (Meliga et al. [2007]).

The $C_{r,m}$ coefficients represent the percentage of the spatially fluctuating energy relative to a particular mode m at a certain signal frequency. Figure 2.11a shows the coherence spectra of the first five azimuthal modes at location X/D=0.72, which is near the middle of the recirculation region.

Note that $\gamma_m = |C_m|$ but that due to the assumption that the imaginary part is zero: $C_{i,m} = 0$, we have in this case $\gamma_m = C_{r,m}$. The spectra display a highly coherent mode at the large-scale vortex shedding frequency $Str_{Lr} = 0.2$ for the first azimuthal mode $|m| = 1$. The coherent mode originates from the region in the middle of the recirculation bubble where absolute instabilities are generated (more on this in section 2.7). The strong dominance of the first azimuthal mode is associated with an antiphase relationship of the signals between two points opposite of each other on the afterbody ($\Delta\phi = 180$ deg). It is this antiphase relationship of the pressure fluctuations at $\Delta\phi = 180$ deg that results in an unequal loading on the afterbody, which produces the unsteady net force that is responsible for baseflow buffeting. Meliga et al. [2007] also investigated what happens when the free stream Mach number is increased. They observed that when it is high enough, in their case it was at $M_\infty = 1.3$, the instability characteristics of the wake are changed by which the growth of the antisymmetric fluctuations are suppressed. Consequently, the flow exhibits no particular frequency peak associated to the shedding of large-scale vortices and no particular azimuthal structure is to be found. From the latter it can be concluded that the global coherent mode does not develop anymore in this case. This is indicated in Figure 2.10b and Figure 2.11b (note that $\Delta\theta$ denotes the same as $\Delta\phi$). Deck and Thorigny [2007] performed a numerical investigation of axisymmetric BFS flow with jet and reattachment of the shear layer at the end of the afterbody. Their results are shown in Figure 2.12a, 2.12b and 2.12c.

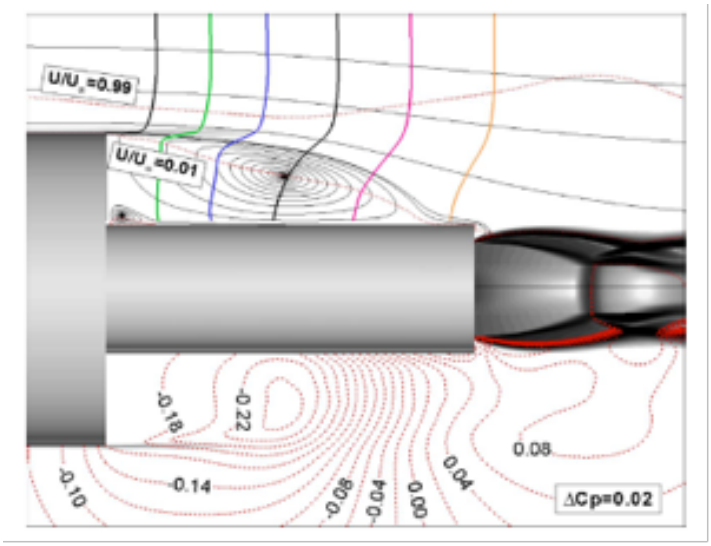

(a) Time-averaged flowfield. Upper part: velocity profiles (colored) and isovelocity (dotted) lines. Lower part: iso-Cp lines.

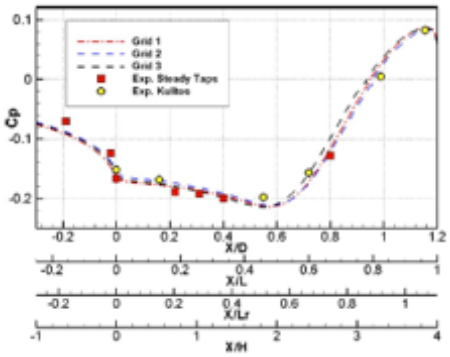

(b) Streamwise distribution of wall pressure coefficient.

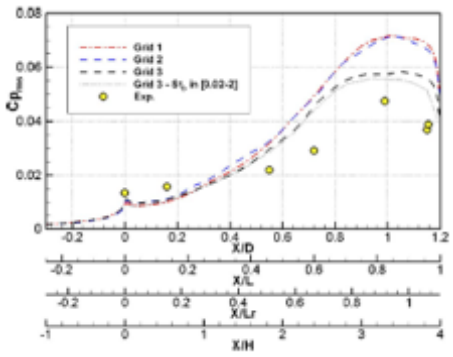

(c) Streamwise distribution of the coefficient of rms wall pressure fluctuations.

Figure 2.12: Computational and experimental results from Deck and Thorigny [2007].

Figure 2.12a gives a nice overview of the whole time-averaged flowfield around the afterbody with jet. From Figure 2.12b and 2.12c it can be seen that the wall pressure distribution is similar to the case without jet, implying that the presence of a jet has no significant influence. This is in agreement with Deprés et al. [2004], who performed tests with ideally expanded jets as well as overexpanded jets. He found that the jet only had a strong effect in case the shear layer reattached downstream of the afterbody on the jet itself. Their results are shown in Figure 2.13a and 2.13b. The configuration concerns an afterbody that extends up to $x/D = 0.6$ such that no reattachment of the shear layer occurs on the body itself (the same study showed that the reattachment point was around $X/D = 1.2$).

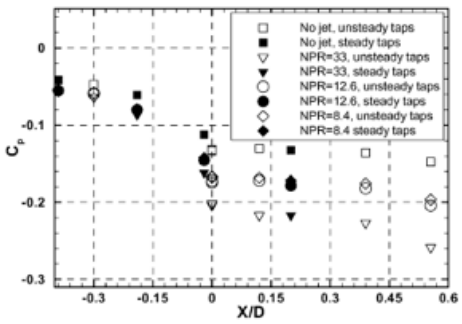

(a) Streamwise distribution of wall pressure coefficient for the case without solid reattachment of the shear layer (L/D=0.6).

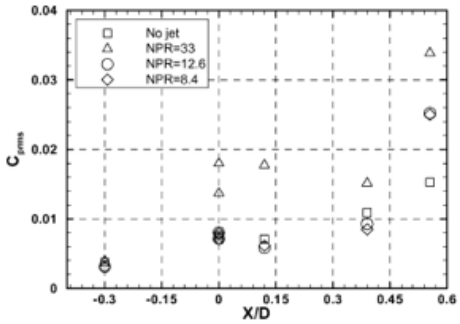

(b) Streamwise distribution of RMS wall pressure fluctuations for the case without solid reattachment (L/D=0.6).

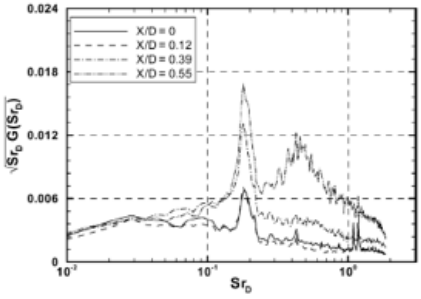

(c) Wall pressure spectra on L/D=0.6 afterbody (no solid reattachment) without jet.

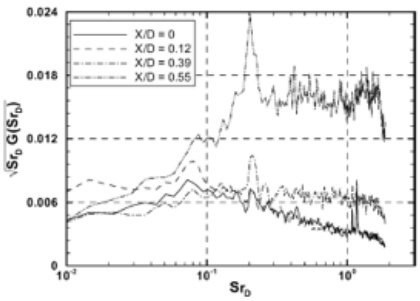

(d) Wall pressure spectra on L/D=0.6 afterbody (no solid reattachment) with jet.

Figure 2.13: Wall pressure data from experimental study by Deprés et al. [2004].

The mean pressure coefficient as can be seen in Figure 2.13a, decreases steadily in streamwise direction if no reattachment occurs. When there is a jet,the C_p curve is approximately shifted down compared to the no-jet case. This is due to the strong suction effect of the jet which decreases the pressure in the whole recirculation region and even in the attached boundary layer up to $x/D = -0.4$. The effect is strongest for the ideally expanded jet and decreases for overexpanded jets. The RMS values also seem to be affected the most by the jet at adaptation, showing a strong increase in the base region and at the end of the afterbody at $x/D = 0.6$. For overexpanded jets, the RMS values are almost the same as without jet except at the end where a strong increase occurs.The pressure spectra of the flows without solid reattachment

for the cases with and without jet, are shown in Figure 2.13c and Figure 2.13d respectively. In the no-jet scenario, the spectra are dominated by a peak at a Strouhal number based on the base diameter of $Str_D = 0.18$. Note that the diameter is approximately the reattachment length such that $Str_{Lr} \approx Str_D$. This means that the flow is characterized by the shedding of large-scale vortices that were also found in the test case where solid reattachment did occur. The configuration with jet exhibits a maximum at approximately the same frequency. However the amplitude of the peak, relative to the other frequencies, is weaker compared to the no-jet spectra. Deprés et al. [2004] reasoned that the reduced dominance of the large-scale vortex shedding frequency is because the presence of the jet interferes with the development of large-scale vortices. Near the end of the afterbody the higher frequencies show a significantly increased contribution, which appears to explain the evident increase in RMS values near the end of the body as indicated before in Figure 2.13b.

2.6 Propagation of disturbances

In an experimental study, Hudy et al. [2003] investigated the pressure distribution below a separating/reattaching flow. Although the configuration they used (fence in front of a splitter plate) was not exactly BFS, the resulting flow is quite similar exhibiting the same characteristic flow features. By means of cross-correlating the pressure fluctuations across the whole region under the separating/reattaching flow, taking the pressure at the reattachment location as reference, they were able to determine the space-time character of propagating pressure disturbances in the flow. Figure 2.14a and Figure 2.14b depict contour maps of the cross-correlation coefficient, using as reference the fluctuations at reattachment and at $x/x_r = 0.25$ respectively. The peak correlation of the signal at some location x with respect to the reference signal is found by delaying the signal recorded at that location which corresponds to a negative τ. The locus of peak correlation points in Figure 2.14a, indicated by the dashed line, has a negative slope. This indicates that the fluctuations measured at the reattachment point are traveling downstream, since going in downstream direction, τ becomes more negative, which means that the signal must be delayed more to be correlated with the reference signal at reattachment. Note that at the origin, of the plot corresponding to the reattachment point, the delay is zero since naturally the peak correlation is the auto-correlation of the reference signal. Figure 2.14b displays again a contour map, but with reference point at $x/x_r = 0.25$. In addition to a negatively inclined lobe, the plot shows a positively inclined lobe as well, indicating the presence of upstream traveling disturbances. These are important results supporting the hypothesis that disturbances felt at the reattachment point originate from upstream locations and only travel further downstream, while in the middle of the recirculation zone, pressure disturbances can travel both upstream as downstream. This is also supported by findings of Deck and Thorigny [2007] who performed a numerical investigation on axisymmetric BFS flow. They observed that upstream and downstream propagating pressure fluctuations seem to originate near the middle of the recirculation region. This is shown in Figure 2.15. These results are used in the discussion in the next section on analytical models.

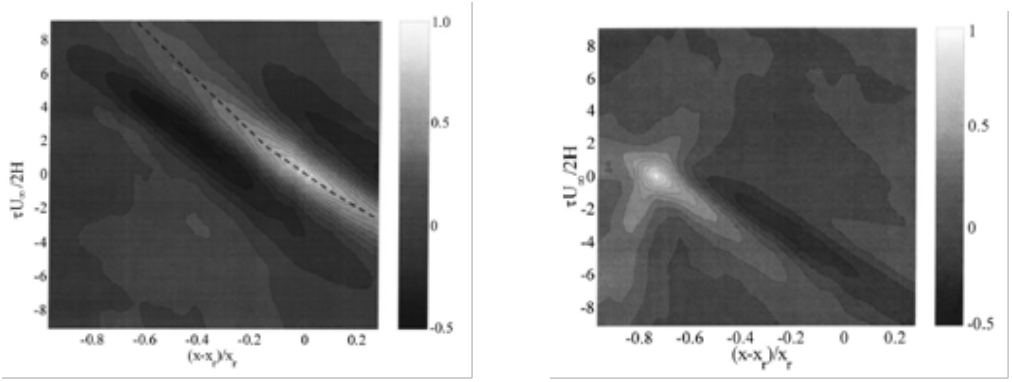

(a) Contour map of cross-correlation coefficient with reattachment point as reference .

(b) Contour map of cross-correlation coefficient with $x/x_r = 0.25$ as reference point.

Figure 2.14: Results from cross-correlating pressure fluctuations across the recirculation area (Hudy et al. [2003]).

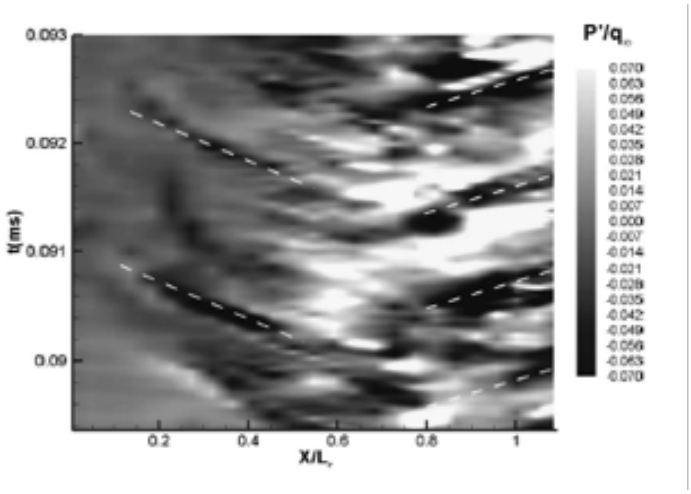

Figure 2.15: Space-time contours of pressure fluctuations on an axisymmetric BFS afterbody (Deck and Thorigny [2007]).

2.7 Linear stability analysis

An analysis has been performed by Wee et al. [2004] and Weiss et al. [2009] using the concept of local absolute/convective instabilities, in order to determine the nature of global instability in the two-dimensional BFS flow. For a more elaborate discussion on this method and mathematical derivations see the paper of Huerre and Monkewitz [1990]. An absolute instability occurs when an initial disturbance grows at a fixed location, gradually spreading through the whole flow field. In case of a convective instability, the initial disturbance grows while moving away from its source. Hence, unless the flow in the convective instability region is constantly perturbed, these convective disturbances will eventually leave the flow field in its undisturbed state. To determine which type of instability the flow exhibits, the absolute mode is examined. This is a particular mode that tells us about the growth of a disturbance occurring at some initial location. More specifically, the absolute mode frequency which consists of a real and imaginary part $\omega_0 = \omega_{0,r} + i\omega_{0,i}$ contains information on the behavior of a disturbance in terms of stability and oscillation. If the absolute mode is unstable i.e. $\omega_{0,i} > 0$, the flow exhibits absolute instability. On the other hand if the absolute mode is stable i.e. $\omega_{0,i} < 0$ then the flow exhibits convective instability. In other words $\omega_{0,i}$ represents the growth rate of the absolute mode. The real part of the absolute mode $\omega_{0,r}$ represents the frequency of the mode.

In the analysis of Wee et al. [2004] there were two parameters that determined the resulting absolute mode of the flow. These were the ratio of backflow to forward flow β, and the thickness of the shear layer δ. They calculated the complex frequency of the absolute mode for various values of β and δ (see Figure 2.16) and observed that for a constant δ, the flow changes from being absolutely stable (i.e. convectively unstable) to absolutely unstable for increasing β. Keeping β fixed, the flow becomes less and less absolutely stable for decreasing δ and can even become absolutely unstable if there is sufficient backflow. Furthermore it is noted that the mode frequency $\omega_{0,r}$ is only weakly dependent on β. This means that changes in the backflow to forward flow ratio that occur in the recirculation region do not affect the frequency of the absolute mode significantly. However, changes in β do have a large impact on the nature of the instability (absolute vs. convective). As can be seen from Figure 2.16, regions with strong backflow (high β) are responsible for absolute instabilities in the flow. With these results, the stability characteristics at different stations of the BFS flow can be determined by inspecting their respective velocity profiles depicted in Figure 2.17. In region (a) in Figure 2.17 close to the separation point, the shear layer is still very thin and the backflow is weak. This situation corresponds to the region in the lower right corner in the graph of Figure 2.16 and hence the flow in region (a) is absolutely stable. Perturbations introduced here are convected downstream. In the middle of the recirculation bubble, denoted as region (b), the shear layer thickness has grown to be $\delta \sim 0.4$ (scaled with h) hence it is in the same order as the step height h. Furthermore the amount of backflow has increased dramatically in this region. These conditions make the flow locally absolutely unstable. Hence perturbations introduced here, or convecting perturbations arriving from upstream locations, grow locally both in upstream as in downstream direction. Region (c) corresponds to the region of shear layer reattachment. Apart from the backflow being reduced compared to the middle of the recirculation bubble, also the shear layer has grown so much that it has become impossible for the flow to maintain an absolutely unstable mode. Hence Wee et al. [2004] concluded that absolutely unstable modes are more likely to originate from the middle of the

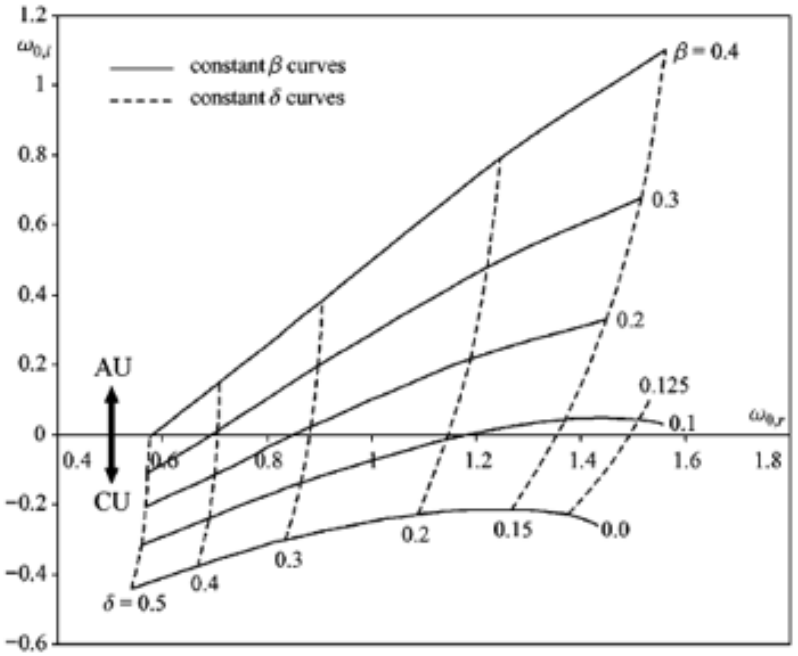

Figure 2.16: Absolute mode frequencies of BFS flow for different values of shear layer thickness δ and strength of backflow β (Wee et al. [2004]).

recirculation zone. They also observed that in the middle of the recirculation region, since $\delta \sim 0.4$ and hence $\omega_{0,r} \sim 0.7$, the frequencies of the absolute modes originating from this region scale as $Str_h = \omega_{0,r}/(2\pi) \sim 0.1$, Str_h being the Strouhal number based on the step height. It implies that this region's rather universal frequency of $Str_h = O(0.1)$ will also be found downstream at the end of the recirculation bubble. Wee et al. [2004] recognized that the absolutely unstable region of the recirculation bubble caused the flow to act like an unstable oscillator. Region (b) essentially acts as the wavemaker for the entire flow and consequently the frequency of the largest eddy formation and shedding should be $Str_h = O(0.1)$.

Also in Weiss et al. [2009] a stability analysis was carried out, which was part of an extensive numerical simulation of an axis symmetric BFS at Mach 0.7. Their results are summarized in

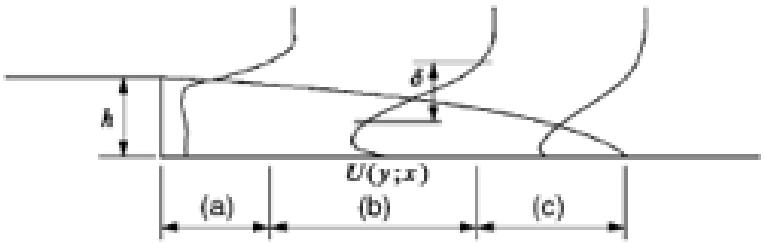

Figure 2.17: Typical velocity profiles in three regions of BFS flow. (a): $\delta << h$ with weak backflow. (b): $\delta = O(h)$ with strong backflow. (c): $\delta = O(h)$ with moderate backflow (adapted from Wee et al. [2004]).

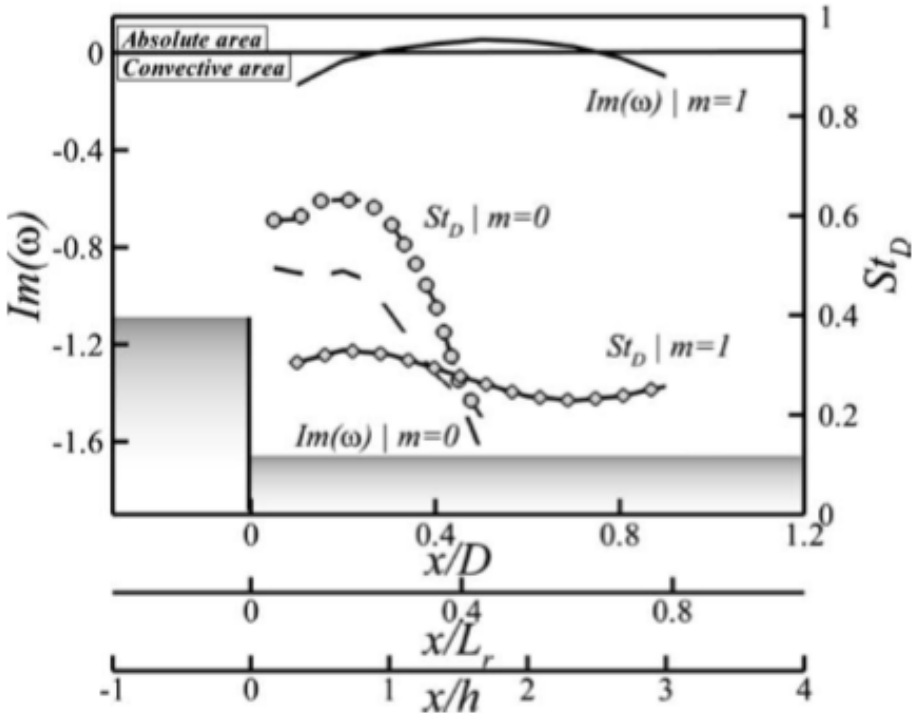

Figure 2.18: Streamwise evolution of Strouhal number Str_D and absolute growth rate $Im(\omega)$ for the m=0 and m=1 modes

2.18. Shown are the streamwise evolution of the Strouhal number based on the base diameter Str_D for the first two azimuthal modes (m=0 and m=1). Also plotted are the absolute growth rate $Im(\omega)$ for the respective modes (dashed line corresponding to m=0 and solid line represents m=1). Figure 2.18 supports the hypothesis that absolute unstability exists in the central region of the recirculation bubble ($0.35 \leq x/D \leq 0.75$) and is exhibited by the antisymmetric mode m=1 at the characteristic frequency $Str_D \approx 0.2$.

2.8 Solutions to buffeting

For the last decades studies have been performed to be able to understand and predict BFS/afterbody flows. With engineering in mind, the next step is to investigate ways to control the flow, such that more efficient, better performing launchers can be designed. Several attempts at reducing the buffeting phenomenon have already been made in recent years. For example Heenan and Morrison [1998] looked at the effect of a permeable reattachment surface for a BFS flow. They observed that the permeable configuration, removed the flapping frequency and attenuated overall pressure disturbances. This was caused by a fairly steady mass flux in upstream direction into the recirculation bubble which seemed to balance the fluid entrainment in the bubble. Consequently the periodic growth/decay of the bubble and hence the flapping was greatly reduced. However a permeable wall, although it seems effective in two-dimensional BFS flows, is not very practical on launcher afterbodies. Meliga et al. [2007] investigated the effect of an axisymmetric serrated skirt (see Figure 2.19) on the buffeting

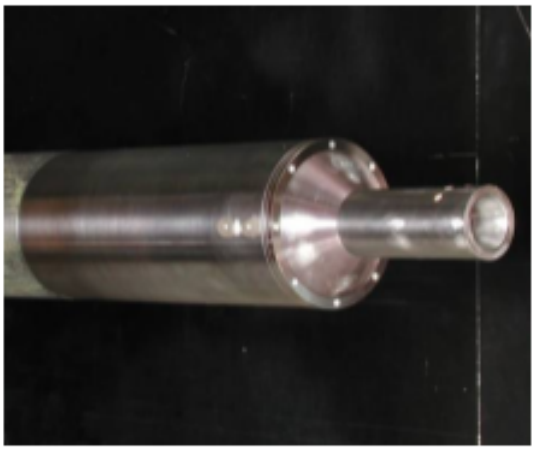

(a) Wind tunnel model in nominal configuration

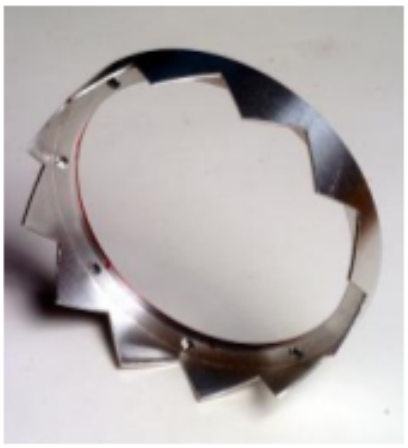

(b) Serrated skirt to be mounted on the model base

Figure 2.19: Wind tunnel model for simulating afterbody flow (axisymmetric BFS) and serrated skirt for passive flow control used in Meliga et al. [2007].

phenomenon for an axisymmetric afterbody. It was expected that the skirt would change the spatial organization of the separated flow by generating small-scale turbulence. However the teeth of the skirt did not seem to have any significant effect. The serrated skirt in fact, acted no different from a smooth skirt, which displaces the separation point downstream and hence also the reattachment point. They suggest that a serrated skirt with an odd number of teeth might lead to different results by breaking the symmetry. Schrijer et al. [2010] tested the influence of various axisymmetric serrated skirts to see if geometric differences of the saw-tooth like pattern had a significant impact on the resulting velocity flow field. No significant differences were found between the different skirts. So far, most attention has been focused on skirt configurations to deal with buffeting and it seems that skirt configurations only have a minor reducing effect on buffeting which does not necessarily compensate for the increase in weight on the launcher if skirts were indeed to be installed.

A different approach has been tested by Weiss and Deck [2011] in a numerical simulation. An attempt was made to control the antisymmetric azimuthal mode, which has been identified as the main contributor to the buffet loads, by modelling controlled jets acting in the separated flow region. The use of controlled jets was expected to decrease the large scale coherence in the recirculation region. Two test cases with the jets were considered and the results compared to the nominal configuration without jets. The test cases differed only in the placement of the jets. The first case employs four jets equally spaced in azimuthal direction and they are placed at the junction between the base and the afterbody extension. The second case is similar in the sense that it also consists of four equally spaced jets, however they are located at the edge of the base near the point of separation. The two different jet configurations are illustrated in Figure 2.20. The jets operated continuously injecting air with a blowing coefficient C_μ on the order of 0.015%. It is defined as

$$C_\mu = \frac{\dot{m}_j V_j}{\frac{1}{2}\rho_\infty V_\infty^2 S} \tag{2-11}$$

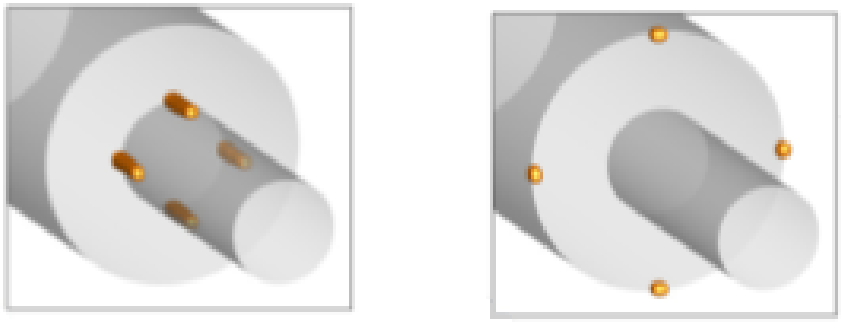

(a) Controlled jets test case 1 **(b)** Controlled jets test case 2

Figure 2.20: Positioning of the controlled jets (orange markers) in the CFD study by Weiss and Deck [2011].

where the subscript j refers to the jet. The mean streamwise velocity fields for the nominal and test cases with jets are presented in Figure 2.21. Streamlines reveal the organization of the recirculation bubble in the time-averaged sense. Upon comparison with the nominal case it is clear that test case 2 with jets positioned at the edge of the base, only has a limited effect on the spatial organization of the mean flow. On the contrary the jets in test case 1 display a much stronger presence since the flow has significantly been altered. The primary vortex has been moved further downstream. Furthermore the secondary vortex that arised naturally in the corner is gone because of the jet that is located there. Instead a new type of secondary vortex appears much further downstream and could be the result from the roll-up of the jet encountering the primary vortex.

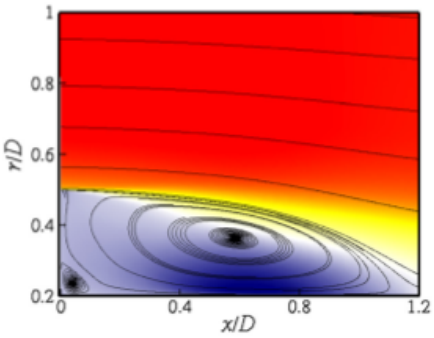

(a) Nominal configuration

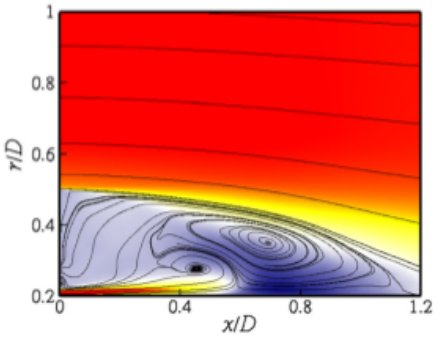

(b) Controlled jets test case 1

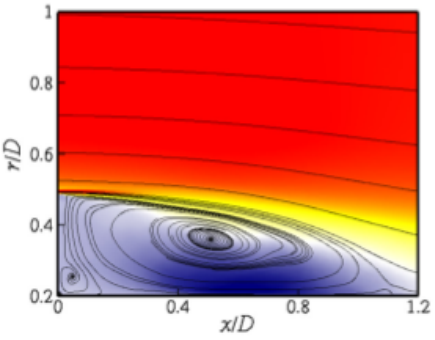

(c) Controlled jets test case 2

Figure 2.21: Streamwise velocity contours and streamlines in the mean flowfield of the nominal and controlled jet configurations Weiss and Deck [2011].

The spatial distribution of the fluctuating energy for the frequency $Str_D = 0.2$, which has been identified as the most important contributor to the antisymmetric mode, is shown in Figure 2.22. This allows to see the influence of the jets. Most striking is the result is found in Figure 2.22b. The broad band of energy occurring in the nominal test case has dissappeared. What is left is four regions of weaker fluctuations centered around $\theta = 0°, 90°$, 180° and 270° which correspond to the azimuthal locations of the jets. Test case 2, however shows no large differences with the nominal configuration.

The coherence function of the antisymmetric mode is displayed for all three configurations in Figure 2.23. The highest percentages of fluctuating energy are found for $Str_D = 0.2$ in the region $0.35 \leq x/D \leq 0.75$. Note that this is to be expected since in previous studies it was established that the antisymmetric mode is associated with this particular frequency and was most prominent in the central region of the recirculation bubble. From Figure 2.23b it can be seen that the energy level of the antisymmetric mode around $Str_D = 0.2$ has been significantly reduced in the middle region (between the dashed lines). The results from test case 2 in Figure 2.23c show a similar distribution as the nominal configuration, except that in the region close to the base ($0 \leq x/D \leq 0.35$), the fluctuations associated to the flapping frequency $Str_D = 0.1$ become more coherent.

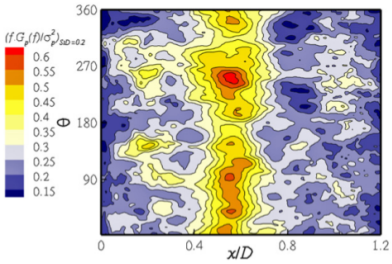

(a) Nominal configuration

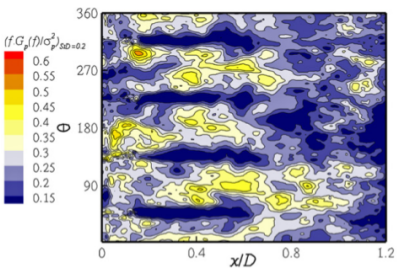

(b) Controlled jets test case 1

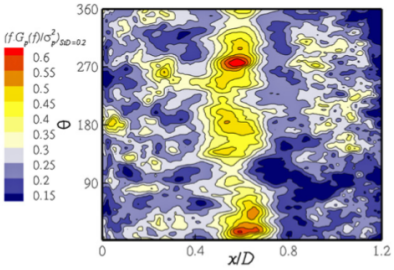

(c) Controlled jets test case 2

Figure 2.22: Contour maps (x/D vs azimuthal angle θ) of dimensionless Power Spectral Density for the dimensionless frequency $Str_D = 0.2$ Weiss and Deck [2011].

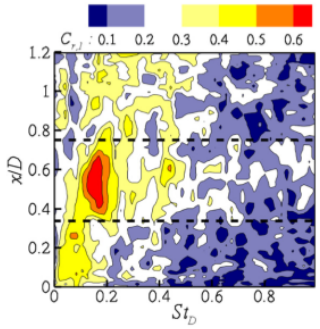

(a) Nominal configuration

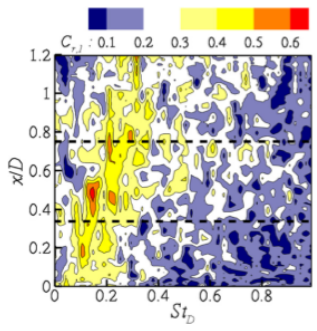

(b) Controlled jets test case 1

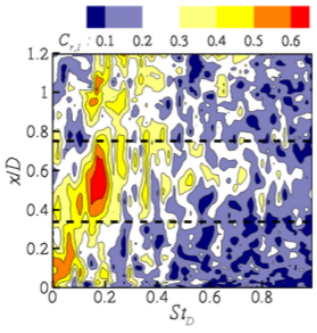

(c) Controlled jets test case 2

Figure 2.23: Contour maps of the antisymmetric azimuthal pressure mode $C_{r,1}$ for every streamwise location along the afterbody extension versus nondimensional frequency (Weiss and Deck [2011]).

Finally the power spectral density of the integrated buffet loads for all three configurations is plotted in Figure 2.24. The graph still shows that the strongest contribution is at $Str_D = 0.2$ for the configurations with jets, but the amplitude is reduced. In terms of RMS values, the amplitude has been reduced by 12% and 3% by test case 1 and 2 respectively. The substantial reduction of 12% seems very promising and Weiss and Deck [2011] suggested future research where for example instead of continuously blowing jets, pulsed jets are used to target particular azimuthal modes.

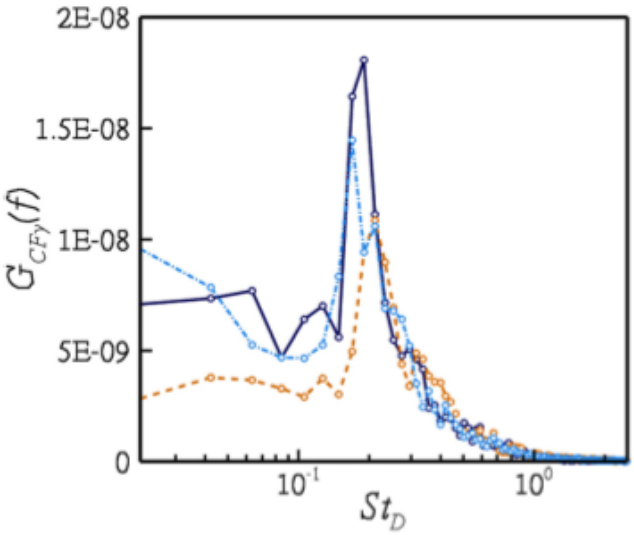

Figure 2.24: Power spectral density of the y-component (i.e. in normal direction) of the buffet load. (Solid line): Nominal configuration; (Orange): Jets test case 1; (Blue): Jets test case 2 (Weiss and Deck [2011]).

Chapter 3

Flow imaging techniques

An important part of the current project consists of performing wind tunnel experiments. This chapter explains the working principles of the different experimental flow imaging techniques that are used. These are *Background Oriented Schlieren* and *Particle Image Velocimetry*.

3.1 Background Oriented Schlieren

Background Oriented Schlieren (BOS) is an experimental technique that can be used to determine the density field. The basic configuration consists of a camera observing some image that is placed in the background of the flow (see Figure 3.1). When a flow with density gradients is running, the Schlieren effect occurs due to the changes in refractive index within the medium. This causes local distortions in the background image captured by the camera. The measured image displacements with respect to the no-flow situation (i.e. the reference case which has no density gradients) correspond to local density gradients from which ultimately a density field can be reconstructed. The relation between refractive index and density is given by the Gladstone-Dale equation shown in equation (3-1) where n is the index of refraction and C is the Gladstone-Dale constant.

$$\frac{(n-1)}{\rho} = C \tag{3-1}$$

From equation (3-1) it is clear that $\nabla n \sim \nabla \rho$. Furthermore, consider the displacement Δy shown in Figure 3.1 which is in the y-direction. Assuming small deflections, the image displacement is related to the deflection angle ε_y by

$$\Delta y = Z_D M \varepsilon_y \tag{3-2}$$

where M is the magnification factor. The above equation can also be rewritten in the form (Richard and Raffel [2001])

$$\Delta y = f\left(\frac{Z_D}{Z_D + Z_A - f}\right)\varepsilon_y \tag{3-3}$$

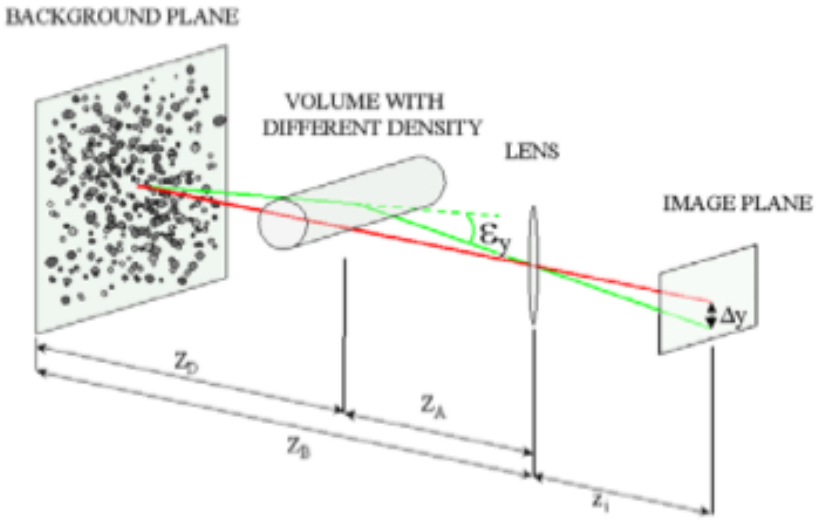

Figure 3.1: BOS setup (Richard and Raffel [2001]).

which shows how the sensitivity of the captured image distortions depends on the parameters of the camera setup. The deflection angle ε in turn is related to ∇n. In y-direction the relation can be expressed as follows (Venkatakrishnan and Meier [2004]).

$$\varepsilon_y = \frac{1}{n_0} \int_{Z_D - \Delta Z_D}^{Z_D + \Delta Z_D} \frac{\delta n}{\delta y} \, \mathrm{d}z \tag{3-4}$$

Hence it can be stated that $\varepsilon \sim \nabla n \sim \nabla \rho$ and it is this relationship on which the principle of the BOS method is based. The image displacements are evaluated through cross-correlation analysis of two images (more on this in section 3.2.4), i.e. the reference image and the image of the flow with density gradients.

3.2 Particle image velocimetry

A nowadays very popular experimental technique is Particle Image Velocimetry (PIV). An overview of its basic features can be found in Figure 3.2. It illustrates the basic setup as well as the measurement process for so called planar or 2-component (2-C) PIV. This method is used to determine the in-plane velocity components of the flow within a certain plane. Upstream of the measurement region, small tracer particles have been inserted into the flow. As they travel into the measurement region a certain plane of particles is illuminated by a laser light sheet. The laser illuminates the plane (at least) twice within a short time interval during which images are recorded by a camera. In two subsequent images, groups of particles can be identified with post-processing software. Their relative displacement from one image with respect to the other, divided by the time interval then gives an estimate of the actual flow velocity. In the following sections the main elements of PIV i.e. tracer particles, light source, image recording and evaluation of particle motion are briefly discussed.

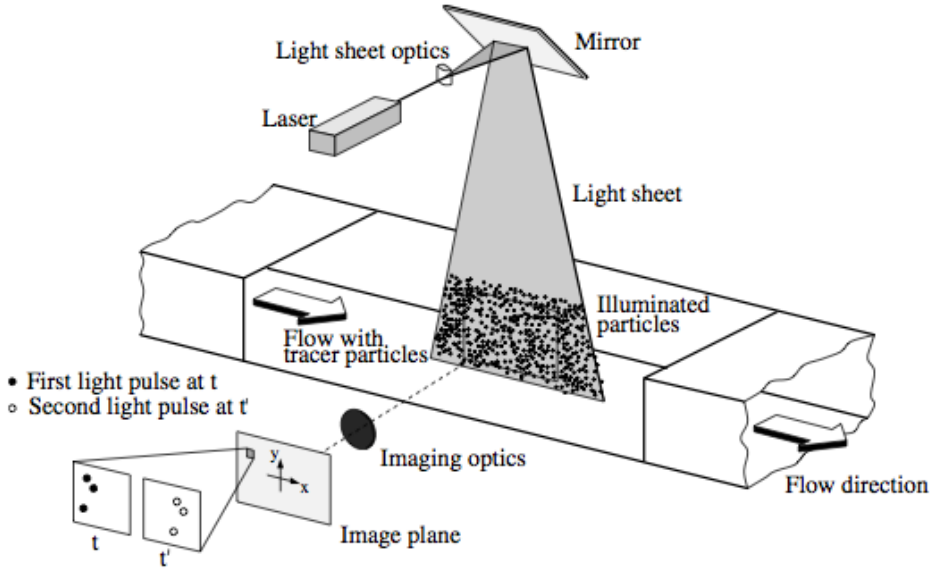

Figure 3.2: Typical arrangement for PIV measurements in a windtunnel (Raffel et al. [2007]).

3.2.1 Tracer particles

PIV measures the flow velocity indirectly since it is the motion of the tracer particles that is being recorded. The estimation of flow velocity with PIV is justified by the assumption that the particle motion closely resembles the fluid motion. Hence it is necessary to be aware of the fluid mechanical properties of the particles used in experiments to make sure that the assumption is indeed valid. An estimate of the difference between particle velocity $\mathbf{U}_p$ and flow velocity $\mathbf{U}$ in a continuously accelerating fluid can be made with equation (3-5).

$$\mathbf{U}_{lag} = \mathbf{U}_p - \mathbf{U} = d_p^2 \frac{(\rho_p - \rho)}{18\mu}\mathbf{a} \tag{3-5}$$

where d_p is the particle diameter, $\mathbf{a}$ is the acceleration of the flow and μ is the viscosity. Another measure of the discrepancy between particle motion and fluid is the step response of particle velocity which typically follows an exponential law.

$$\mathbf{U}_p(t) = \mathbf{U} + \mathbf{U}_{lag} \exp\left(-\frac{t}{\tau}\right) \tag{3-6}$$

where τ is given by:

$$\tau = d_p^2 \frac{\rho_p}{18\mu} \tag{3-7}$$

The relaxation time τ is a measure for the tendency of particles to adapt to the flow velocity. The time response expressed by equation (3-6) is illustrated in Figure 3.3 for various particle diameters. Note that the simple expressions above for particle motion only apply if the flow is continuously accelerating and the particles can be assumed to be experiencing Stokes drag. If this is not the case the equations of motion for the particles become more difficult to solve. Nevertheless, τ remains an indication of how well particle motion corresponds to the actual velocity of the fluid. Apart from selecting tracing particles based on their mechanical

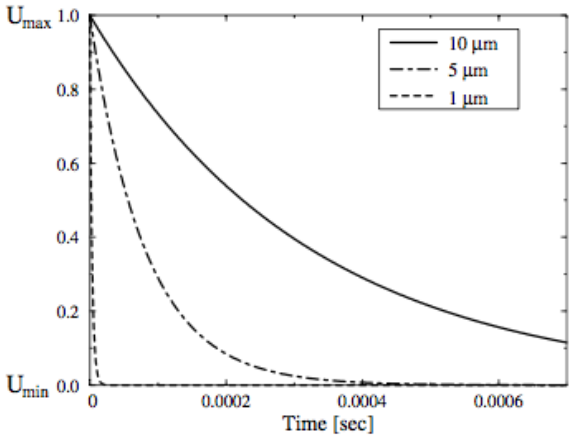

Figure 3.3: Time response of oil particles in a decelerating air flow(Raffel et al. [2007]).

properties it is necessary to consider their light scattering behavior, because the quality of the recorded images depends for a large part on the amount of light collected. As particles become smaller they scatter less light and are thus more difficult to capture on image. Hence it is not possible to simply opt for the smallest particles available, because although they will follow the flow very well, they might be too hard to detect.

3.2.2 Light source

Lasers are a commonly used light source in PIV experiments because of their ability to emit monochromatic light with high energy density. They can be easily shaped into thin sheets to illuminate particles in a certain plane located in the flow without chromatic aberrations. Figure 3.4 is an example of an optical setup that can manipulate a laser pulse such that a thin light sheet is formed in the region of interest.

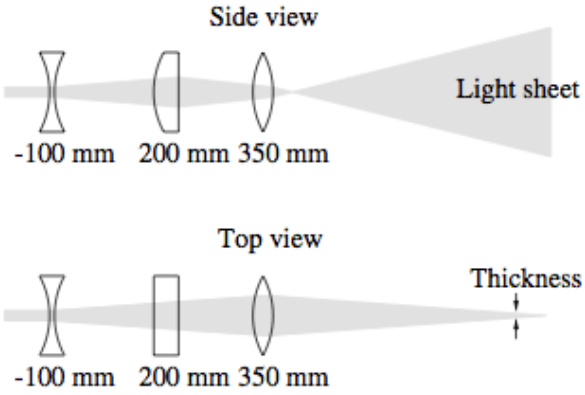

Figure 3.4: Light sheet optics with two spherical lenses and on cylindrical lens (Raffel et al. [2007]).

3.2.3 Image recording

Nowadays digital image recording is the preferred method of capturing the flow field. For this a wide variety of electronic image sensors is available. The most commonly used sensor is the Charge Coupled Device, or CCD. When exposed to light, it converts the photons into an electric charge. The accumulated charge depends on the collected amount of light during the exposure time. A CCD camera contains a sensor that consists of an array of these individual CCD elements (pixels). By reading out the electric charge for all the array elements the recorded image can be reconstructed.

3.2.4 Evaluation of particle motion

The basic steps involved in the process of obtaining a velocity field from the recorded images are as follows.

1. The entire image is partitioned into smaller cells called **interrogation windows**. Every interrogation window should contain a statistically significant number of particles (typically > 10, Raffel et al. [2007]) from which a velocity estimate can be extracted. Furthermore every interrogation window is treated as an individual measurement volume where a local velocity vector is determined. As such the size of an interrogation window affects the resolution of the resulting velocity field.

2. For every image pair their corresponding interrogation windows are subjected to a **cross-correlation analysis**. The output of every analysis is a cross-correlation map with the distance between the maximum and the origin being an indication of the average particle displacement of the corresponding interrogation window. This process is illustrated in Figure 3.5. Because the cross-correlation map is discrete, a peak can only be found at integer pixel shifts. To achieve higher accuracies the position of the peak must be interpolated using sub-pixel estimation methods.

3. In the previous step the average displacement of the particles in a certain window has been evaluated in terms of pixels. Knowing the image magnification, the displacement in pixels can be **scaled to the actual displacement**. The average particle velocity in an interrogation window is then found by **dividing the displacement by the time separation** between the two images.

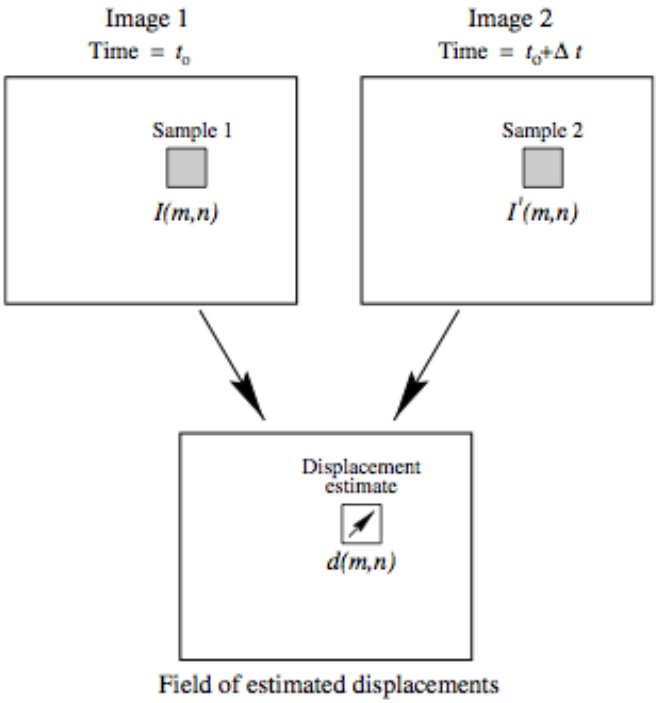

Figure 3.5: Cross-correlation analysis for corresponding interrogation windows (Raffel et al. [2007]).

Chapter 4

Experimental apparatus and setup

All wind tunnel experiments are performed at the High Speed Laboratory of Delft University of Technology. This chapter describes all the equipment that is used during the experiments. Furthermore an overview is given of the test campaigns undertaken along with all the relevant parameters and settings characterizing the experiments.

4.1 Flow facility

The experiments are carried out in the TST-27 wind tunnel (Figure 4.1) at the High Speed Laboratory of Delft University of Technology. The TST-27 (TST stands for Transonic-Supersonic Tunnel and 27 is the maximum height of the test section in cm) is used for measurements in the transonic-supersonic regime and is capable of generating Mach numbers from 0.5 to 4 in the test section. The blow-down tunnel is driven by dry, oil-free air and has a maximum running time of 300 seconds. The test section is 280mm wide and its height ranges between 250mm and 270mm depending on the desired Mach number. Supersonic Mach numbers are set by means of a continuously variable throat and flexible upper and lower nozzle walls (indicated in Figure 4.2) and it is possible to vary the Mach number during a run. Subsonic Mach numbers are controlled using a variable choke section in the outlet diffuser. Small deviations of the Mach number during a run are corrected by automatic fine adjustment of the choke. The maximum unit Reynolds number varies from 38 million per meter in the transonic range to 130 million per meter at Mach = 4. Total pressure p_0 and temperature T_0 in the settling chamber are approximately 2bar and 285K respectively.

Figure 4.1: TST-27 wind tunnel.

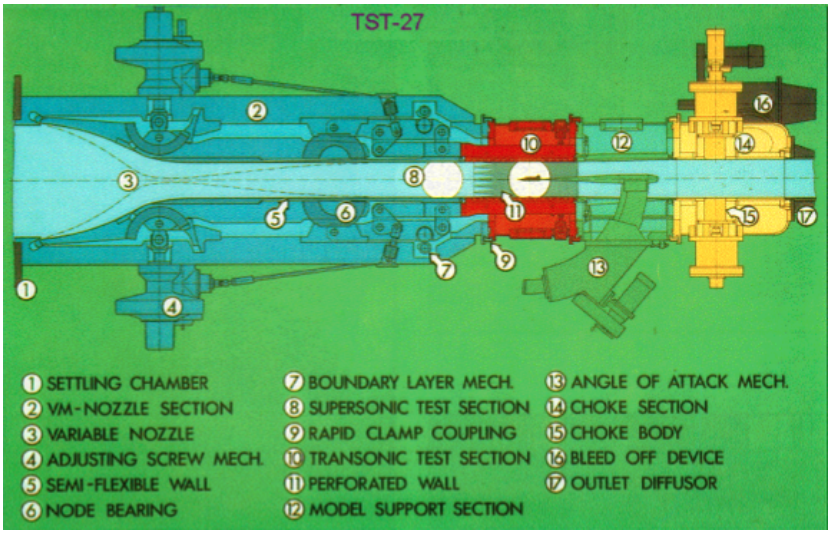

Figure 4.2: Topview schematic of the TST-27.

4.2 Model

In order to investigate launcher baseflow a generic wind tunnel model was designed, shown in Figure 4.3 and 4.4. Care was taken to design the sting, made of stainless steel, such that it would have negligible influence on the flow in the wake of the model. The sting support is mounted in one of two windows that give optical access to the test section. It is equiped with a mechanism giving easy control over the spanwise positioning of the model inside the test section. Being able to move the model allows PIV measurements to be taken in different planes without having to adjust the laser optics, which makes the alignment of the whole system much easier. The model itself is made of anodized aluminium and its surface is covered with a black coating to reduce the intensity of laser reflection. On the nose of the model a tripping strip is applied to ensure that the boundary layer is fully turbulent at separation. The strip is in the shape of a sawtooth pattern with a wavelength of 5mm and amplitude of 5mm. The thickness of the strip is 0.32mm. Furthermore the distance between the strip and the base of the model is 210mm.

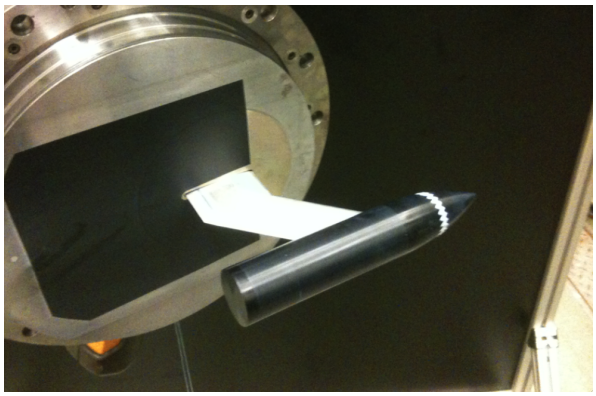

Figure 4.3: The wind tunnel model fitted with a blunt base and trip-strip applied on the nose.

The dimensions of the model are shown in Figure 4.5 as well as the used coordinate system during the experiments. The basic model is 260mm in length and has a base diameter of 50mm. However the back of the model is removable so that different bases can be fitted. Two types of bases are used in the experiments: the basic blunt base (see Figure 4.3) and a base with a smaller cylindrical afterbody extending downstream up to twice the base diameter (see Figure 4.4a). The diameter of this afterbody is 20mm and the extension of the afterbody can be varied as necessary. The ratio between afterbody diameter and base diameter equals $D_{ratio} = 0.4$. D_{ratio} is chosen such that it corresponds to the geometry used in Deck and Thorigny [2007] and Weiss et al. [2009]. These studies concerned a CFD analysis of afterbody flows at similar flow conditions as in the current project. Hence they serve as a suitable reference with regard to comparing and validating the results.

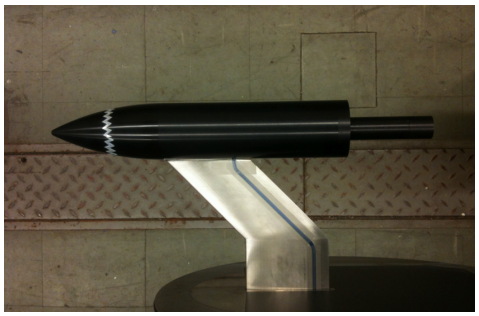

(a) The wind tunnel model with afterbody and trip-strip applied on the nose.

(b) Inside the model.

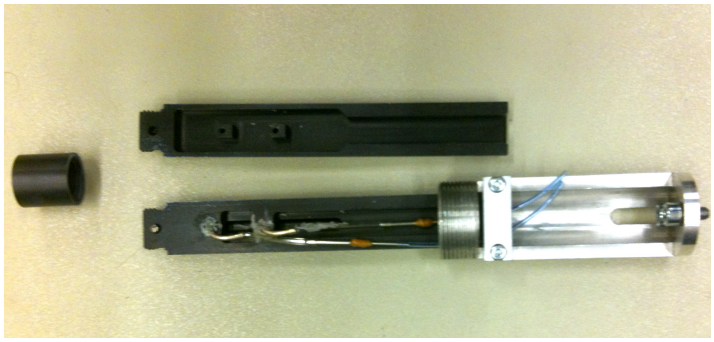

(c) Inside the afterbody: two pressure tubes glued to pressure ports.

Figure 4.4: Model afterbody

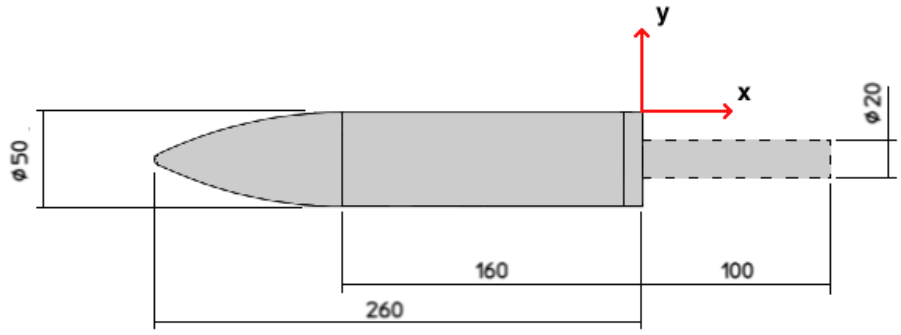

Figure 4.5: Model dimensions and definition of coordinate system.

Static pressure ports

Originally the model was designed such that small dynamic pressure transducers could be installed in the afterbody. For this 1.6mm holes were drilled in the afterbody surface which lead to inner cavities that would contain the pressure transducers. Dynamic pressure transducers are able to accurately measure high frequency fluctuations in the pressure. For the purposes of the current project however, only the mean static pressure is required, so that small dynamic transducers are not needed inside the model. Consequently the cavities meant for the dynamic transducers are simply fitted with pressure tubes instead (see Figure 4.4), which lead through a channel in the sting to existing transducers located outside the test section.

During the experiments two pressure ports in the afterbody of the model are used. The ports are spaced 20mm from each other and are connected to transducers outside the test section. The transducers are of the type *PDCR 42* manufactured by *Druck*. They have a operating pressure range between 75mbar and 35bar. Both gauge (i.e. with respect to ambient pressure) or differential pressure (i.e. pressure difference between two points) measurements are possible.

Figure 4.6: Pressure transducer used *(Courtesy of proconsystems.com)*.

4.3 Flow imaging system

4.3.1 Seeding

For the PIV experiments the flow is seeded with titanium dioxide (TiO_2) particles of the type *UV-Titan L830* produced by *Kemira*. The mean diameter of the particles is 50nm and the bulk density is 200kg/m^3. The particles are injected into the settling chamber with a cyclone generator (see Figure 4.7) at the start of a run and are carried into the test section with the flow.

Note that unlike PIV, BOS does not require actual seeding of the flow, but requires a background image that distorts due to refraction effects caused by flow density variations. For this background image, a piece of paper printed with a synthetic seeding pattern is used.

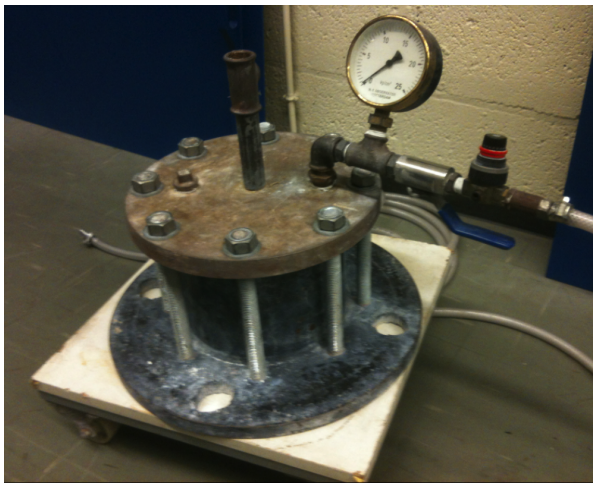

Figure 4.7: Cyclone generator used for seeding.

4.3.2 Illumination

For the BOS experiments a simple halogen lamp is sufficient to provide the required lighting of the background image. Under normal circumstances it is preferred to have two opposing windows in the test section providing optical access. The background image is then mounted on one of the two windows with the light source behind it and the camera observing from the opposing side, so that no shadows of the model are formed on the background image. However in the current experiment only one window is available, since the sting support of the model replaces one window. Hence the halogen lamp is mounted on the same side of the camera. By illuminating the background at an angle though, it is possible to avoid the presence of shadows within the observed region.

Two light sources are used for for the PIV experiments. The first one is the *Big Sky CFR PIV-200 Nd: YAG* laser shown in Figure 4.8. It operates in the green region of the optical spectrum at a wavelength of $\lambda = 532$nm, providing 200 mJ/pulse of power. Furthermore it has a maximum repitition rate of 20Hz and a pulse duration of 7ns. Due to maintenance issues on this laser, some experiments are performed with a replacement laser which is the *Spectra-Physics Quanta-Ray PIV-400 Nd: YAG* shown in Figure 4.9. It also operates at $\lambda = 532$nm but can provide 400 mJ/pulse of power. Repetition rate goes up to 10Hz and pulse duration is in the range of 5-10ns.

Each laser pulse is guided into the wind tunnel through a probe that is mounted downstream of the test section. Inside the probe the laser passes through a set of mirrors and lenses that shape the laser beam into a diverging sheet before it is released into the test section in upstream direction thereby illuminating the seeding particles in a certain plane of interest.

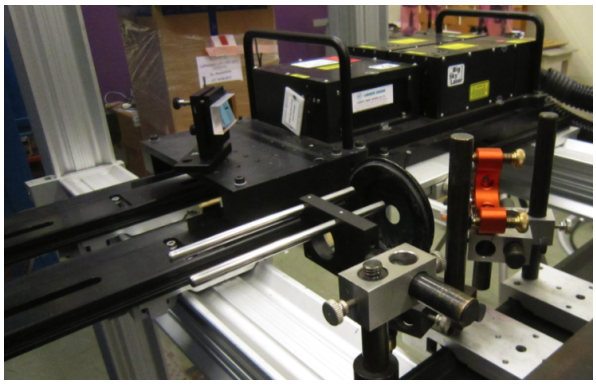

Figure 4.8: BigSky laser

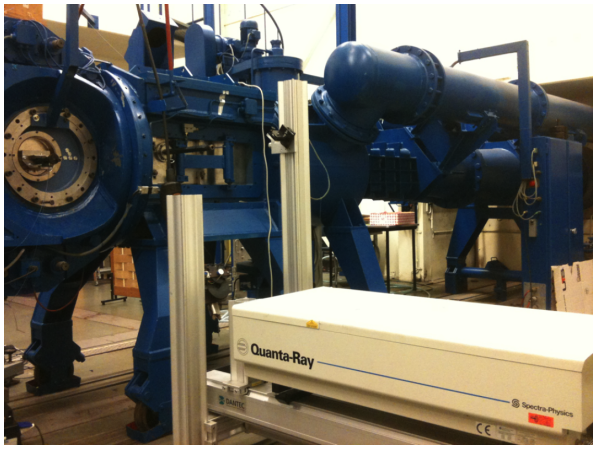

Figure 4.9: Quanta-Ray laser

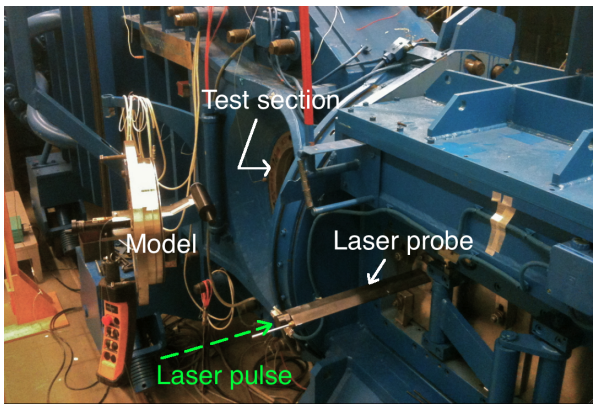

Figure 4.10: The laser probe is mounted to the side of the wind tunnel and guides the laser pulse into the test section.

4.3.3 Recording devices

Two types of CCD cameras are used during the project to capture the flow field. These are the *Imager Pro LX* and the *Imager Intense*, both manufactured by *Lavision* (see Figure 4.11). For the BOS experiment the Imager Pro LX is used, fitted with a 50mm Nikon lens. During the PIV experiments two Imager Intense cameras are used in combination with 50mm, 60mm and 200mm Nikon lenses depending on the purpose of the particular experiment. In addition, daylight filters are attached to the lenses to filter out any ambient light other than the green laser, thereby reducing the noise level in the images. Camera specifications are shown in Table 4.1.

(a) Imager Pro LX *(Courtesy of Lavision)*

(b) Imager Intense *(Courtesy of Lavision)*

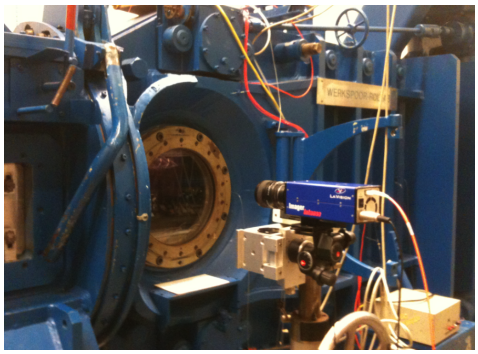

(c) setup of camera

Figure 4.11: Lavision PIV cameras used for the experiment

	Imager Pro LX	Imager Intense
resolution	4900 x 3300pixel	1376 x 1040pixel
pixel size	7.4 x 7.4μm^2	6.45 x 6.45μm^2
framerate	5Hz	10Hz
min. exposure time	600ns	500ns
dynamic range	12bit	12bit

Table 4.1: Flow parameters.

4.4 Experimental setup

The schematic in Figure 4.12 illustrates the geometric arrangement of the model, laser and camera with respect to each other. The model is shown in the test section mounted to the wall where normally a window is located. Downstream of the test section a probe with laser optics enters the tunnel through the wall. It guides the laser pulse which is generated externally, into the wind tunnel. A combination of mirrors and lenses inside the probe shape the laser pulse into a vertical diverging sheet running upstream through the test section as shown in Figure 4.12. Finally a camera observes the flow in the plane illuminated by the laser sheet.

Figure 4.13 shows a top view of the test section with the model inside. As can be seen from the figure it is not possible to observe the front of the model. The camera's field of view is limited by the size of the window and since the base area is the focus of the project, the model is installed such that it can be clearly viewed by the camera.

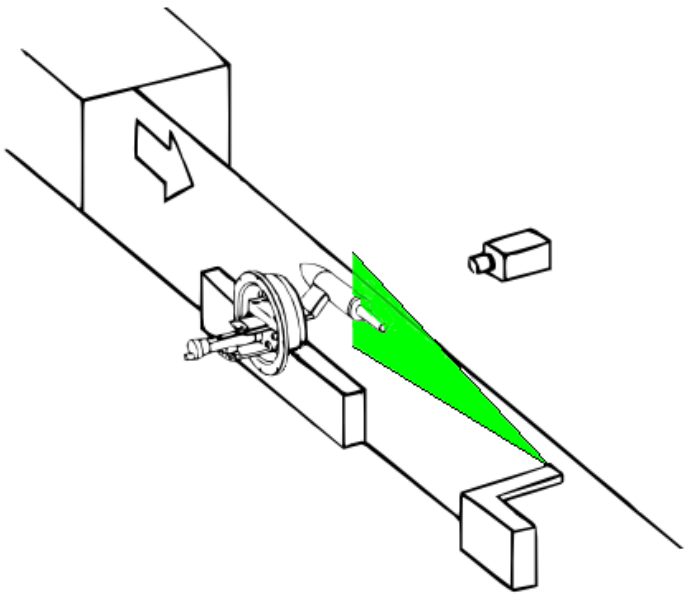

Figure 4.12: Geometric arrangement of the experiment in the TST-27.

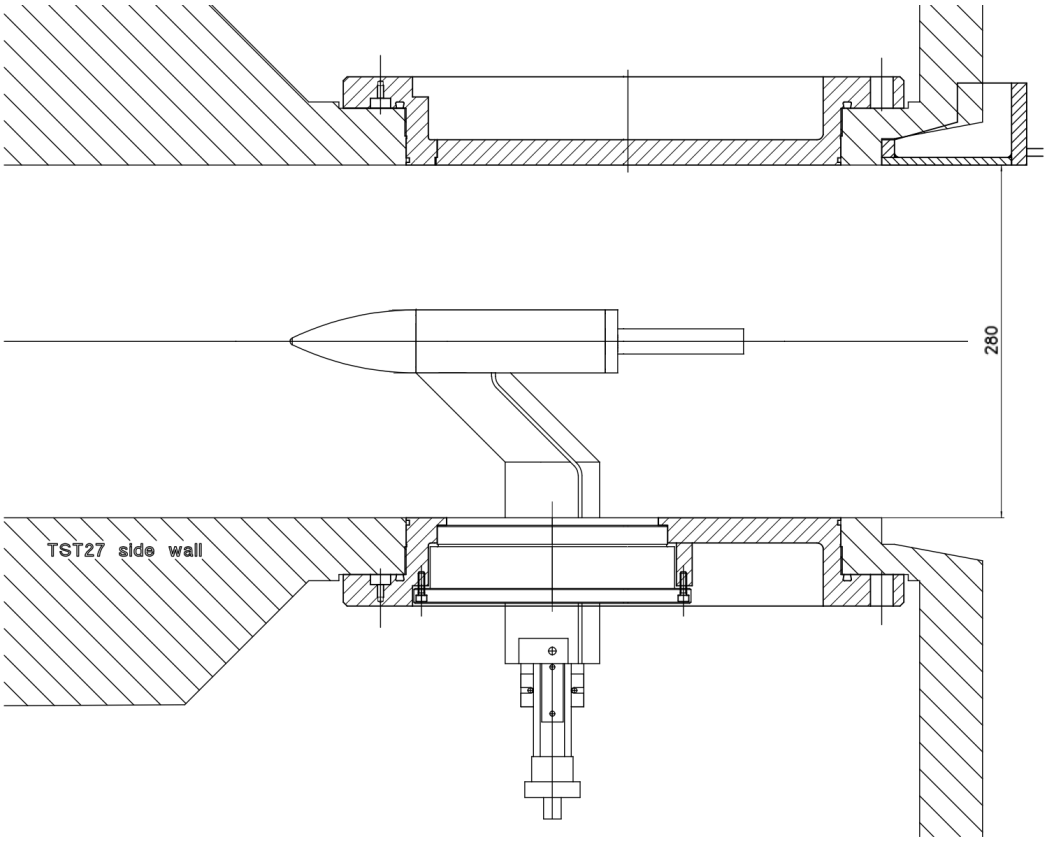

Figure 4.13: Topview of the model inside the wind tunnel test section.

4.5 Flow parameters

The TST-27 is driven by dry, oil-free air for which, given the conditions in the wind tunnel, we can assume a specific heat ratio $\gamma = 1.4$ and a specific gas constant of $R = 287\,\mathrm{Jkg^{-1}K^{-1}}$. Flow conditions at the start of the wind tunnel test section (upstream of the model) are referred to as 'free stream' conditions denoted by a subscripted ∞ symbol. For all experiments the TST-27 is run at the same Mach number, namely $M_\infty = 0.7$. Since the total pressure and total temperature in the settling chamber are known measured values, all relevant free stream conditions can be determined using the ideal gas law (equation (4-1)), the energy equation for adiabatic flow (equation (4-2)), isentropic flow relations (equation (4-3)) and the power law approximation of the viscosity in dilute gases (equation (4-4)).

$$p = \rho R T \tag{4-1}$$

$$\frac{T_0}{T} = 1 + \frac{\gamma - 1}{2} M^2 \tag{4-2}$$

$$\frac{p_0}{p} = \left(\frac{\rho_0}{\rho}\right)^{\gamma} = \left(\frac{T_0}{T}\right)^{\frac{\gamma}{(\gamma-1)}} \tag{4-3}$$

$$\mu = \mu_0 \left(\frac{T}{T_0}\right)^{0.67} \tag{4-4}$$

M_∞	0.7	-
V_∞	224	m/s
μ_∞	$1.67 \cdot 10^{-5}$	$Pa \cdot s$
Re_D	$1.3 \cdot 10^6$	-
p_0	$2 \cdot 10^5$	Pa
T_0	285	K
γ	1.4	-
R	287	$\mathrm{Jkg^{-1}K^{-1}}$
D	50	mm

Table 4.2: Flow parameters.

The Reynolds number based on the diameter of the model base Re_D is computed as

$$Re_D = \frac{\rho_\infty V_\infty D}{\mu_\infty} \approx 1.3 \cdot 10^6 \tag{4-5}$$

where ρ_∞, V_∞ and μ_∞ are the free stream density, velocity and dynamic viscosity respectively and D is the base diameter of the model. Experimental flow parameters are summarized in Table 4.2.

4.6 BOS experiments

The BOS experiments are carried out using the Imager Pro LX camera fitted with a 50mm Nikon lens. A reference image is shot with the wind tunnel off. Then a series of images are recorded at Mach 0.7. Figure 4.14 shows the field of view (FOV) used in the experiments. All of these images which contain distortions of the background due to density gradients in the flow are then cross-correlated with the reference image and the results are averaged. The resulting average displacement field is proportional to the mean density gradient field, thus giving a qualitative idea of how the density varies across the region of interest. Obtaining actual density fields is not the focus of the project, therefore further processing of the data is not performed. Additional settings during the experiment can be found in Table 4.3 - 4.6.

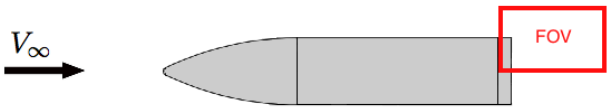

(a) blunt based configuration.

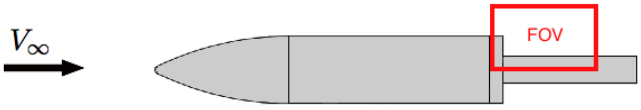

(b) afterbody configuration.

Figure 4.14: Used field of view in the BOS experiments.

4.7 PIV test campaign

The PIV experiments make use of the Imager Intense cameras. All tests are performed at Mach 0.7. The new model has never been used before and the actual influence of the sting on the flow is yet unknown. The first series of experiments are thus performed to assess the influence of the sting and to see if the flow around the model is indeed axissymmetric. This is done by taking measurements at five equally spaced planes. They are distributed in spanwise direction with respect to the center plane of the model ranging from -30mm to +30mm as illustrated in Figure 4.15.

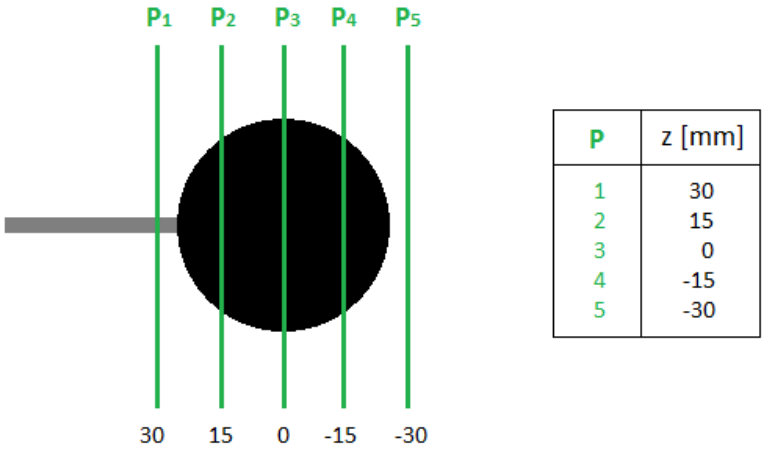

P	z [mm]
1	30
2	15
3	0
4	-15
5	-30

Figure 4.15: Backview of the model illustrating the measurement planes chosen for the planar PIV experiments.

The velocity fields of the different planes are compared to assess the effect of the sting. If the sting indeed has negligible influence on the wake then the flow is axissymmetric. This will then be reflected in the obtained velocity fields which will be symmetric with respect to the center plane of the model. In these first experiments the recording of the images is done with two cameras of the type Imager Intense fitted with 50mm Nikon lenses. The second

camera is aimed at a region next to the one observed by the first camera, thus increasing the effective field of view. A slight overlap is maintained between the two separate field of views of both cameras, to make it easier to combine the PIV data obtained from both cameras into a single flowfield. As indicated in Figure 4.16a the FOV of both cameras is used to obtain a combined FOV that is able to capture more of the downstream wake. In addition the state of the boundary layer near the separation is investigated, since it determines the initial development of the shear layer. The FOV used is indicated in Figure 4.16b as FOV BL. One Imager Intense is used with a 200mm Nikon lens for a more suitable magnification to observe the boundary layer.

When the effect of the sting has been evaluated and the state of the boundary layer is determined, the focus is turned towards obtaining PIV data suitable for pressure evaluation. Considering the axis symmetric nature of the flow, it is sufficient to determine the pressure field in the center plane of the model. This is discussed in Chapter 6. The PIV experiments for the pressure evaluation in the center plane are performed with the blunt based configuration as well as the afterbody configuration of the model. One Imager Intense camera with a 60mm Nikon lens is sufficient to capture the relevant flow region. Now the FOV for the blunt configuration as well as the afterbody configuration correspond to FOV1 in Figure 4.16b. Finally Tables 4.3 to 4.7 show the specific settings under which all the experiments are carried out.

(a) blunt based configuration.

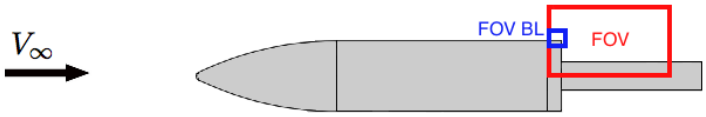

(b) blunt base/afterbody configuration.

Figure 4.16: Used field of view in the PIV experiments.

	Camera1				Camera2			
	Type	f	f#	FOV	Type	f	f#	FOV
BOS	Imager Pro LX	50mm	5.6	6.7x4.4cm	-	-	-	-
2-C PIV Sweep	Imager Intense	50mm	8	7.8x5.9cm*	Imager Intense	50mm	8	7.8x5.9cm*
2-C Centerplane	Imager Intense	60mm	11	9x6.5cm	-	-	-	-
BL	Imager Intense	200mm	2.8	1.1x0.8cm	-	-	-	-
Pressure	-	-	-	-	-	-	-	-
*joined FOV of both camera's is 13.8x5.9cm								

Table 4.3: Camera settings.

	Laser				
	Type	Power	Laser sheet thickness	frequency*	dt
BOS	-	-	-	-	-
2-C PIV Sweep	Big Sky	40-60%	3mm	5Hz	3μs
2-C Centerplane	Quanta-Ray	50%	1mm	5Hz	2.5μs
BL	Big Sky	55%	1mm	5Hz	1μs
Pressure	-	-	-	-	-
*Corresponds to camera recording rate					

Table 4.4: Laser settings.

	Seeding	
	Type	Overpressure
BOS	-	-
2-C PIV Sweep	TiO_2	3.5bar
2-C Centerplane	TiO_2	3.5bar
BL	TiO_2	3.5bar
Pressure	-	-

Table 4.5: Seeding settings.

	Dataset (nr. of frames)		
	Blunt	Short afterbody	Long afterbody
BOS	100	-	100
2-C PIV Sweep	130 per plane	-	-
2-C Centerplane	492	426	422
BL	-	-	100
Pressure	-	-	-

Table 4.6: Number of recorded frames for each experiment.

	PIV processing	
	Window size	Vector pitch
BOS	128x128 (1.6x1.6mm^2)	0.4mm
2-C PIV Sweep	32x32 (2x2mm^2)	0.5mm
2-C Centerplane	24x24 (1.6x1.6mm^2)	0.4mm
BL	32x32 (0.24x0.24mm^2)	0.06mm
Pressure	-	-

Table 4.7: PIV processing.

Chapter 5

Mean flowfield analysis

In this chapter the results from the BOS and PIV experiments are presented and discussed. From the BOS experiment distortion fields are obtained, which without further processing allows for a qualitative overview of the density gradient in the region of interest. The acquired PIV data allows the mean velocity field to be extracted as well as the Reynolds stress components. Furthermore an analysis of the boundary layer ahead of the separation is performed to assess its nature (laminar vs turbulent). This needs to be determined since the state of the boundary layer affects the dynamics of the flapping shear layer that develops after separation. Finally the growth rate of the separated shear layer is estimated and compared to literature.

5.1 Density gradients

The results of the BOS experiment are presented in Figure 5.2 for the blunt configuration and in Figure 5.3 for the afterbody configuration with extension up to $x/D = 2.0$. They show the magnitude of the distortions caused by the flow with respect to the no flow case. As discussed in Chapter 3, these distortions are proportional to the density gradients and thus give an qualitative impression on the density variations across the flow. Consider Snell's law aplied to a flowfield with a positive density gradient as illustrated in Figure 5.1. Snell's law states the relationship between the angle of incidence and refraction when light travels through an interface between two isotropic media of different refractive indices. This also applies to the current situation where light is traveling through air with varying density (density is proportional to refractive index). Simply put, the law implies that when light travels from low to high density air, the angle of refraction is smaller than the angle of incidence. In other words the light ray will bend towards the interface normal and vice versa for the case when light travels from high to low density. From Figure 5.1 it can thus be concluded that regarding distortions in x-direction, a flow with positive density gradient creates distortions in negative x-direction. From a similar analysis for the distortions in y-direction it can be concluded that a positive density gradient leads to distortions in negative y-direction.

With the implications of Snell's law in mind the BOS results are inspected to see whether the plots confirm what is expected to happen in the flow. Consider for instance Figure 5.2a.

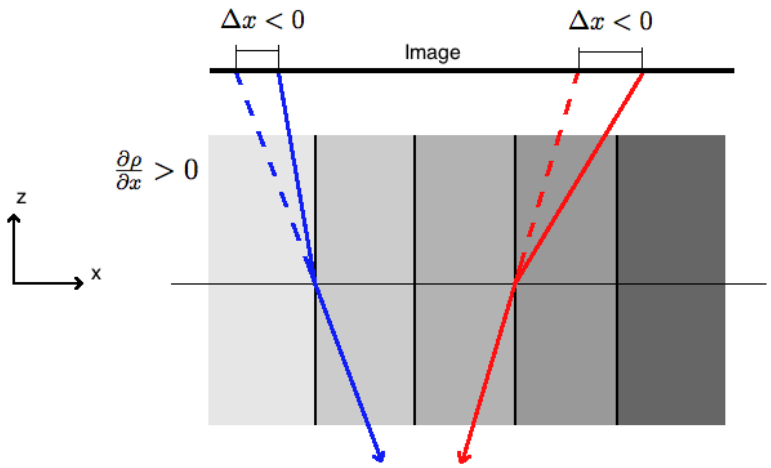

Figure 5.1: Distortion of light rays in a flow with positive density gradient.

Knowing that around the point of separation the flow expands, it is expected that density decreases in downstream direction i.e. a negative gradient is present. This is indeed reflected in Figure 5.2a by a positive x-distortion. Furthermore it is known that the flow reattaches at $x/D \approx 1$ hence in this region the density should increase again which, as shown in Figure 5.2a, is confirmed by the negative distortions. Similary in y-direction it is assumed that the density in the outer flow is higher than in the low pressure recirculation zone. Hence a positive density gradient is expected and this is reflected once again by the negative distortions.

Upon comparison it can be observed that the distortions displayed by the blunt configuration are larger than those of the afterbody configuration. But otherwise the overall distortion field of both configurations appear to be quite similar. The circular organization of the distortion magnitude contours in Figure 5.2c and 5.3c indicating that near the separation point at the base the density gradient is aligned in radial direction i.e. the density decreases in radial direction. This observation supports the notion that near the base, the flow accelerates and consequently expands. From the distortion magnitude it can also be seen that moving in downstream direction the magnitude of the density variations decrease in the outer flow. In addition, it can be observed that the shear layer which separates the outer flow from the inner low pressure region where recirculation occurs, displays the largest density gradients. Finally, Inside the recirculation area there is a local minimum at $x/D \approx 0.6$.

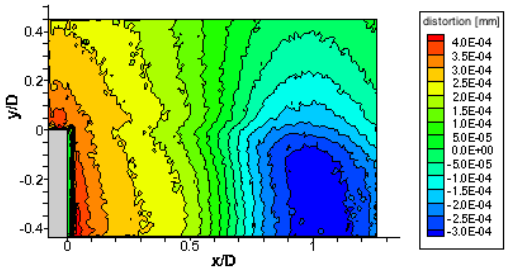

(a) Distortions in x-direction.

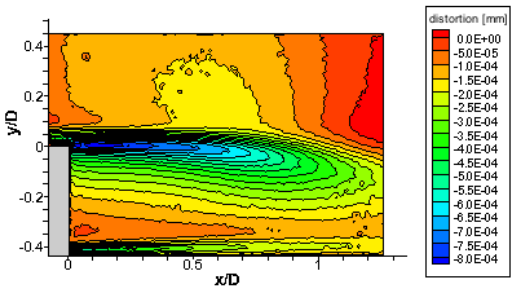

(b) Distortions in y-direction.

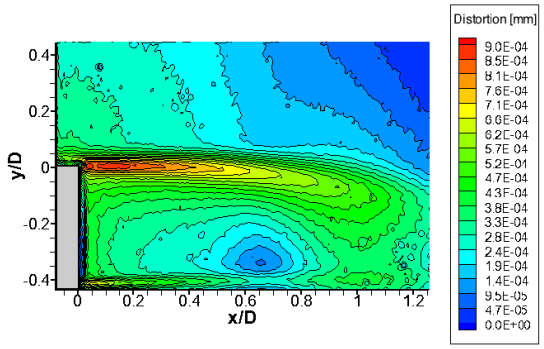

(c) Magnitude of distortions

Figure 5.2: Distortion contours behind the blunt based model.

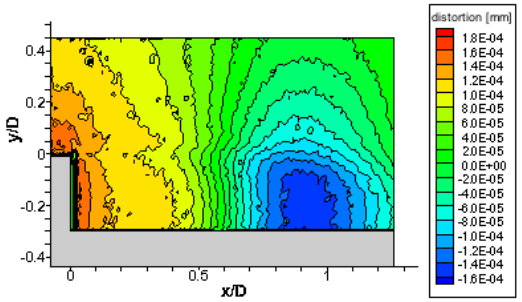

(a) Distortions in x-direction.

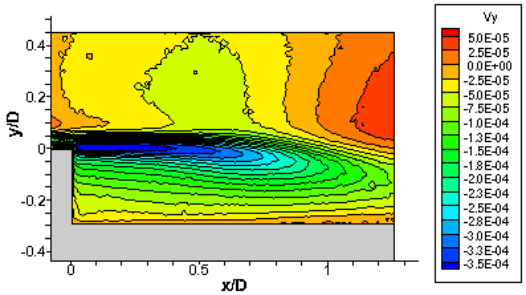

(b) Distortions in y-direction.

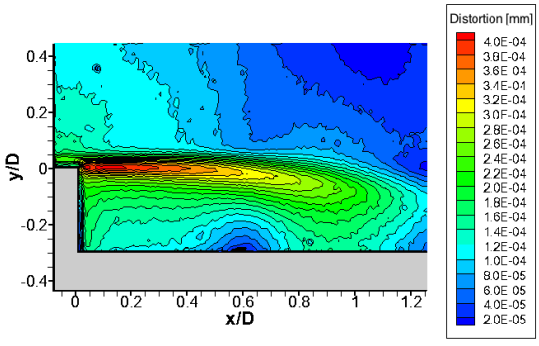

(c) Magnitude of distortions

Figure 5.3: Distortion contours behind the model with afterbody.

5.2 Velocity fields

The tested model configurations during the experiments can be divided in two categories. These are the blunt base and afterbody configuration as discussed in Chapter 4. In the blunt base configuration, the separated shear layers do not reattach anywhere on the model itself again. The point of 'reattachment' is where the shear layers from all sides coincide with each other. Hence this is termed fluidic reattachment. The situation changes when the model is fitted with an afterbody simulating the presence of an exhaust nozzle. When the afterbody extends to well beyond the fluidic reattachment point, the shear layers eventually hit the solid wall of the afterbody. This is referred to as solid reattachment. Finally there is an intermediate case where the afterbody extends to approximately the mean reattachment point itself. Recall that due to the turbulence in the recirculation zone, the reattachment point of the shear layer is continuously oscillating in streamwise direction around the mean reattachment point. Therefore in this intermediate case the nature of the reattachment alternates between solid when the shear layer hits the afterbody upstream of the mean reattachment point and fluidic when the shear layer reaches beyond the end of the afterbody. This is termed the hybrid case.

5.2.1 Mean velocity

Fluidic reattachment

Figure 5.4 shows the mean streamwise velocity in the wake of the blunt based model. The velocity fields are plotted in several planes distributed in spanwise direction. Overall the velocity ranges from approximately 250m/s in the isentropic flow region, to approximately -90m/s in the center of the wake, where the occuring backflow is strongest. The backflow thus reaches up to 40% of the free stream velocity ($V_\infty = 224$m/s). The velocity fields also show that the sting which is attached on the side of positive z, has small influence on the symmetry of the flow. The velocity fields at $z = \pm 15$mm are almost identical, indicating that the influence of the sting is small. Furthermore velocity profiles are shown in Figure 5.5 for the streamwise locations $x/D = 0.2$ and $x/D = 1.0$. The different planes of measurement P1, P2, P3, P4 and P5 correspond to spanwise locations 30mm, 15mm, 0mm, -15mm and 30mm respectively. Once again the velocity profiles at $z = \pm 15$mm agree very well. Moreover the profile at P1 shows the deficit caused by the sting which is approximatly 10m/s and accounts to only 4% of the free stream velocity. These result indicate the negligible influence that the sting has on the wake and hence the flow can be assumed axisymmetric.

In Figure 5.6 the mean velocity field of the blunt configuration is shown. The corresponding streamlines are visualized in Figure 5.7 clearly indicating the area of recirculating flow. The maximum flow velocity is reached outside the recirculation zone shortly downstream of separation where the flow expands. Fluidic reattachment occurs at $x/D \approx 1.1$. Finally the region of strongest backflow occurs halfway of the recirculation bubble.

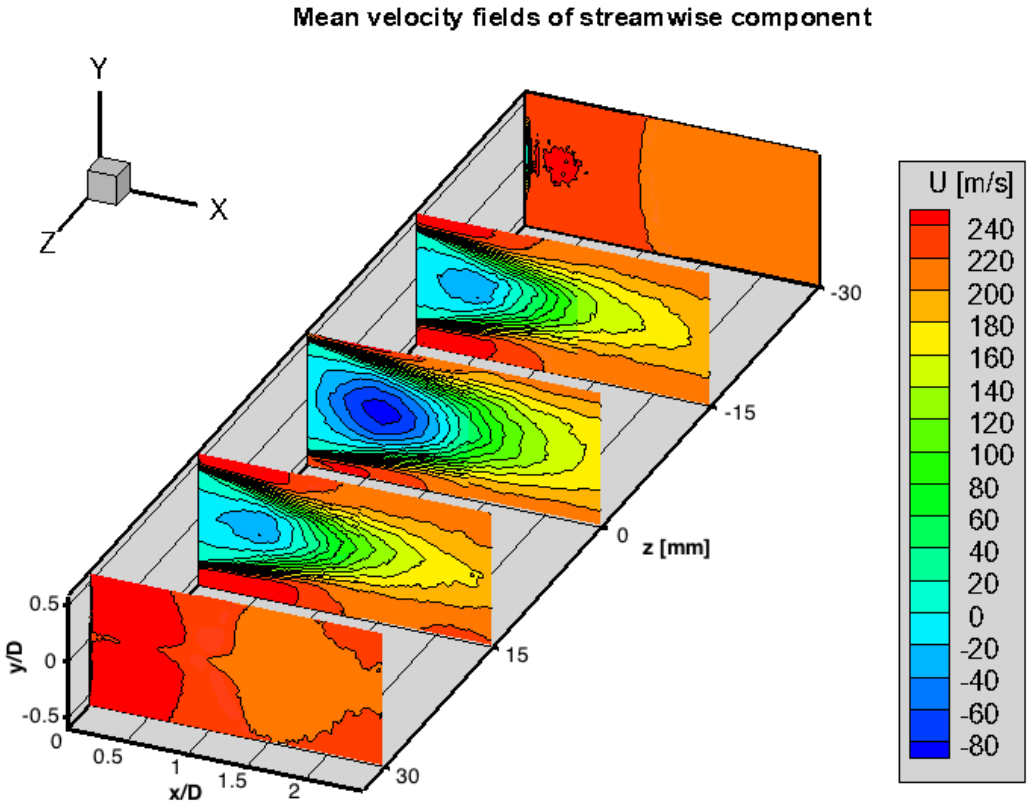

Figure 5.4: Contour plots of the mean streamwise velocity component in the wake of the model in various planes at different spanwise location.

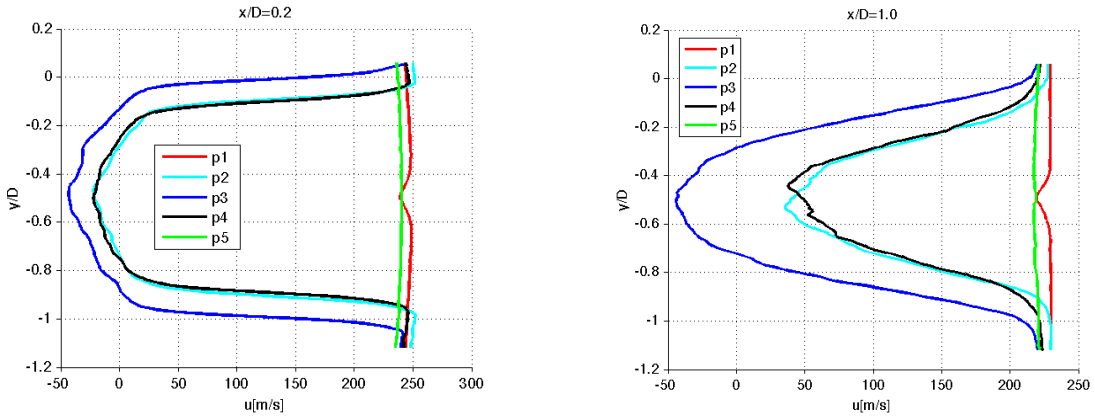

(a) $x/D = 0.2$. **(b)** $x/D = 1.0$.

Figure 5.5: Velocity profiles in the wake.

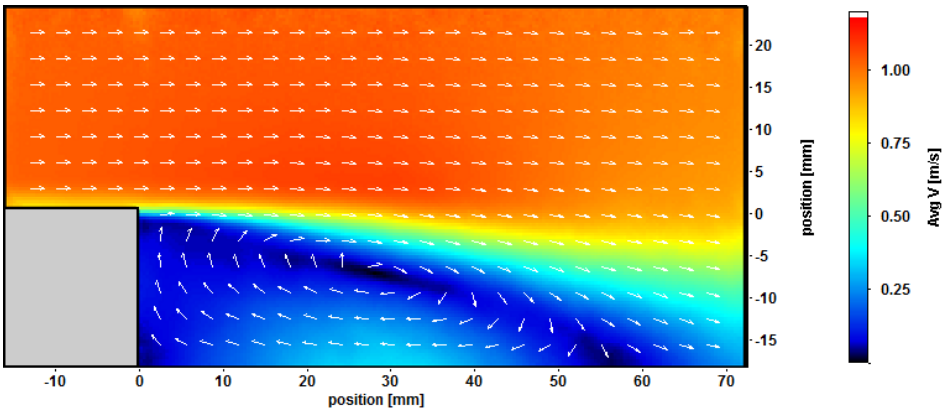

Figure 5.6: Mean velocity field in the center plane for the blunt base configuration.

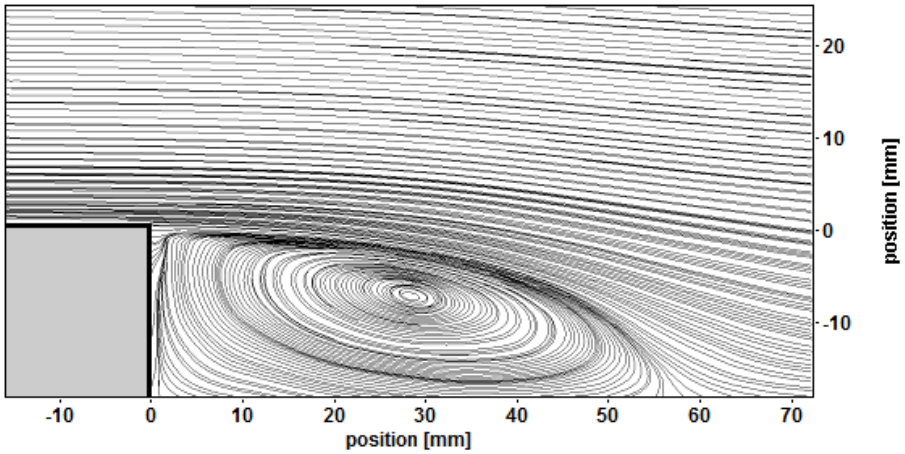

Figure 5.7: Mean velocity field in the center plane for the blunt base configuration.

Hybrid reattachment

The mean velocity field for the short afterbody configuration is presented in Figure 5.8. The blunt based configuration and the base with short afterbody differ in the sense that in the former case the reattachment is completely fluidic, whereas in the latter the shear layer impinges on the end of the afterbody extension. Due to the flapping motion of the shear layer, the reattachment point is not always at the same location. At times the shear layer impinges on the afterbody surface which is referred to as solid reattachment, but alternatively it may be downstream of the afterbody in which case we speak of fluidic reattachment. Therefore this hybrid case combines both types of reattachment. Nonetheless, the resulting mean flowfields are quite similar. The maximum velocity is found outside the separated flow region near the separation point where the flow is expanding. Continuing in streamwise direction where the flow encounters a compression the velocity decreases. The recirculation bubble has the same elliptical shape as before with a region of strong backflow occuring halfway its length. In this case the maximum backflow velocity is found to be around 35% of the free stream velocity. The streamlines of the flow are shown in Figure 5.9. In addition to the main recirculation bubble, the secondary corner vortex can be discerned. The mean reattachment length is estimated at $x/D \approx 1$ which comes close to the value found for the blunt configuration.

Finally the proportion between fluidic and solid reattachment is assessed for this particular test case where the afterbody extends to $x/D = 1.2$. This is done by taking a small 4x4mm^2 interrogation window at the back of the afterbody (blue window in Figure 5.10a) near the surface and computing the spatiial average of the streamwise velocity component for every instantaneous velocity field. For every frame, the resulting velocity is compared to a threshold value in order to determine whether the reattachment point is on or beyond the afterbody. To obtain the threshold value, a 4x4mm^2 window is taken at the actual reattachment point in the mean velocity field (red window in Figure 5.10a). The spatial average over this window is then computed and the resulting streamwise velocity is then taken as the threshold value. If the instantaneous velocity at the back of the afterbody is less than the threshold value, there is most likely to be an increase in backflow within the interrogation window. Consequently this indicates that the recirculation area extends beyond the afterbody and hence reattachment is fluidic. However if the velocity is larger than the threshold value, this implies that the shear layer impinges upstream of the mean reattachment point and hence we have solid reattachment. This criterion for determining whether reattachment is solid or fluidic, results for this test case in 18% fluidic reattachment. This is visualized in Figure 5.10b where the instantenous velocities are plotted together with the threshold value.

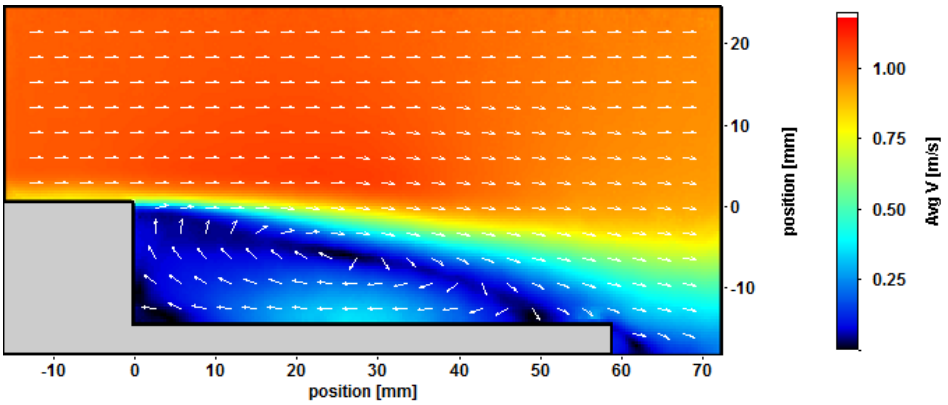

Figure 5.8: Mean velocity field in the center plane for the blunt base configuration.

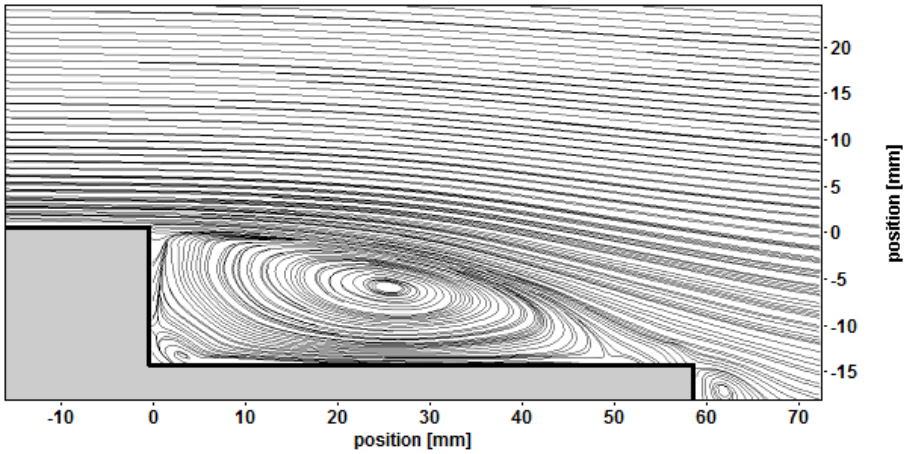

Figure 5.9: Mean velocity field in the center plane for the blunt base configuration.

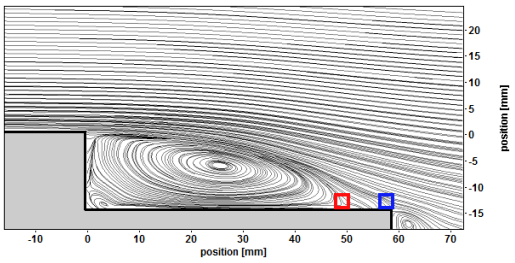

(a) Threshold velocity (red window) and instantaneous velocity (blue window).

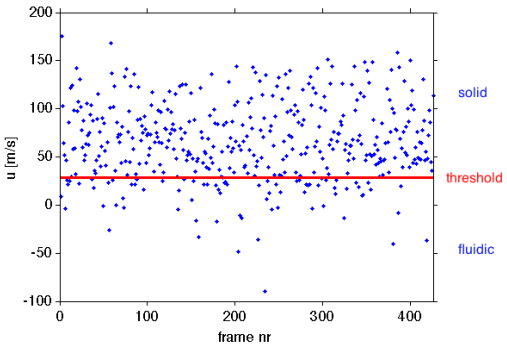

(b) Instantaneous streamwise velocity at the end of the afterbody.

Figure 5.10: Determining solid vs fluidic reattachment ratio.

Solid reattachment

With the long afterbody extending up to $x/D = 2.0$ from the base, the reattachment is completely solid. From inspecting the velocity field in Figure 5.11 and the streamlines in Figure 5.12, no substantial differences are observed compared to the case of hybrid reattachment. The maximum backflow velocity appears to be around 35% as well and the mean reattachment point at $x/D \approx 1$. Furthermore the overall velocity field and the point of reattachment is in accordance with the findings in Bitter et al. [2010] which concerned an extensive PIV study with the same test configuration. At $M_\infty = 0.7$ and $Re_D = 1.0 \cdot 10^6$ their experiment produced the mean velocity field shown in Figure 5.13, which was based on a data set of 8000 instantaneous velocity fields. Also in Bitter et al. [2010] the maximum back flow was found to be around 35%. Their reattachment point however seems to be located slightly further downstream nearing $x/D = 1.1$ rather than $x/D = 1$ as found in the current experiement. Nevertheless it is evident from the good agreement between the results that the much smaller data set used in the current experiment (422 instantaneous velocity fields) is sufficient to accurately resolve the mean velocity field.

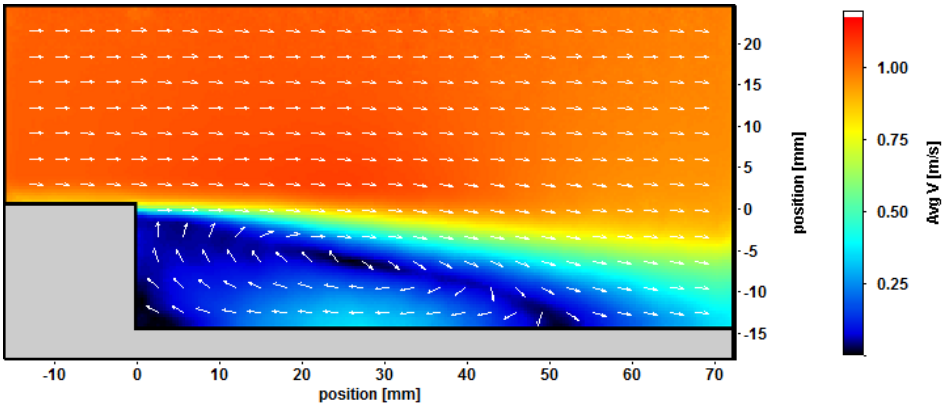

Figure 5.11: Velocity magnitude and streamlines in the center plane for the base with afterbody configuration.

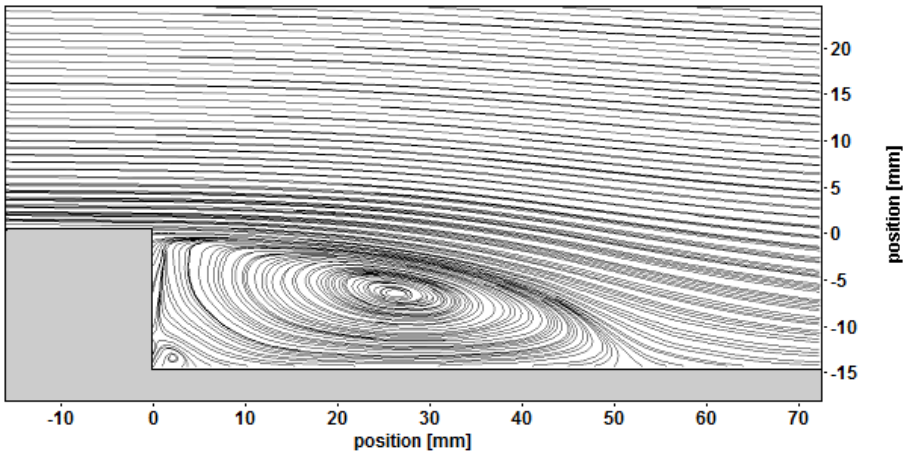

Figure 5.12: Mean velocity field in the center plane for the blunt base configuration.

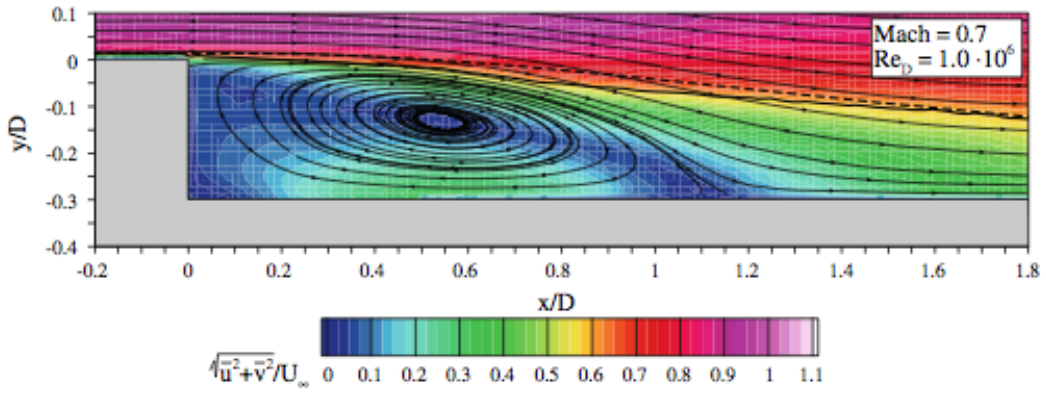

Figure 5.13: Mean velocity field as evaluated by Bitter et al. [2010]

5.2.2 Reynolds stresses

Fluidic reattachment

Figure 5.14 shows the different Reynolds stress components obtained. The magnitude of the streamwise Reynolds stress component $\overline{u'u'}$ is the largest reaching up to approximately 0.08 after normalization with V_∞. The transverse component $\overline{v'v'}$ remains below 0.06. Another difference between the streamwise and transverse Reynolds stresses is that $\overline{u'u'}$ is largest near the edge of the wake, whereas the transverse component $\overline{v'v'}$ is most prominent near the centerline of the wake and downstream of reattachment. Unlike the normal stress components which are always positive, the Reynolds shear stresses can be both positive and negative. As can be seen in Figure 5.14c the normalized shear stress reaches -0.04 (note that the plot shows $-\overline{u'v'}$). The fact that this component is negative can be interprested as follows. Consider the shear layer which develops between a high velocity flow above it and a low velocity recirculation bubble below it. In the mean sense it can thus be stated that if a fluid particle in the high velocity flow is subject to a negative velocity fluctuation in y-direction, it moves downward into the shear layer carrying with it a velocity higher than the local mean velocity in the shear layer. Consequently this causes a positive u' fluctation. Likewise when a fluid particle moves upward due to a positive v' fluctuation, a negative u' fluctuation will be experienced because the fluid particle has a lower u velocity than the local u velocity. Hence in the upper shear layer u' and v' are negatively correlated leading to negative Reynolds stresses as confirmed by Figure 5.14c. Finally the overall turbulence intensity $\frac{\sqrt{\frac{\overline{u'u'}+\overline{v'v'}}{2}}}{V_\infty}$ is presented in Figure 5.14d.

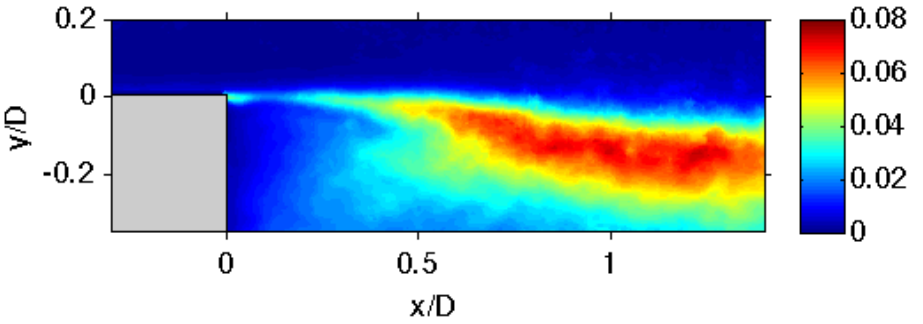

(a) $\frac{\overline{u'u'}}{V_\infty^2}$.

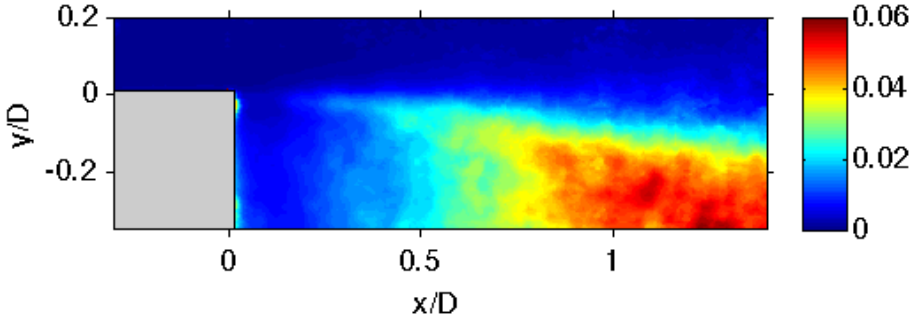

(b) $\frac{\overline{v'v'}}{V_\infty^2}$.

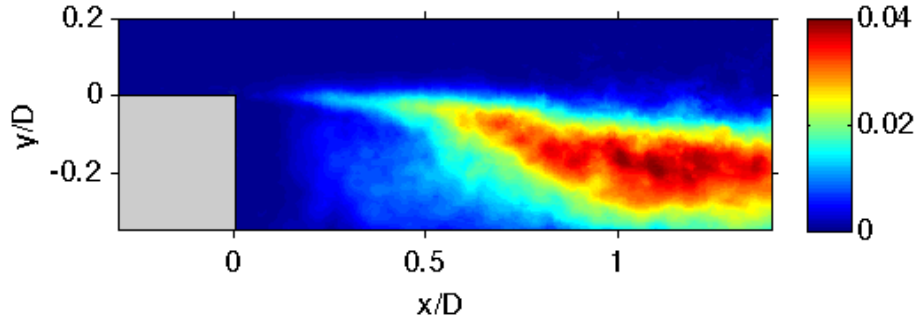

(c) $-\frac{\overline{u'v'}}{V_\infty^2}$.

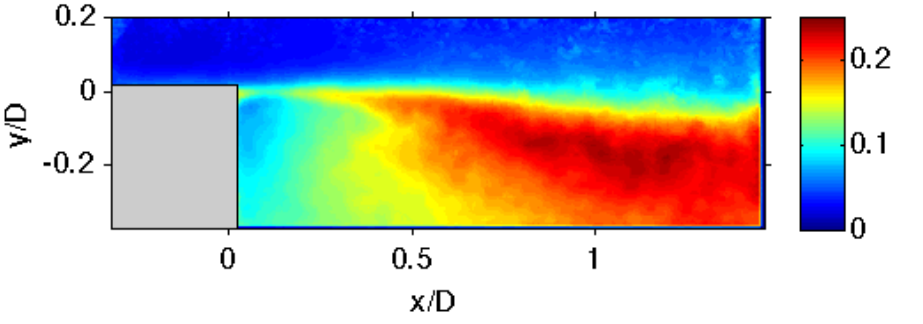

(d) $\frac{\sqrt{\frac{\overline{u'u'}+\overline{v'v'}}{2}}}{V_\infty}$.

Figure 5.14: Reynolds stresses for the blunt based configuration.

Hybrid reattachment

In the configuration with the short afterbody, the mean reattachment point of the shear layer is at the end of the afterbody. It appears that this causes a reduction in the Reynolds stress terms. Contrary to the blunt configuration, in this case the streamwise component goes up to 0.06 instead of 0.08, the maximum transverse component is approximately 0.035 instead of 0.06 and the shear stress is found to be -0.03 instead of -0.04. The overall decrease in the intensity of the fluctuation seems to be a direct result of the presence of the afterbody. Moreover it should be noted that the largest reduction in fluctuation intensity is in the transverse component. This can be explained by noting that the afterbody impeding the flow mostly in transverse direction, would naturally have the largest impact on the fluctuations in y-direction. Since the individual Reynolds stresses are smaller compared to the blunt configuration, the turbulence intensity is reduced as well.

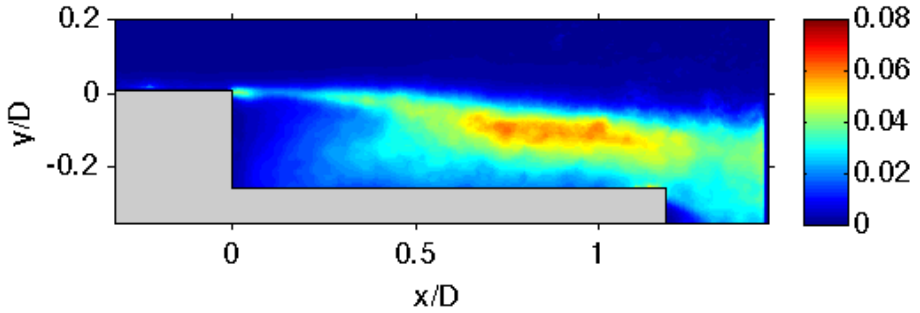

(a) $\frac{\overline{u'u'}}{V_\infty^2}$.

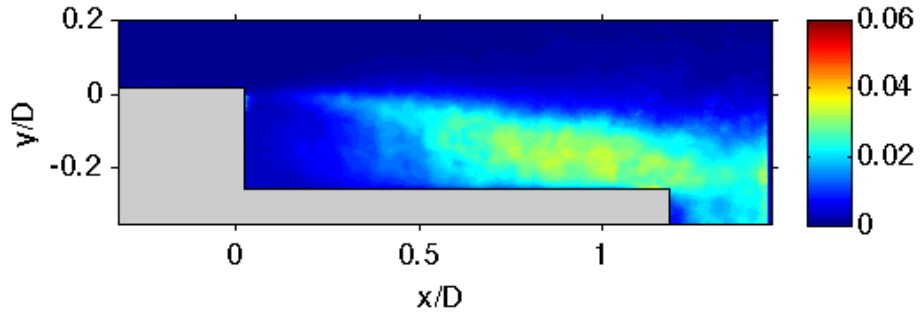

(b) $\frac{\overline{v'v'}}{V_\infty^2}$.

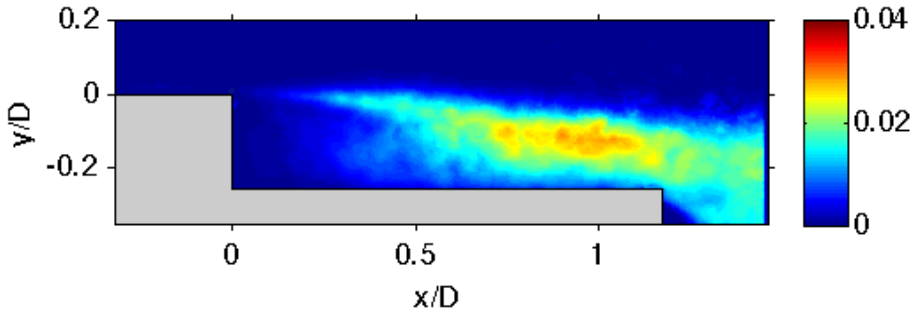

(c) $-\frac{\overline{u'v'}}{V_\infty^2}$.

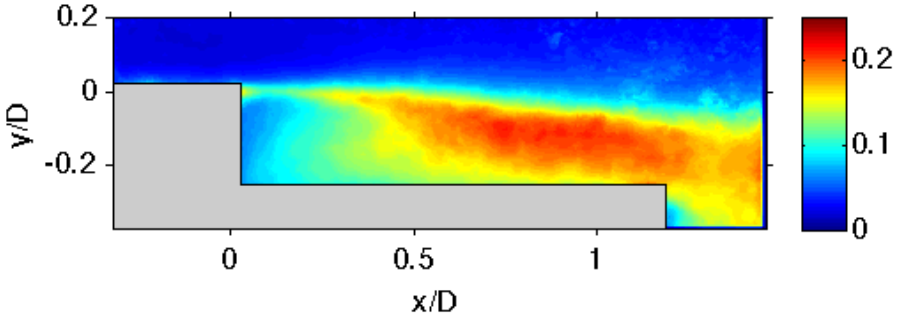

(d) $\frac{\sqrt{\frac{\overline{u'u'}+\overline{v'v'}}{2}}}{V_\infty}$.

Figure 5.15: Reynolds stresses for the short afterbody configuration.

Solid reattachment

In Figure 5.17 the results are shown for the case where there is complete solid reattachment. It can be seen that the flow behaves in a quite similar way to the hybrid case with combined fluidic and solid reattachment. The respective Reynolds stresses are of approximately the same magnitude. The result shown in Figure 5.16 is obtained by Bitter et al. [2010] which concerned a PIV experiment with similar setup. The Reynolds shear stress found, appears to be in good agreement with the current results. The maximum Reynolds shear stress in Bitter et al. [2010] occurs just slightly downstream of reattachment at $x/D = 1.2$ at a normalized value of -0.02. The current results reveal a maximum value of -0.03 which is also found near reattachment ($x/D = 1$). Overall the distribution of the Reynolds stress throughout the flow field show a strong resemblance.

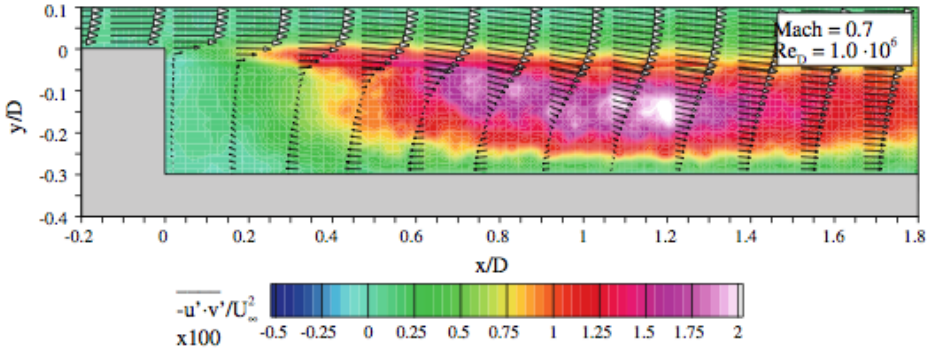

Figure 5.16: Reynolds shear stress as evaluated by Bitter et al. [2010].

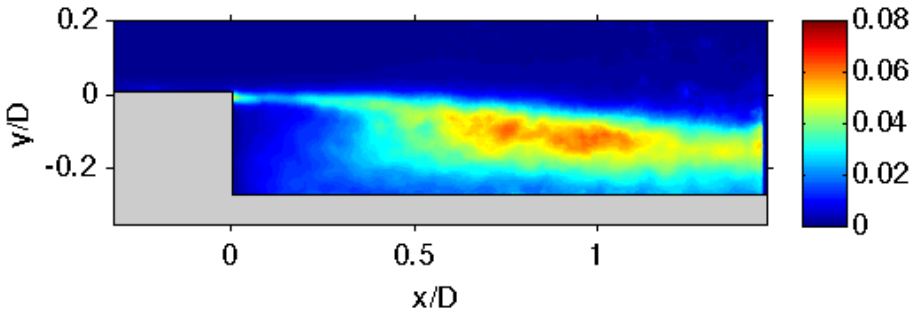

(a) $\frac{\overline{u'u'}}{V_\infty^2}$.

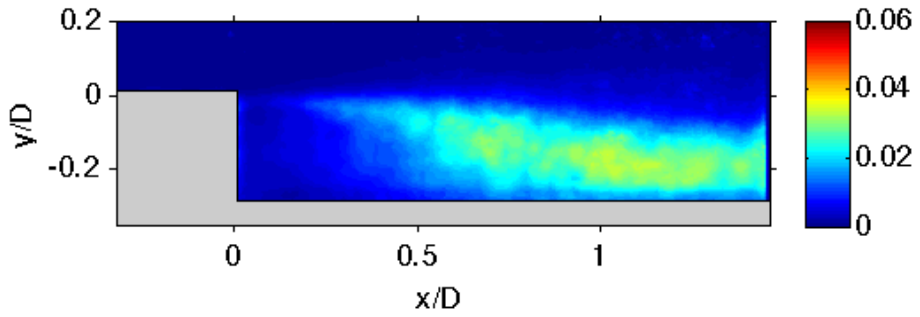

(b) $\frac{\overline{v'v'}}{V_\infty^2}$.

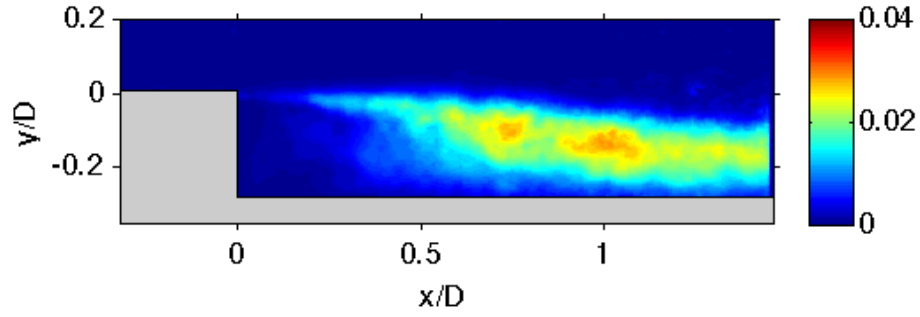

(c) $-\frac{\overline{u'v'}}{V_\infty^2}$.

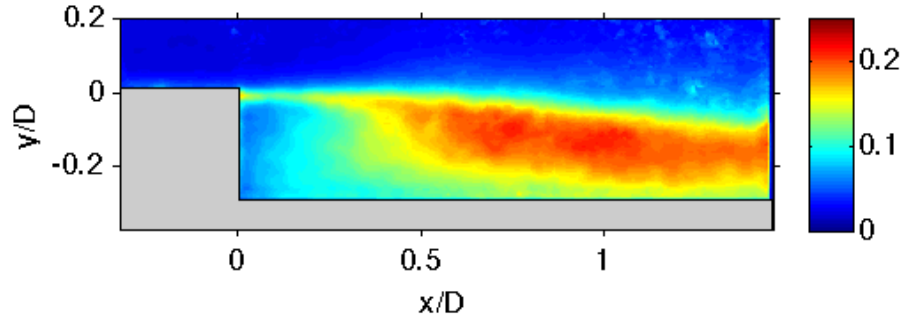

(d) $\frac{\sqrt{\frac{\overline{u'u'}+\overline{v'v'}}{2}}}{V_\infty}$.

Figure 5.17: Reynolds stresses for the long afterbody configuration.

Comparison

In order to make a more qualitative comparison between the tested configuration, profiles of the turbulence quantities are plotted in Figure 5.18. The profiles are plotted for the streamwise location $x/D = 0.5$ approximately halfway the recirculation bubble and $x/D = 1.0$ near the reattachment point. Looking at the turbulence intensity profiles at $x/D = 0.5$ in Figure 5.18g, it appears that the maximum turbulence levels are comparable in magnitude. The blunt base configuration shows a slightly higher maximum value. The most noticeable difference at $x/D = 0.5$ however lies in the shape of the profiles. From inspecting the profiles for the individual Reynolds stresses it can be seen that the afterbody configurations are quite similar with a well defined peak at the shear layer near $y/D = -0.05$ and a monotonous decrease towards the wall. The profiles corresponding to the blunt base configuration show a peak as well at the shear layer, but going inwards the turbulent fluctuations are clearly larger than for the afterbody configurations. The difference is especially visible for the transverse component shown in Figure 5.18c where the blunt configuration shows a much fuller profile. As discussed in the above this difference is attributed to the absence of an afterbody. The turbulent fluctuations and in particular those in y-direction can therefore grow larger since there is no solid body to obstruct this. In other words the flapping shear layer separated from a blunt base has more room in the wake to move up and down.

As we move further downstream to $x/D = 1.0$, the afterbody profiles remain similar. Apparently the hybrid reattachment (20% fluidic) does not have a substantial impact on the fluctuations with respect to complete solid reattachment. The earlier differences between the afterbody configurations and the blunt base configurations however have become more pronounced. This is because near the reattachment point, the influence of the wall is felt more. Not only does the blunt configuration show much fuller profiles but also the absolute levels of turbulent fluctuations are clearly larger. Hence it can be concluded that the presence of a solid afterbody has a weakening effect on the shear layer flapping.

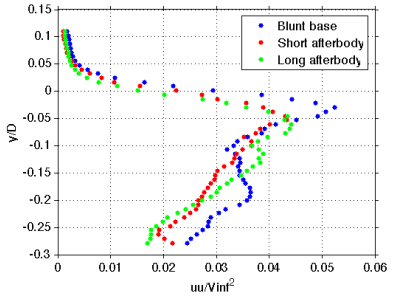

(a) $\frac{\overline{u'u'}}{V_\infty^2}$ at $x/D = 0.5$.

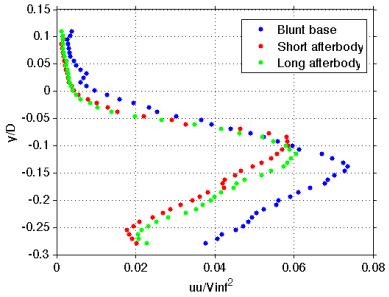

(b) $\frac{\overline{u'u'}}{V_\infty^2}$ at $x/D = 1.0$.

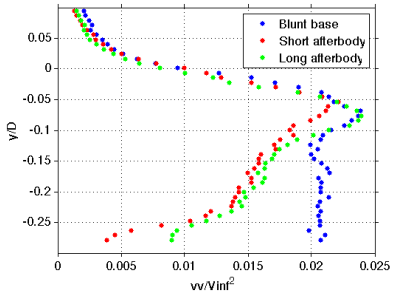

(c) $\frac{\overline{v'v'}}{V_\infty^2}$ at $x/D = 0.5$.

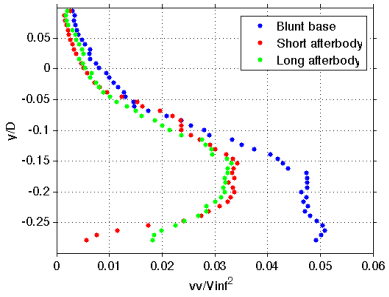

(d) $\frac{\overline{v'v'}}{V_\infty^2}$ at$x/D = 1.0$.

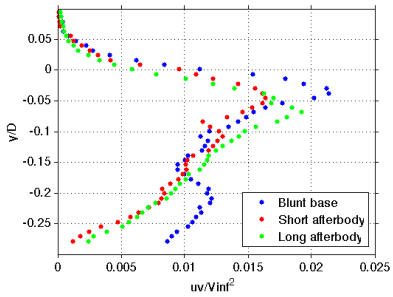

(e) $\frac{\overline{u'v'}}{V_\infty^2}$ at$x/D = 0.5$.

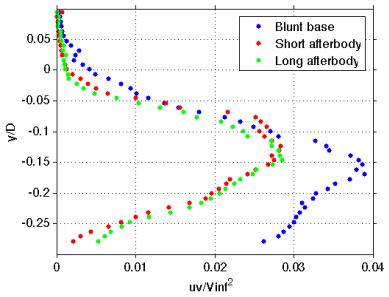

(f) $\frac{\overline{u'v'}}{V_\infty^2}$ at$x/D = 1.0$.

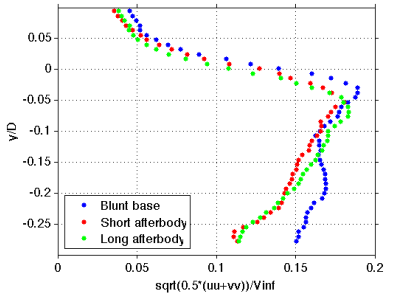

(g) Turbulence intensity at $x/D = 0.5$.

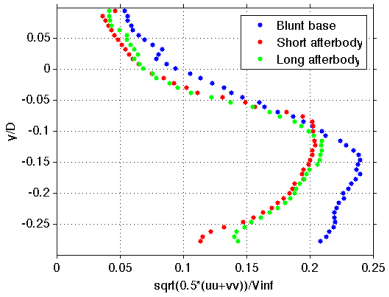

(h) Turbulence intensity at $x/D = 1.0$.

Figure 5.18: Comparison of turbulence profiles.

5.3 Boundary layer analysis

A boundary layer analysis is performed to assess the state of the boundary layer near separation before it evolves into the free flapping shear layer. Figure 5.19 gives an overview of how the boundary layer is developing in the region before it separates. A more in-depth analysis of the boundary layer profile is shown in Figure 5.20 and 5.21. Since the boundary layer profile did not show significant change within the inspected region $-0.7 \leq x/H \leq 0$ (H refers to step height), an averaged velocity profile of the whole region is used and is shown in 5.20. Using the definition of the boundary layer edge being where the velocity has reached 99% of the free stream, the boundary layer thickness can be estimated to be approximately $\delta_{99\%} \approx 4\text{mm}$ or $\delta_{99\%}/D \approx 0.08$.

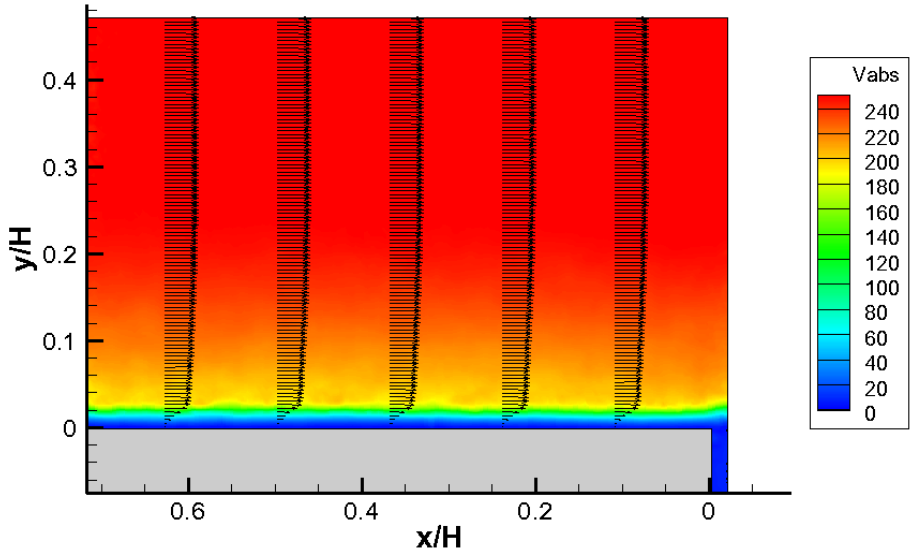

Figure 5.19: Boundary layer development near the point of separation.

The assumption is made that near the base of the model the boundary layer is turbulent, which is reinforced by the notion that a tripping wire is attached to the nose of the model to induce early transition. In order to confirm that the boundary layer is indeed turbulent, the velocity profile obtained from PIV is compared to the theoretically predicted profile which is done in Figure 5.21 by replotting the velocity profiles in terms of non-dimensionalized variables. It can be shown that when the spatial coordinate and velocity (e.g. y and u) are properly non-dimensionalized, the velocity profiles found in turbulent boundary layers can all be neatly described by a set of formulae. The variables y and u are non-dimensionalized as

$$y^+ = \frac{y\upsilon^*}{\nu}; \qquad u^+ = \frac{\overline{u}}{\upsilon^*} \tag{5-1}$$

where υ^* is called the *wall friction velocity* and is defined as

$$\upsilon^* = \sqrt{\frac{\tau_w}{\rho}} \tag{5-2}$$

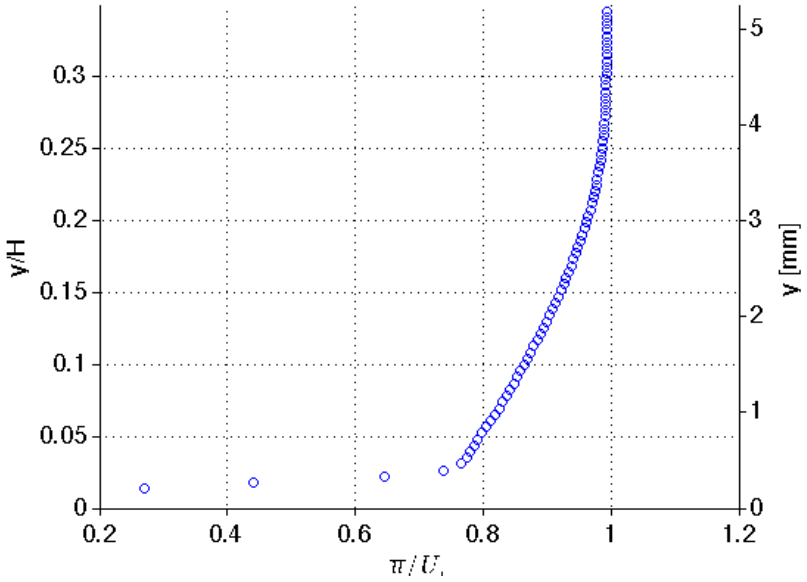

Figure 5.20: Velocity profile in the boundary layer ahead of separation.

The wall shear stress τ_w can normally be determined from

$$\tau_w = \mu \left(\frac{d\overline{u}}{dy} \right)_w ; \qquad \mu = \mu_0 \left(\frac{T}{T_0} \right)^{0.67} \tag{5-3}$$

However it is difficult to accurately determine the velocity close to the wall with the obtained PIV data. Hence the value obtained for the velocity gradient in equation (5-3) would be unreliable. Therefore an emprical formula is used to estimate the wall shear stress. The following power-law in correspondence to White [2006] is used:

$$C_f = 0.02 Re_\delta^{-\frac{1}{6}} \tag{5-4}$$

with the skin friction coefficient C_f related to τ_w as

$$C_f = \frac{\tau_w}{\frac{1}{2}\rho_\infty V_\infty} \tag{5-5}$$

As discussed in White [2006], the velocity profile of a turbulent boundary layer can be divided into an inner layer where viscous shear dominates, an outer layer where turbulent shear dominates and an intermediate overlapping region that smoothly connects the velocity profiles of the inner and outer layer.

The inner region of the velocity profile closest to the wall ($0 \leq y^+ \leq 5$) is called the *viscous sublayer*. This region can be described by the linear relation

$$u^+ = y^+ \tag{5-6}$$

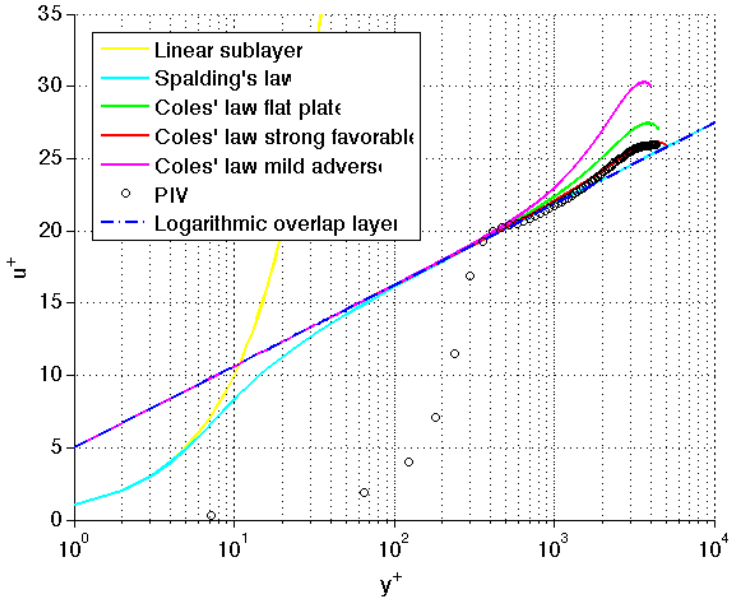

Figure 5.21: Boundary layer velocity profile plotted in terms of y^+ and u^+.

The *overlap layer* which corresponds to the region $35 \leq y^+ \leq 350$ can be described by a logarithmic relation as follows

$$u^+ = \frac{1}{\kappa} \ln y^+ + B \tag{5-7}$$

Where $\kappa = 4.1$ and $B = 5.0$ are empircally determined parameters as reported in White [2006]. The region between the viscous sublayer and the overlap layer (i.e. $5 \leq y^+ \leq 30$), which also falls within the inner region, is neither linear nor lograthmic but a smooth transition between the two and is called the *buffer layer*. A relation has been found that adequately describes this region as well and is termed *Spalding's Law of the Wall*:

$$y^+ = u^+ + e^{-\kappa B} \left(e^{\kappa u^+} - 1 - \kappa u^+ - \frac{(\kappa u^+)^2}{2} - \frac{(\kappa u^+)^3}{6} \right) \tag{5-8}$$

Finally the outer layer can be described by *Coles' Law of the wake*:

$$u^+ \approx \frac{1}{\kappa} \ln y^+ + B + \frac{2\Pi}{\kappa} f(\eta) \tag{5-9}$$

where

$$f(\eta) \approx \sin^2 \left(\frac{\pi}{2} \eta \right) \approx 3\eta^2 - 2\eta^3; \qquad \eta = \frac{y}{\delta} \tag{5-10}$$

The quantity Π is called Coles' wake parameter and for flat-plate flow corresponds to $\Pi \approx 0.5$. In case of a strong favorable pressure gradient $\Pi \approx 0.2$ and with a mild adverse pressure

gradient $\Pi \approx 11.5$ (as reported in White [2006]). Note that Coles' Law is also a valid approximation of the overlap region, in fact when $\Pi = 0$ the original log law of the overlap region is recovered.

The functions that describe the inner region (viscous sublayer and the buffer layer), the overlap region and the outer region are shown in 5.21 along with the obtained PIV data. It can be seen that only towards the end of the overlap region, the experimental data starts to fit the curves established from the empirical laws. The poor fitting data in Figure 5.21 runs up to $y^+ \approx 300$ which correponds to $y \approx 0.33mm$. For $y^+ > 300$ however the data fits Coles' Law for a boundary layer subject to a strong favorable pressure gradient (i.e. $\Pi = 0.2$) very well. The poor fit of the data in the inner region is attributed to inaccurate PIV data causing an underestimation of the velocity. The deterioration of accuracy near the surface is attributed to a combination of three things: movement of the model (< 5 pixels), reflections at the surface and insufficient spatial resolution.

Another way of investigating the nature of the boundary layer is by computing its shape factor H. The shape factor is a characteristic property of boundary layers defined as the ratio between the displacement thickness δ^* and momentum loss thickness θ (see equations (5-11)-(5-13)).

$$\delta^* = \int_0^\infty \left(1 - \frac{\overline{\rho}\,\overline{u}}{\rho_e U_e}\right) \mathrm{d}y \approx \int_0^\infty \left(1 - \frac{\overline{u}}{U_e}\right) \mathrm{d}y \tag{5-11}$$

$$\theta = \int_0^\infty \left(\frac{\overline{\rho}\,\overline{u}}{\rho_e U_e}\left(1 - \frac{\overline{u}}{U_e}\right)\right) \mathrm{d}y \approx \int_0^\infty \left(\frac{\overline{u}}{U_e}\left(1 - \frac{\overline{u}}{U_e}\right)\right) \mathrm{d}y \tag{5-12}$$

$$H = \frac{\delta^*}{\theta} \tag{5-13}$$

For laminar boundary layers the shape factor typically takes a value of $H \approx 2.59$ and for turbulent boundary layers $H \approx 1.5$. Typical velocity profiles of laminar and turbulent boundary layers are depicted in Figure 5.22. It can be seen that the turbulent profile is fuller than the laminar profile. This is because in turbulent boundary layers there is better mixing of the flow which causes more momentum to be exchanged from the outer region towards the wall. Furthermore, a 'fuller' velocity profile is connected to a lower shape factor.

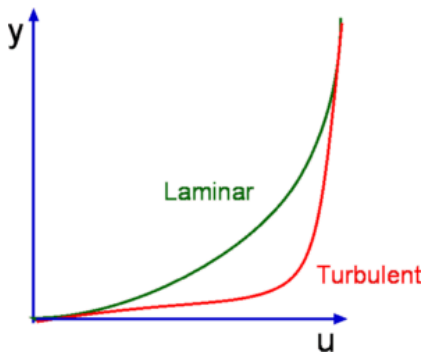

Figure 5.22: Typical velocity profiles for laminar and turbulent boundary layers *(Courtesy of http://www-mdp.eng.cam.ac.uk/)*

The shape factor in the present experiment is found to be $H = 1.7$ ($\delta^* = 0.69$mm, $\theta = 0.41$mm) which suggests a turbulent boundary layer rather than a laminar one. In addition it should be taken into account that the velocity near the wall is underestimated so that in reality the velocity profile is fuller which corresponds to a lower shape factor. In other words the obtained $H = 1.7$ is somewhat overestimating the actual shape factor which further proves that the boundary layer must be turbulent.

The computed shape factor in combination with the match of the PIV data with the outer region in Figure 5.21 is deemed sufficient to confirm that the boundary layer ahead of separation is indeed turbulent. Moreover the fit indicates that the boundary layer is subject to a favorable pressure gradient. This result could also be expected from inspection of the mean velocity fields, which show that at the base the flow expands and thereby accelerates.

5.4 Mixing-layer analysis

The turbulent boundary layer turns into a mixing layer after separation at the base of the model. Although the flow is axis symmetric, the separated shear layer is very similar to a planar mixing layer. The free shear layer plays an important role in the overall behavior of the recirculation area on the afterbody. The global dynamics of the bubble are influenced by the interaction between large vortical structures shed from the shear layer and the reattachment process on the afterbody. Considering the importance of the shear layer, it is therefore worth analyzing its development from the point of separation. Given the mean velocity data as obtained from the PIV experiment, it is possible to investigate the streamwise evolution of the shear layer. More specifically one can evaluate the growth of the shear layer thickness by inspecting the mean velocity profiles obtained from PIV. Formally speaking, the (plane) mixing layer is the turbulent flow that forms between to uniform and nearly parallel streams of different velocity e.g. U_1 and U_2.The edges of the shear layer can then be roughly defined as the point at which the mean velocity of the shear layer reaches a certain value. The shear layer thickness can thus be defined as (Pope [2000]):

$$\delta_{shear}(x) = y_{0.9}(x) - y_{0.1}(x) \tag{5-14}$$

where $y_{0.9}$ is the coordinate corresponding to one edge of the mixing layer where the following holds: $\overline{u} = U_1 + 0.9(U_2 - U_1)$ and $y_{0.1}$ on the other edge of the mixing layer, is the point where $\overline{u} = U_1 + 0.1(U_2 - U_1)$. This is also illustrated in Figure 5.23. In addition the position of the shear layer center $\overline{y}(x)$ can be defined by

$$\overline{y}(x) = \frac{1}{2}[y_{0.9}(x) + y_{0.1}(x)] \tag{5-15}$$

Alternatively one can investigate the streamwise development of the vorticity thickness which is also a characteristic thickness of the shear layer. The vorticity thickness allows for a more accurate estimate of the characteristic thickness than using the definition of δ_{shear} when either U_1 or U_2 is not effectively known. This is also the case with the configuration of the current experiment where the recirculation region under the free shear layer is not exactly a nearly parallel stream of uniform velocity. The vorticity thickness is defined as

$$\delta_\omega(x) = \frac{\overline{u}_{max}(x) - \overline{u}_{min}(x)}{\max\limits_y \left[\frac{\partial \overline{u}}{\partial y}(x,y)\right]} \tag{5-16}$$

where $\overline{u}_{max}(x) = \max\limits_y[\overline{u}(x,y)]$ and $\overline{u}_{min}(x) = \min\limits_y[\overline{u}(x,y)]$. This is illustrated in Figure 5.24.

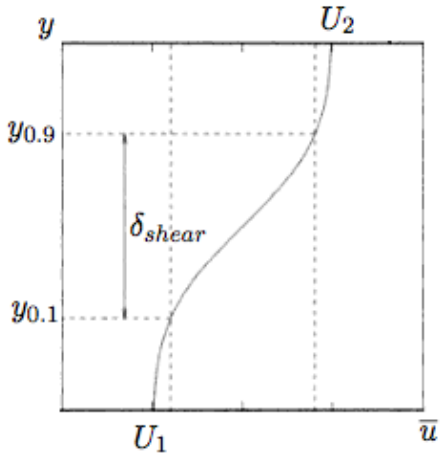

Figure 5.23: Definition of shear layer thickness.

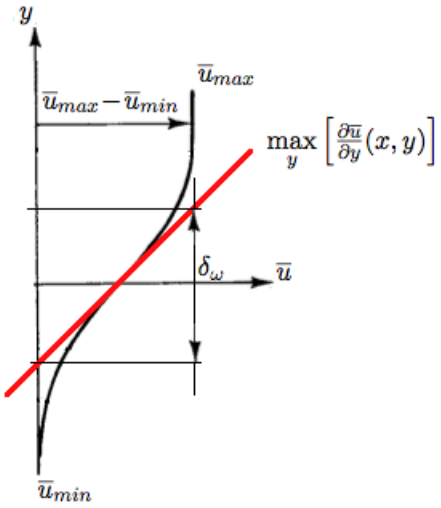

Figure 5.24: Definition of vorticity thickness.

Blunt base configuration

In Figure 5.25a velocity profiles of the separated shear layer are plotted. They correspond to the different streamwise positions x/D=0.1, x/D=0.3, x/D=0.5, x/D=0.7 and x/D=1.0. Note that the origin is chosen to coincide with the point of separation. It can be seen that

at x/D=0.1 when the shear layer has just separated, the thickness of the layer is still rather thin with a steep velocity gradient. At x/D=0.1 when the shear layer has just separated, the velocity profile exhibits a steep velocity gradient coupled with a small shear layer thickness. Between x/D=0.3 and x/D=1.0, the effects of mixing and momentum transport across the layer become clearly visible. The velocity gradient becomes less steep due to momentum transport and the thickness of the layer grows due to the entrainment process. The shear layer appears to move downwards until the reattachment point is reached. There is no afterbody and hence no wall to enforce a no slip condition. Therefore the velocity profiles do not go to zero until they near the reattachment point (y/D=1.2), which is in agreement with the notion that the reattachment point is analogous to a stagnation point. Also notice that as expected the backflow velocity near the centerline of the model is highest near x/D=0.5, since this corresponds to the point halfway of the recirculation bubble where the strongest backflow occurs.

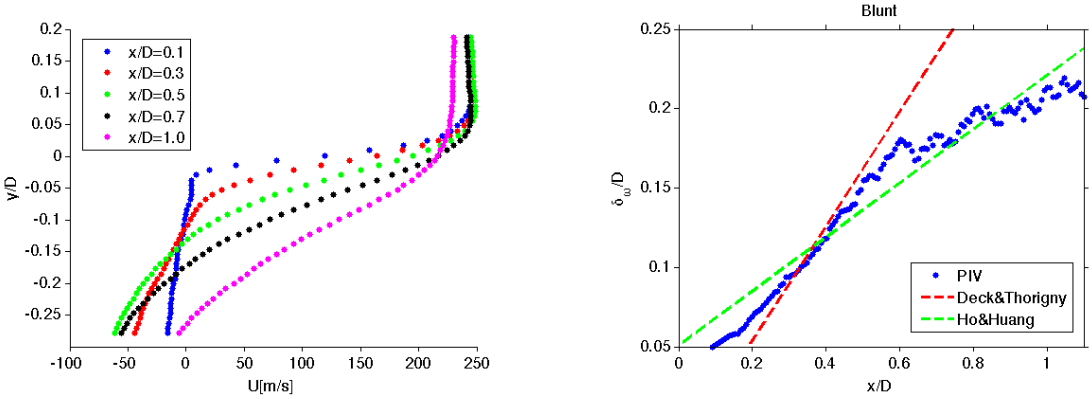

(a) Velocity profiles at different streamwise locations.

(b) Streamwise development of the vorticity thickness.

Figure 5.25: Streamwise development of the shear layer for the blunt configuration.

On the other hand the shear layer development can be viewed in terms of vorticity thickness as is done in Figure 5.25b. It shows the streamwise development of the vorticity thickness for the blunt configuration. From literature it is known that the planar free mixing-layer exhibits a linear growth rate. This is found to be $\frac{d\delta_\omega}{dx} \approx 0.17$ as reported by Ho and Huang [1982]. In a recent study on afterbody flow by Deck and Thorigny [2007] however, the separated shear layer showed a growth rate of $\frac{d\delta_\omega}{dx} \approx 0.36$ in the region up to $x/D = 0.6$ where it was considered outside the influence of the wall. For comparison these linear growth rates are shown in Figure 5.25b as well. The current results are in better agreement with the findings of Deck and Thorigny [2007]. It thus seems that the free shear layer in afterbody flows has a larger growth rate compared to the classic planar mixing layer. This difference might be caused by the expansion of the flow after separation of the shear layer. Also as suggested by Deck and Thorigny [2007], in case of afterbody flow the low speed side of the flow is highly turbulent due to recirculation. This in turn leads to the reingestion of turbulent structures in the separated shear layer which enhances its growth.

Afterbody configurations

In Figure 5.26a velocity profiles are shown for the streamwise locations corresponding to x/D=0.1, x/D=0.3, x/D=0.5, x/D=0.7 and x/D=1.0. Overall the shear layer behaves quite similar to the blunt base case, starting off with a steep velocity gradient that gradually evens out as the entrainment process continues. In Figure 5.26b the streamwise development of the vorticity thickness as determined from the PIV data is shown together with results from a CFD simulation performed by Deck and Thorigny [2007]. The vorticity thickness displays a steady increase from the point of separation to $x/D \approx 0.6$ after which it reaches a plateau. The overall trend of δ_ω agrees with the results by Deck and Thorigny [2007] except for the maximum vorticity thickness reached in the current results is slightly lower. The main difference with the blunt base configuration is that the maximum vorticity thickness seems to be reached earlier and at a lower value than when reattachment is purely fluidic. The vorticity thickness is seen to grow mostly in the region up to halfway the recirculation bubble. At $x/D \approx 0.6$ the vorticity thickness reaches a plateau set at $\frac{\delta_\omega}{D} \approx 0.18$. In case of fluidic reattachment (see Figure 5.25b) the vorticity thickness keeps increasing and reaches up to $\frac{\delta_\omega}{D} \approx 0.21$. A reason for this could be that in the blunt configuration there is no solid afterbody present that inhibits the shear layer growth. Finally in Figure 5.27 the results of the case with solid reattachment are presented. The velocity profiles for both the afterbody configurations are almost identical. Also the maximum vorticity thickness observed is the same. A noticable difference however is that with solid reattachment the reaching of the plateau value is somewhat more gradual.

Finally Figure 5.28 shows the results from a CFD study by Deck and Thorigny [2007] which concerned a short afterbody configuration ($L/D = 1.2$) with an exhaust jet.

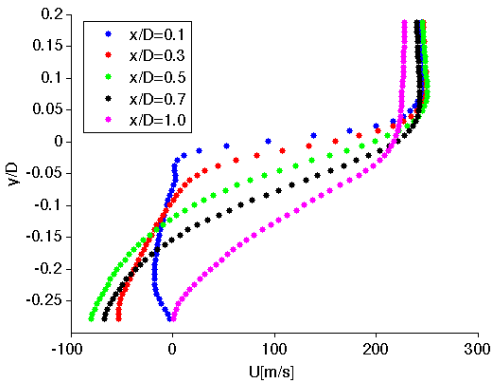

(a) Velocity profiles at different streamwise locations.

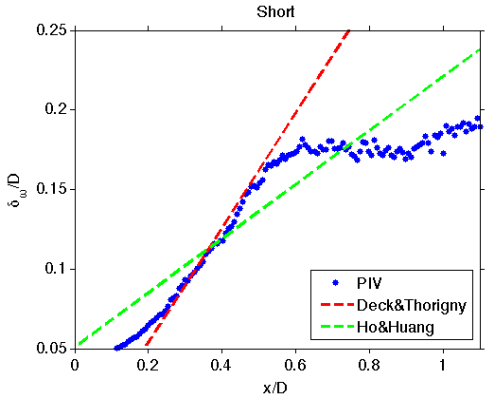

(b) Streamwise development of the vorticity thickness.

Figure 5.26: Streamwise development of the shear layer for the short afterbody configuration.

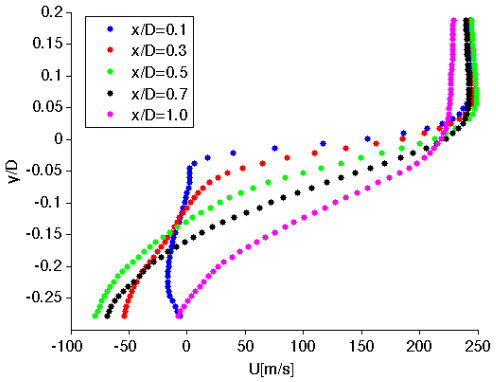

(a) Velocity profiles at different streamwise locations.

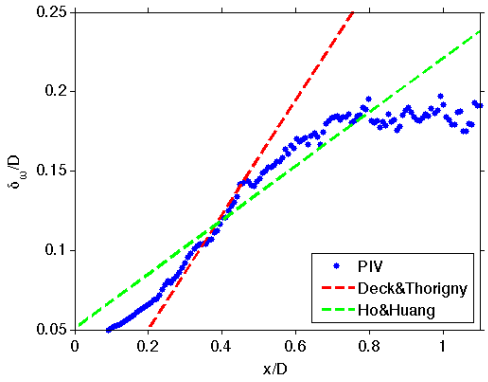

(b) Streamwise development of the vorticity thickness.

Figure 5.27: Streamwise development of the shear layer for the long afterbody configuration.

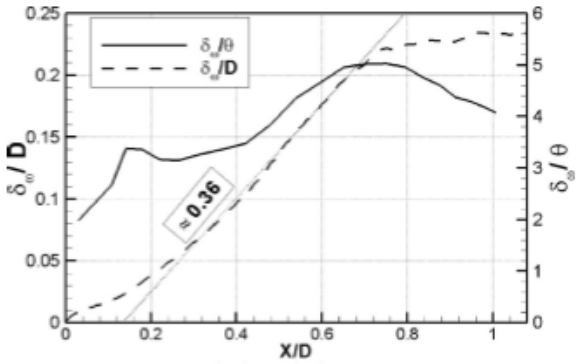

Figure 5.28: Vorticity thickness growth rates from Deck and Thorigny [2007].

Comparison

The mixing-layer growth in the three tested configurations are compared in Figure 5.29. Up to $x/D = 0.5$ the profiles appear almost identical. This indicates that the influence of the afterbody on the growth rate is still negligible. Between $x/D = 0.5$ and $x/D = 0.7$ the blunt base and short afterbody configuration show the same development. On the other hand the long afterbody shows a slightly lower rate of growth than the blunt configuration but more importantly also lower than the short afterbody. This might indicate that hybrid reattachment in the short afterbody configuration has some influence on the shear layer thickness even though the effect on the overall turbulence levels is limited as discussed in the previous section. However at this point it cannot be said with certainty whether this measured difference in shear layer growth is indeed an actual physical phenomenon or that it is caused by a suboptimal spatial resolution of the PIV data in the shear layer center. From $x/D = 0.7$ onward the small difference observed between the afterbody configurations remains inconclusive as to whether we are observing a physical difference between the shear layer development in both afterbody configurations. They both seem to reach a plateau around δ_ω/D=0.18. The blunt configuration clearly continues increasing and reaches a value

of δ_ω/D=0.21. The larger vorticity thickness for the blunt base configuration can once again be attributed to the absence of an afterbody that would restrict the space in which the shear layer can grow.

When we compare the result by Deck and Thorigny [2007] with the current experiment we see a similar trend in the shear layer development but a difference in the plateau values reached near the reattachment region. Deck and Thorigny [2007] found a value of δ_ω/D=0.23, whereas the current results shows a value of δ_ω/D=0.18. This difference can be ascribed to a difference in the initial boundary layer thickness right before separation. In Deck and Thorigny [2007] the boundary layer ahead of separation had a boundary layer thickness of $\delta/D = 0.2$, while in the current experiment $\delta/D = 0.08$. Consequently the thicker starting boundary layer thickness in Deck and Thorigny [2007] explains why the final plateau value reached is also higher.

In the region up to $x/D \approx 0.5$ the current results show a larger vorticity thickness than was found by Deck and Thorigny [2007]. At first sight this seems to contradict the notion that the current experiment features a much thinner separating boundary layer. However since the boundary layer is already known to be thinner (established by the PIV measurements), the discrepancy cannot be caused by the actual thickness of the boundary layer. Another potential cause to be considered is the spatial resolution. Insufficient spatial resolution typically leads to an underestimation of the slope (in the center) of a shear layer's velocity profile. By inspecting equation (5-16) it becomes clear that underestimating the slope i.e. $\frac{\partial \overline{u}}{\partial y}$ consequently leads to an overestimation of the vorticity thickness as was observed Figure 5.29. In the current experiment the boundary layer thickness is 4mm and an interrogation window size of 1.6x1.6mm^2 is used. In other words the height of the interrogation window covers 40% of the boundary layer thickness.

Moreover Figure 5.30 shows the recommended amount of data points in the mixing layer's vorticity thickness for accurate CFD modeling as reported in (Weiss et al. [2009]). It is suggested that near separation approximately 20 data points are required. This number increases going in downstream direction up to almost 60 in the region of reattachment of the mixing layer. Subsequently inspecting the velocity profiles in Figure 5.26a and 5.27a and counting data points reveals that in the current experiment near separation the mixing layer thickness is described by approximately 12 data points which goes up to about 40 data points near reattachment. Thus in addition to a relatively large interrogation window size compared to the shear layer also the number of data points available appears to be less than advised. Hence it can be concluded that it is most likely an inadequate spatial resolution that causes an overestimation of the vorticity thickness of the shear layer in the region right after separation.

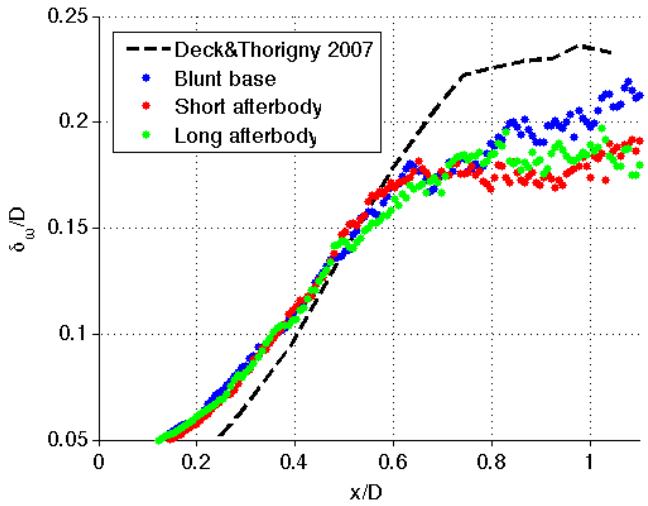

Figure 5.29: Comparison between the vorticity thickness growth rates.

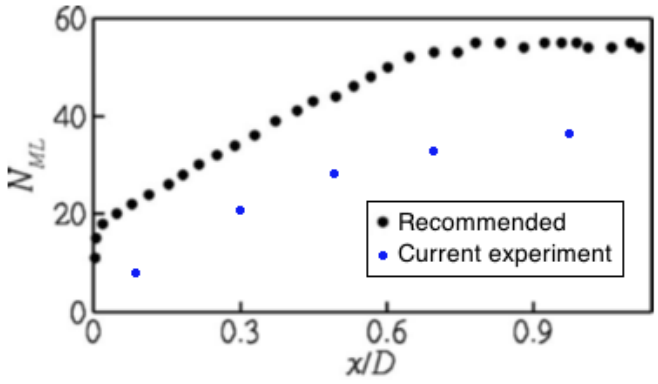

Figure 5.30: Recommended number of data points in the mixing layer's vorticity thickness (Weiss et al. [2009]).

Chapter 6

Pressure evaluation

The PIV data discussed in the previous chapter can be used to compute the pressure field. In this approach the computation of the pressure resembles a CFD procedure. The main difference however is that the velocity data is obtained experimentally (PIV) rather than being computed numerically from the relevant fluid dynamic equations.

Traditional CFD methods require a number of fundamental equations to form a closed system from which the unknown variables in the flow field can be computed. In compressible flow the required equations are the continuity equation, Navier-Stokes (momentum) equations and the energy equation along with the necessary thermodynamic state relations. This generally results in five independent equations for the five unknowns density ρ, pressure p, velocity $\mathbf{V}$, internal energy e and temperature T, see Anderson [2007]. When analyzing turbulent flow however, one can make use of the so called Reynolds-averaged formulation, which expresses the equations above in terms of time-averaged and fluctuating components of the flow variables. This introduces additional terms in the momentum equations also known as the Reynolds stresses that are coupled to the fluctuating velocity components in the flow (discussed in Pope [2000]).

On the other hand when PIV data is available, the velocity flow variable (whether in absolute or Reynolds-averaged formulation) can be eliminated as an unknown which greatly simplifies the system of equations. The main flow variable that is of interest in the current project is the pressure which can be obtained in a number of ways. This chapter starts with an elaboration on the particular approach used to obtain the pressure field near the base of the model from PIV data. Then the results are presented and analyzed. The chapter concludes with a discussion on the accuracy of the results.

6.1 Governing equations

As mentioned in the introduction of this chapter, pressure is the flow variable to be determined from the governing flow equations. As a first step, the Navier-Stokes equations are considered since they contain a pressure term. More specifically because the flow under investigation is

turbulent, the Reynolds-averaged Navier-Stokes (RANS) equations (6-1) are used. Viscosity is assumed negligible due to the high Reynolds number of the flow. Hence the viscous terms in the RANS equations are left out. Note that the Eulerian acceleration of the mean velocity has been left out, because the flow is assumed to be statistically stationary i.e. statistics depend on spatial coordinates only and are independent of time. From the momentum equation all the velocity variables are essentially known, since they are measured by PIV. This leaves a pressure term and the density. The wind tunnel experiments are carried out at $M = 0.7$, hence the flow is considered compressible. Therefore the momentum equation alone is not sufficient to solve for the two unknowns pressure and density. In accordance to Van Oudheusden [2008] the ideal gas law, equation (6-2) is introduced to replace density with pressure and temperature. The adiabatic flow assumption, equation (6-3) then allows to express temperature in terms of velocity magnitude which again is provided from PIV data.

$$\frac{\partial p}{\partial x_j} = -\left(\rho U_j \frac{\partial U_i}{\partial x_j} + \frac{\partial \rho \overline{u_i' u_j'}}{\partial x_j}\right) \tag{6-1}$$

$$\rho = \frac{p}{RT} \tag{6-2}$$

$$\frac{T}{T_\infty} = 1 + \frac{\gamma - 1}{2} M_\infty^2 \left(1 - \frac{V^2}{V_\infty^2}\right) \tag{6-3}$$

The RANS equations together with the ideal gas law and adiabatic flow assumption thus form a closed system from which p can be determined. The actual form of the implemented RANS equation corresponds to the non-conservative formulation given in Van Oudheusden [2008] where density has been replaced using the gas law.

$$\left(\delta_{ij} + \frac{\overline{u_i' u_j'}}{RT}\right) \frac{\partial \ln(p/p_\infty)}{\partial x_j} = -\frac{1}{RT}\left(U_j \frac{\partial U_i}{\partial x_j} + \frac{\overline{\partial u_i' u_j'}}{\partial x_j} - \frac{\overline{u_i' u_j'}}{T}\frac{\partial T}{\partial x_j}\right) \tag{6-4}$$

Note that the pressure term has been recast according to

$$\frac{1}{p}\frac{\partial p}{\partial x_i} = \frac{\partial \ln(p/p_\infty)}{\partial x_i} \tag{6-5}$$

This is done for reasons that will become clear in the next section. Furthermore it has been assumed that the effect of density fluctuations is negligible as well as the viscous stresses.

6.2 Poisson formulation for the pressure

In the previous section an expression was obtained where pressure is the only unknown since the other variables are known available from PIV measuremens. The pressure term $\frac{\partial \ln(p/p_\infty)}{\partial x_j}$ can be solved by employing a spatial integration scheme. However for the current project it is chosen to solve for the pressure by means of a 2-D Poisson formulation:

$$\nabla^2 \ln(p/p_\infty) = \frac{\partial^2 \ln(p/p_\infty)}{\partial x^2} + \frac{\partial^2 \ln(p/p_\infty)}{\partial y^2} = F(x, y) \tag{6-6}$$

This is done because the Poisson formulation is a more robust method, in particular when the accuracy of the boundary conditions may vary. Consider again equation (6-4) presented in

the previous section. For clarity the left hand side of this equation is expanded and presented below.

$$\frac{\partial \ln(p/p_\infty)}{\partial x} + \frac{\overline{u'u'}}{RT}\frac{\partial \ln(p/p_\infty)}{\partial x} + \frac{\overline{u'v'}}{RT}\frac{\partial \ln(p/p_\infty)}{\partial y} + \frac{\overline{u'w'}}{RT}\cancel{\frac{\partial \ln(p/p_\infty)}{\partial z}} = f_x \tag{6-7}$$

$$\frac{\partial \ln(p/p_\infty)}{\partial y} + \frac{\overline{u'v'}}{RT}\frac{\partial \ln(p/p_\infty)}{\partial x} + \frac{\overline{v'v'}}{RT}\frac{\partial \ln(p/p_\infty)}{\partial y} + \frac{\overline{v'w'}}{RT}\cancel{\frac{\partial \ln(p/p_\infty)}{\partial z}} = f_y \tag{6-8}$$

$$\cancel{\frac{\partial \ln(p/p_\infty)}{\partial z}} + \frac{\overline{u'w'}}{RT}\frac{\partial \ln(p/p_\infty)}{\partial x} + \frac{\overline{v'w'}}{RT}\frac{\partial \ln(p/p_\infty)}{\partial y} + \frac{\overline{w'w'}}{RT}\cancel{\frac{\partial \ln(p/p_\infty)}{\partial z}} = f_z \tag{6-9}$$

The flow is assumed to be axisymmetric. The validity of this assumption is shown in Chapter 5. It also implies that any plane aligned with the x-axis can be considered a plane of symmetry. Since in an axisymmetric flow, resolving the symmetry plane is essentially sufficient to describe the complete wake, the analysis can be greatly simplified. By only resolving the symmetry plane we can reduce the analysis of the 3-D flow field to a 2-D problem. In the current experiment the measurement takes place in the symmetry plane aligned with the x and y axes. Therefore if we apply the Poisson formulation in this plane all terms that contain a derivative in z direction can be ignored as shown in the above equations. This conveniently leaves just two unknowns $\frac{\partial \ln(p/p_\infty)}{\partial x}$ and $\frac{\partial \ln(p/p_\infty)}{\partial y}$ which can be solved with equations (6-7) and (6-8). Writing the system of linear equations as a matrix product, the individual pressure terms can easily be computed using matrix inversion.

$$[\mathbf{A}]\,[\mathbf{dp}] = [\mathbf{f}] \quad \Rightarrow \quad [\mathbf{dp}] = [\mathbf{A}]^{-1}\,[\mathbf{f}] \tag{6-10}$$

$$[\mathbf{dp}] = \begin{bmatrix} \frac{\partial \ln(p/p_\infty)}{\partial x} \\ \frac{\partial \ln(p/p_\infty)}{\partial y} \\ \frac{\partial \ln(p/p_\infty)}{\partial z} \end{bmatrix} \tag{6-11}$$

$$[\mathbf{A}] = \begin{bmatrix} 1+\frac{\overline{u'u'}}{RT} & \frac{\overline{u'v'}}{RT} & \frac{\overline{u'w'}}{RT} \\ \frac{\overline{u'v'}}{RT} & 1+\frac{\overline{v'v'}}{RT} & \frac{\overline{v'w'}}{RT} \\ \frac{\overline{u'w'}}{RT} & \frac{\overline{v'w'}}{RT} & 1+\frac{\overline{w'w'}}{RT} \end{bmatrix} \tag{6-12}$$

The matrix $\mathbf{A}$ and vector $\mathbf{dp}$ are shown here in their general form applicable to a general 3-D flow. Note that for the current case of axisymmetric flow only the flow in the x, y-plane is considered. Hence $\mathbf{dp}$ and $\mathbf{f}$ only consist of their first two entries and $\mathbf{A}$ consists of the first two rows and columns. The expanded right hand side of equations (6-7), (6-8) and (6-7) are shown below. As before the terms with a derivative with respect to z are omitted based on the assumption of axisymmetric flow.

$$\begin{aligned} f_x = -\frac{1}{RT}\Bigg(& U\frac{\partial U}{\partial x} + V\frac{\partial U}{\partial y} + \cancel{W\frac{\partial U}{\partial z}} \\ & + \frac{\partial \overline{u'u'}}{\partial x} + \frac{\partial \overline{u'v'}}{\partial y} + \cancel{\frac{\partial \overline{u'w'}}{\partial z}} - \frac{\overline{u'u'}}{T}\frac{\partial T}{\partial x} - \frac{\overline{u'v'}}{T}\frac{\partial T}{\partial y} - \cancel{\frac{\overline{u'w'}}{T}\frac{\partial T}{\partial z}}\Bigg) \end{aligned} \tag{6-13}$$

$$\begin{aligned} f_y = -\frac{1}{RT}\Bigg(& U\frac{\partial V}{\partial x} + V\frac{\partial V}{\partial y} + \cancel{W\frac{\partial V}{\partial z}} \\ & + \frac{\partial \overline{u'v'}}{\partial x} + \frac{\partial \overline{v'v'}}{\partial y} + \cancel{\frac{\partial \overline{v'w'}}{\partial z}} - \frac{\overline{u'v'}}{T}\frac{\partial T}{\partial x} - \frac{\overline{v'v'}}{T}\frac{\partial T}{\partial y} - \cancel{\frac{\overline{v'w'}}{T}\frac{\partial T}{\partial z}}\Bigg) \end{aligned} \tag{6-14}$$

$$f_z = -\frac{1}{RT}\left(U\frac{\partial W}{\partial x} + V\frac{\partial W}{\partial y} + \cancel{W\frac{\partial W}{\partial z}} + \frac{\partial \overline{u'w'}}{\partial x} + \frac{\partial \overline{v'w'}}{\partial y} + \cancel{\frac{\partial \overline{w'w'}}{\partial z}} - \frac{\overline{u'w'}}{T}\frac{\partial T}{\partial x} - \frac{\overline{v'w'}}{T}\frac{\partial T}{\partial y} - \cancel{\frac{\overline{w'w'}}{T}\frac{\partial T}{\partial z}}\right) \tag{6-15}$$

The final step in preparing the 2-D Poisson formulation for the x-y plane, is to take the divergence of the result in equation (6-10) (considering only x and y components). By doing this we in effect obtain $F(x, y)$ as given on the right hand side in equation (6-6) whereas the left hand side is prepared with a finite difference scheme in terms of $\ln(p/p_\infty)$ taking into account boundary conditions.

The steps outlined in the above are carried out for every point on a $n \times m$ grid, which results in

$$\nabla^2 \ln(p/p_\infty) \quad \equiv \quad [\mathbf{M}] \begin{bmatrix} \ln(p/p_\infty)_1 \\ \vdots \\ \ln(p/p_\infty)_{n\times m} \end{bmatrix} = \begin{bmatrix} F_1 \\ \vdots \\ F_{n\times m} \end{bmatrix} \tag{6-16}$$

which is a system of linear equations that is the discrete counterpart of (6-6) i.e. it is the discrete poisson equation which can be solved numerically to obtain the pressure field. The exact form of matrix $\mathbf{M}$ depends on the shape of the computational domain and the type of boundary conditions used. The right hand side vector $\mathbf{F}$ in equation (6-16), corresponds to

$$[\mathbf{F}] = \nabla \cdot [\mathbf{A}]^{-1} [\mathbf{f}] \tag{6-17}$$

where $[\mathbf{A}]^{-1} [\mathbf{f}]$ was obtained previously in equation (6-10).

6.3 Poisson solver

The Poisson solver is based on the one originally developed and used in Ragni et al. [2012] and it solves equation (6-16) for the pressure terms. To run the solver though, appropriate boundary conditions need to be specified. These can be either of the Dirichlet type which specifies the pressure on the boundary directly or of the Neumann type, by which the first order derivative of pressure with respect to the appropriate spatial coordinate is given. Note that the Poisson formulation is given in terms of $\ln(p/p_\infty)$ as shown in equation (6-16). Therefore the Poisson solver computes $\ln(p/p_\infty)$ and not p directly. So accordingly the Dirichlet boundary condition specifies $\ln(p/p_\infty)$ while Neumann conditions would be given as $\frac{\partial \ln(p/p_\infty)}{dx}$ on vertical boundaries and as $\frac{\partial \ln(p/p_\infty)}{dy}$ on horizontal boundaries. Figure 6.1 illustrates the computational domains for the tested configurations (blunt and afterbody) and the type of boundary conditions applied on the edges. The Dirichlet boundary condition is represented by the color blue and is applied on the top boundary. Dirichlet is applied there because there the flow can be assumed isentropic. Consequently from the isentropic flow relation given in equation (6-18) values for the pressure can be computed directly.

$$\frac{p}{p_\infty} = \left(\frac{\rho}{\rho_\infty}\right)^\gamma = \left(\frac{T}{T_\infty}\right)^{\frac{\gamma}{\gamma-1}} = \left(1 + \frac{\gamma-1}{2} M_\infty^2 \left(1 - \frac{V^2}{V_\infty^2}\right)\right)^{\frac{\gamma}{\gamma-1}} \tag{6-18}$$

In flow regions where the isentropic flow assumption does not hold, such as in the wake or the boundary layer, Neumann conditions are applied which are shown as red lines in Figure

6.1. The value of the Neumann boundary condition i.e. the spatial derivative of the pressure is readily available since it has been computed during the step outlined by equation (6-10) where the velocity terms are provided by the PIV experiment.

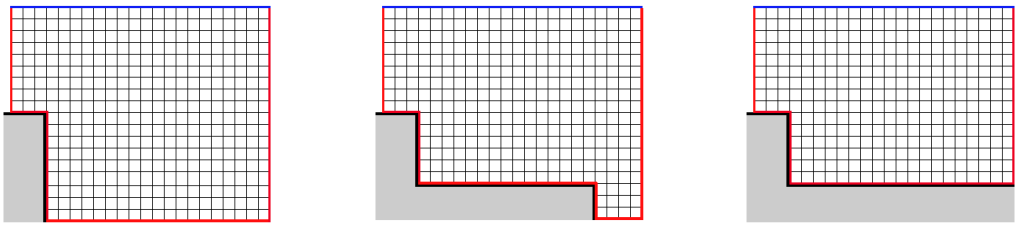

(a) Boundary conditions used for the blunt based configuration.

(b) Boundary conditions used for the short afterbody configuration.

(c) Boundary conditions used for the long afterbody configuration.

Figure 6.1: Boundary conditions specified in the Poisson solver. (Red): Dirichlet, (Blue): Neumann.

6.4 Mean pressure fields

Blunt configuration

The mean pressure field is computed with the Poisson solver using the obtained PIV data for the afterbody configuration. The result is shown in Figure 6.2. Note that the mask used is slightly larger than the model body (the origin in the figure is the actual edge of the model base). The reason for this is that the velocity at the model surface is not resolved accurately enough due to local reflections off the model surface. This affects the quality of the boundary conditions which would in turn decrease the accuracy of the computed pressure field.

The pressure distribution across the base in radial direction is shown in Figure 6.3. The values appear in reasonably good agreement with Deprés et al. [2004], showing a similar trend of decreasing pressure in radial direction. Overall the C_p values seem slighty lower however. Possible causes for this will be discussed in the next section where the afterbody configurations are covered. The result in Figure 6.4a is obtained by solving the complete domain using the Poisson solver. This includes the inviscid flow region away from the model that in theory can be assumed to be isentropic. This implies that if the Poisson solver performs correctly, the results in the isentropic flow region should correspond to the pressure as predicted from the isentropic flow theory. The pressure field predicted by applying the isentropic flow relations is shown in Figure 6.4b. The pressure obtained in the non-isentropic region i.e. the turbulent wake of the model is of course not valid and is therefore blanked. The pressure field obtained by the Poisson solver and the one predicted from isentropic flow theory appear to agree very well and the difference in C_p is found to be on the order of 1%. This confirms the validity and the ability of the Poisson solver to accurately resolve the pressure in isentropic flow.

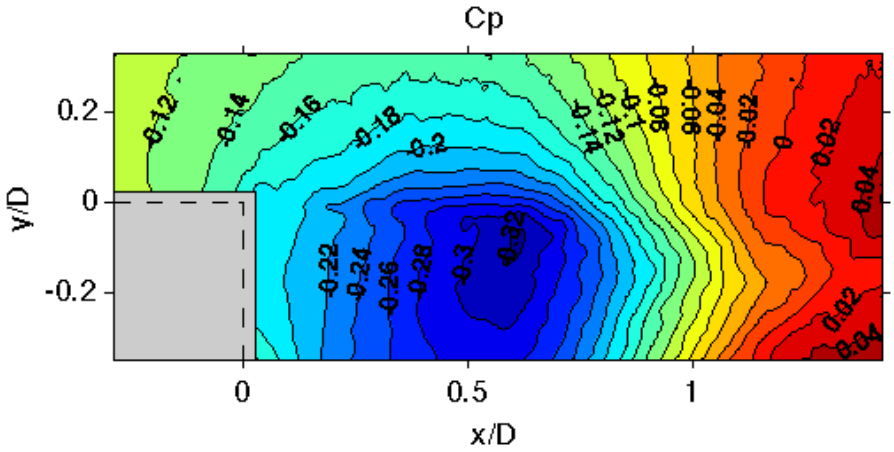

Figure 6.2: C_p contours for the blunt base configuration.

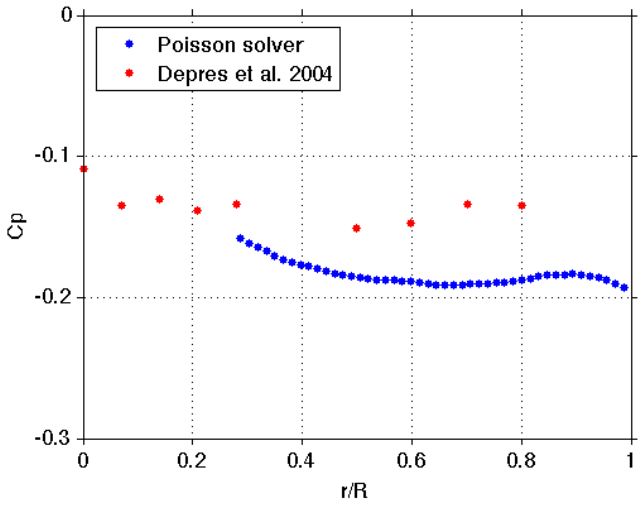

Figure 6.3: C_p distribution across the surface of the blunt base in radial direction.

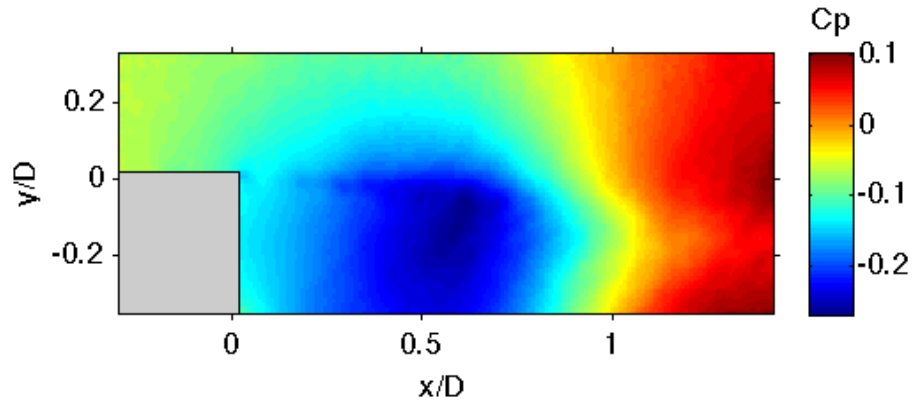

(a) C_p computed with Poisson solver.

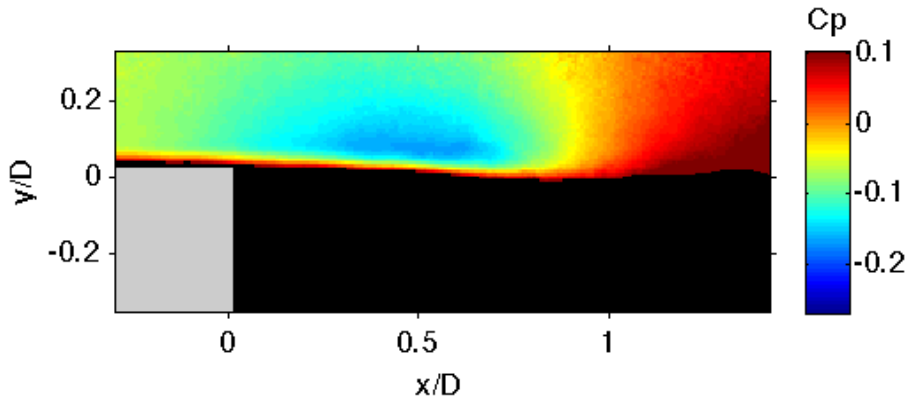

(b) C_p resulting from isentropic flow assumption.

Figure 6.4: Computed pressure fields for the blunt base configuration.

Afterbody configurations

The CFD results reported in Deck and Thorigny [2007] and Weiss et al. [2009] are well suited for comparison with the pressure obtained by the Poisson solver in the turbulent wake. Their results are based on a cylindrical afterbody flow simulation with the afterbody extending up to $L/D = 1.2$, see Figure 2.8. In Deck and Thorigny [2007] the afterbody featured an ideally expanded exhaust jet at the end of the afterbody, while in the study performed by Weiss et al. [2009] this jet was absent as can be seen in Figure 2.8. The free stream Mach number was set at $M_\infty = 0.702$ and Reynolds number based on the base diameter was $Re_D = 1.1 \cdot 10^6$. Furthermore the model they used had a ratio between afterbody diameter and base diameter of $D_{ratio} = 0.4$ which is the same for the model used during the current experiments.

Presented in Figure 6.5 (top) is the pressure field obtained from the current experiment for the short afterbody configuration. The lower half of the figure features the results obtained by Weiss et al. [2009]. Overall the contour lines appear to be in good agreement. Downstream of the base a low pressure region develops. The minimum pressure is reached in the center of the recirculation bubble at $x/D = 0.5$ after which recompression of the flow begins. It is also noticed that the effective stagnation point located at $x/D \approx 1$ is not where the maximum pressure is reached because the recompression process continues beyond the mean reattachment point at least up to $x/D = 1.4$.

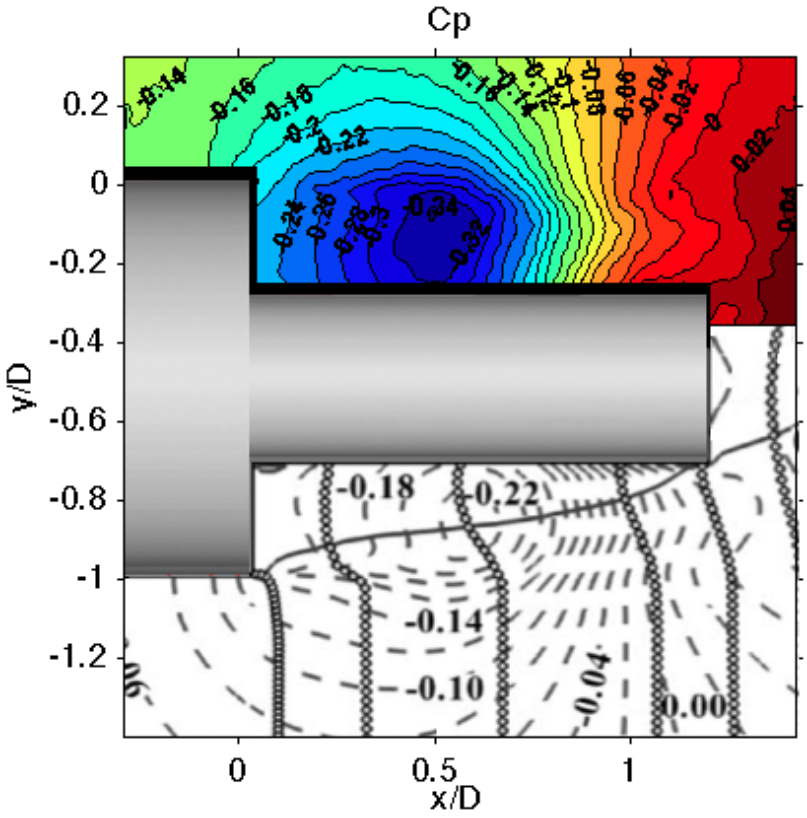

Figure 6.5: (top): C_p contours by Poisson solver, black edge on model is outline of mask. (bottom) CFD results from Weiss et al. [2009].

Despite the general agreement of the contour lines there are also some noticeable differences to be seen. The first difference can be found in the region of the developing shear layer ($0 \leq x/D \leq 0.5$). In the lower half of Figure 6.5 it can be seen that the pressure contours follow the course of the shear layer after separation. The contour lines show a clear horizontal orientation as they are aligned with the shear layer which acts as an interface between the free stream and the separated low pressure region. These features are less pronounced in the upper half of Figure 6.5. This is attributed to insufficient spatial resolution to fully capture the developing shear layer. Another difference is found at the afterbody surface. The contour lines in Weiss et al. [2009] clearly show that near the afterbody there are moderate pressure gradients normal to the surface. In the solution obtained from the current experiment however the orientation of the contour lines barely show any pressure gradient normal to the surface. The difference in orientation of the contour lines near the surface is mainly caused by the mask used in the current experiment. Due to reflections at the surface, the mask has to cover more than the outlines of the model. Hence the pressure is not resolved up to the actual model surface but slightly above it. This notion is confirmed when noticing that in Weiss et al. [2009] that slightly away from the surface, the pressure contours indeed become more vertical indicating a decrease in pressure gradient normal to the surface.

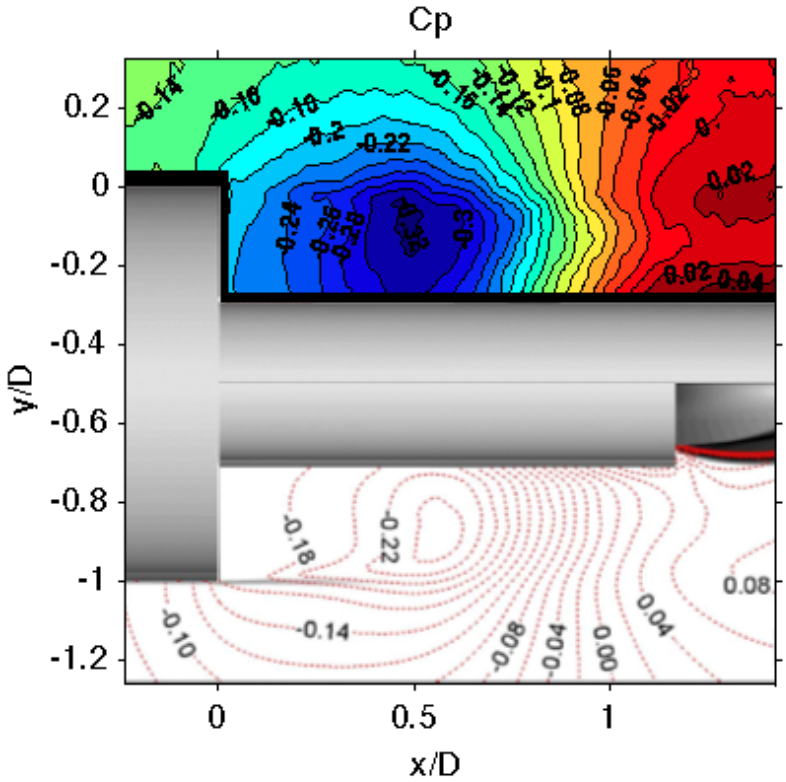

Figure 6.6: (top): C_p contours by Poisson solver with L/D=2.0 afterbody, black edge on model is outline of mask. (bottom) CFD results from Deck and Thorigny [2007] with L/D=1.2 afterbody and ideally expanded exhaust jet.

The pressure field for the long afterbody configuration ($L/D = 2.0$) is shown in Figure 6.6 together with the results from Deck and Thorigny [2007]. The afterbody in Deck and

Thorigny [2007] only extends to $L/D = 1.2$ but it features an exhaust jet. As reported by Deprés et al. [2004] the effect of an exhaust jet on the recirculation area is very little in case the jet exhaust is downstream of the reattachment point. This is confirmed by comparing the results of Weiss et al. [2009] (Figure 6.5, bottom) and Deck and Thorigny [2007] (Figure 6.6, bottom). Both studies obtained similar pressure contours in the recirculation region. Moreover when comparing the result from Deck and Thorigny [2007] with the pressure field of the long afterbody in Figure 6.6, the similarity in the contour lines is even stronger especially in the region downstream of the reattachment point. This indicates that an ideally expanded exhaust jet effectively functions as if a solid boundary were present. Finally when comparing the obtained pressure values to their CFD counterparts in Figures 6.5 and 6.6, we clearly see that pressure field obtained in the current experiment features lower values up to $x/D \approx 0.8$. While the minimum pressure found in the CFD results by Deck and Thorigny [2007] and Weiss et al. [2009] is on the order of $C_p \approx -0.22$, in the current experiment the minimum pressure is found to be $C_p \approx -0.32$. The cause for this will be discussed shortly.

The surface pressure distribution as computed by the Poisson solver along the afterbody is shown in Figure 6.7. Also shown in Figure 6.7 is the data obtained from the pressure ports in the wind tunnel model. For comparison in Figure 6.8 the results as reported by Weiss et al. [2009], Meliga and Reijasse [2007b] and Deprés et al. [2004] are shown.

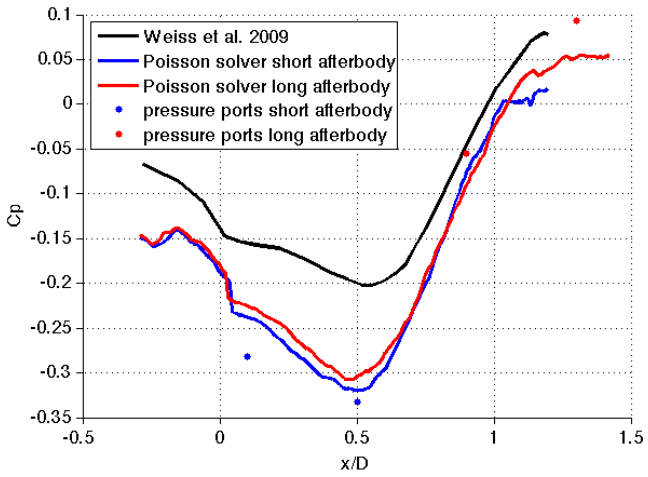

Figure 6.7: C_p distribution on the afterbody surface.

Note that the mask used in the Poisson solver is slightly larger than the actual model. Hence in order to determine the pressure distribution along the actual surface of the model, the Cp values obtained from the Poisson solver are linearly extrapolated towards the position of the model surface. However due to the pressure gradient being almost zero normal to the surface, this extrapolation has no substantial effect in terms of estimating the surface pressure as illustrated in Figure 6.9. Before we start comparing the results with literature, the Poisson solution itself needs to be examined. As an additional means to verify the result obtained by the Poisson solver, the wind tunnel model was fitted with pressure ports. The surface pressure as measured by these pressure ports are plotted in Figure 6.7 along with the Poisson solution. It appears that in the recirculation region the pressure ports measure a slightly lower pressure than would be expected from the Poisson solver. However further

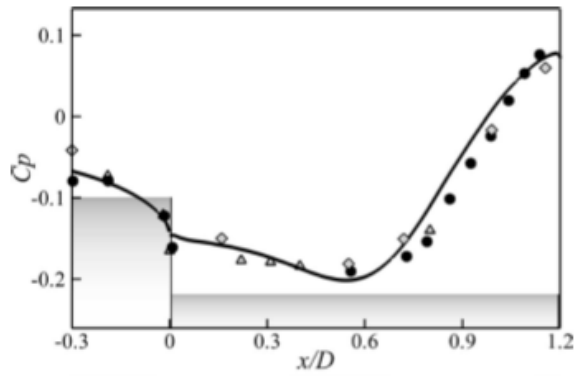

Figure 6.8: C_p distribution on the afterbody surface as reported in literature. -: Weiss et al. [2009] (CFD); •: Meliga and Reijasse [2007b](experimental); △, ◇: Deprés et al. [2004] (experimental). (Weiss et al. [2009]).

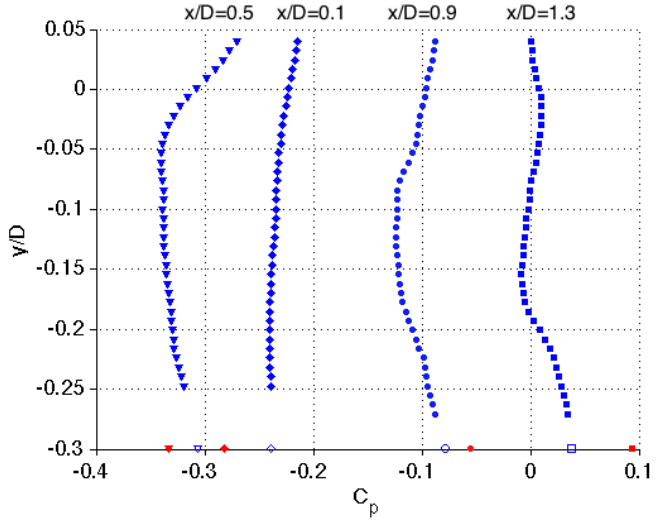

Figure 6.9: (blue): C_p profiles with extrapolated values. (red): C_p values measured by pressure ports.

downstream near and beyond the reattachment point, the pressure is slightly underestimated by the Poisson solver. Overall the Poisson solution seems to stay within the values measured by the transducers. In other words the Poisson solution does not reach the same extremes. Deviations up to approximately 12% of the measured C_p range are encountered. Considering the least-squares nature of the Poisson solution it seems plausible that near the model surface where Dirichlet boundary conditions are absent, the solution shows slight deviations as a result of the tendency to attenuate extremes. Another reason could be that the PIV dataset is not large enough and that the unsteady flow variables are not sufficiently resolved.

Regardless of the actual cause of the deviations, the most straightforward approach into improving the Poisson solution is to specify Dirichlet boundary conditions (provided by the pressure ports) along the surface. This will help guiding the solution toward the required values. It should be noted though that this is done with the assumption that the pressure data acquired by the transducers is more accurate than the solution generated by the Poisson

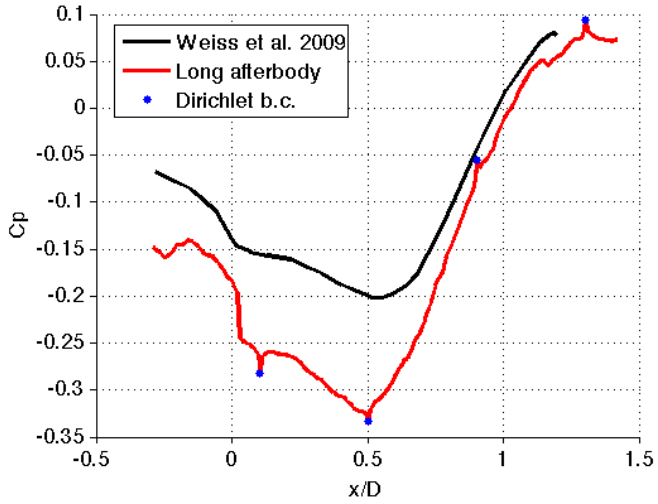

Figure 6.10: C_p distribution after applying pressure port data as Dirichlet conditions in the Poisson solver.

solver. Figure 6.10 shows the effect of using the pressure port measurements as Dirichlet conditions for the long afterbody configuration. Due to the pressure field similarity between the two afterbody configurations, it is assumed that the pressure port measurements corresponding to the short afterbody configuration are also representative for the long afterbody configuration. From Figure 6.10 it seems that applying the pressure port measurements as Dirichlet conditions does improve the overall Poisson solution in terms of fitting the pressure port data. the C_p curve now matches the values measured by the pressure ports (which is to be expected) while at the same time keeping the same overall trend. However at the locations where the Dirichlet conditions are prescribed a small localized peak can be discerned which is unphysical and therefore a point of concern. This is visible especially at x/D=0.1 and x/D=1.3 where the initial discrepancy was larger. The peaks indicate the tendency to move towards the original solution near the locations where Dirichlet conditions have been prescribed. It is expected that increasing the number of Dirichlet conditions evenly distributed across the boundary will smooth out the unphysical peaks in the solution. This could however not be tested in the current experiment due to the limited number of pressure ports available. Finally it is important to keep in mind that strictly speaking the pressure port values measured at the afterbody surface are not valid Dirichlet boundary conditions in the current experiment. This is because the computational domain of the Poisson solver is not actually bounded by the afterbody surface but by the applied mask which is larger in order to cover up reflections at the surface. Hence the location of the pressure port value does not correspond to the edge of the computational domain but is actually slightly outside. Hence using the pressure ports for Dirichlet conditions in this way should be done with care. Only if the mask follows the outline of the model exactly can the pressure port values regarded as valid boundary conditions. This indicates the importance of limiting reflections and keeping the mask as close to the actual model as possible. If the mask is too large, applying these Dirichlet boundary conditions will yield a pressure field that is not representative. In such cases the pressure field obtained by applying Neumann conditions would be more accurate.

After improving the Poisson solution for the surface pressure distribution by using the pressure

port data as Dirichlet boundary conditions, the solution is compared with literature. In addition to the Poisson solution Figure 6.10 also shows the solution obtained from the CFD study by Weiss et al. [2009] which agreed very well with experimental data reported by Meliga and Reijasse [2007b] and Deprés et al. [2004] (see Figure 6.8). It is evident that in the current experiment the pressure on the base (before separation) and in the recirculation region is found to be significantly lower than was reported by those other studies. Going further downstream however, the results start to match quite well. Recall that this trend was already observed in the pressure fields in Figure 6.5 and 6.6. Two possible causes for this discrepancy in the results are considered and discussed in the following.

First off the data mismatch might be the result of blockage effects in the wind tunnel. The blockage (ratio between frontal area of model to test section area) in the current experiment is 3%. As can be seen in Figure 6.10, the pressure on the model before separation is already lower than found by Weiss et al. [2009]. This could be the result of accelerated flow due to the blockage caused by the wind tunnel model. Downstream of separation point the pressure then decreases further due to the favorable pressure gradient towards the afterbody surface. Near the reattachment point the pressure distribution begins to resemble the reference data which consequently indicates that the blockage has diminished due to the afterbody diameter being smaller than the base diameter.

Another perhaps more likely explanation for the difference in the pressure values is found in the fact that in the other studies a slightly different flow geometry was used consisting of a cylindrical afterbody model without a nose (axisymmetric BFS). Recall that in the CFD study by Weiss et al. [2009] a mesh was used as shown in Figure 2.8. In the other experimental studies carried out in a wind tunnel, the afterbody was directly connected to a cylindrical sting running in upstream direction into the settling chamber. The free stream in these studies case referred to the inviscid flow region outside the boundary layer of the main cylindrical body. The free stream in the current experiment however corresponds to the flow entering the test section upstream of the wind tunnel model. The current experiment thus features a configuration with a full rocket model rather than the axisymmetric BFS configuration used in literature.

An attempt is made to compensate for this difference in flow configuration as follows. Instead of the actual free stream conditions ahead of the wind tunnel model, the flow conditions found in the isentropic region at the model base (indicated as ref1 in Figure 6.11) are used as reference values to normalize the pressure. This proved quite effective in recovering the pressure distribution found in literature. As illustrated in Figure 6.12a the new C_p distributions show a substantial improvement in terms of corresponding to the CFD results by Weiss et al. [2009]. The trends appear to be nearly identical. There is however a small offset in the absolute values. It should be noted that the current results start at a value $C_p \approx 0$ on the base ($x/D < 0$), which is no coincidence. This is to be expected since the reference pressure is obtained from the same region. Therefore the pressure near the base is almost the same as the reference pressure which consequently leads to a pressure coefficient $C_p \approx 0$. At this point it should become clear why the CFD results start lower. This can be explained by the fact that in Weiss et al. [2009] the reference conditions are taken much further upstream. In that case the pressure near the base is lower than the reference pressure because flow expansion occurs near the base. This also implies that the region as indicated in Figure 6.11 is too close to the base and affected too much by the flow expansion to provide the appropriate reference conditions for the acquired data. Hence it is expected that in order to further emulate the

normalization performed in Weiss et al. [2009], it is necessary to use flow conditions further upstream outside the influence of the flow expansion (indicated by ref2 in Figure 6.11). In the current experiment however the velocity further upstream is not measured since this is outside the FOV. Therefore it is also not possible to accurately determine the other relevant flow variables required for normalization. Therefore these upstream conditions are estimated under the assumption of isentropic flow and making use of the Area-Mach number relation (see, Anderson [2007]). Using these estimated flow conditions for normalization leads to a further improvement in matching the results as can be seen in Figure 6.12b.

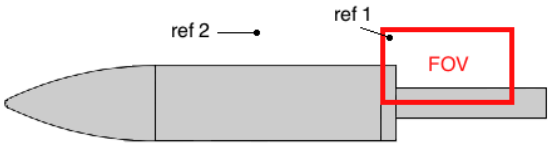

Figure 6.11: Alternative flow conditions used for normalization as indicated by ref 1 and ref 2.

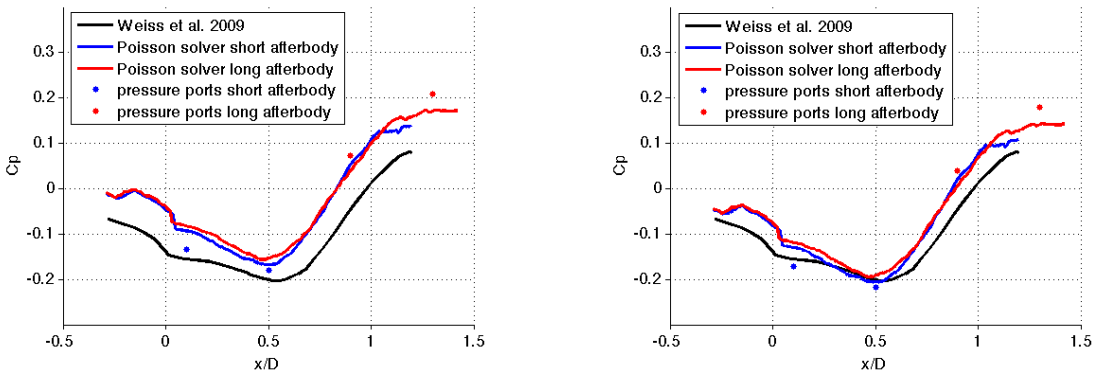

(a) normalization with ref 1 flow conditions.

(b) normalization with ref 2 flow conditions.

Figure 6.12: Effect of choosing different reference flow conditions for normalization purposes.

Finally we can continue fine tuning our chosen reference conditions until the best match in the data is obtained. The results are shown in Figures 6.13, 6.14 and 6.15. Notice that with the new normalization the shape of the contours have barely changed, but the absolute values now appear to correspond much better. A maximum difference of 17% with respect to the total C_p range is observed between the current results and what is found in literature. Also in the case of the blunt base configuration an improvement in the matching of the results can be observed. In Figure 6.16 the pressure across the base is replotted using the new normalizing quantities. The good agreement with literature obtained by using a different normalization, validates the accuracy of the current approach of reconstructing pressure from PIV data and attributes differences in the results mainly to inconsistent normalization rather than the accuracy of the approach itself. For the sake of consistency in our definition of free stream conditions however we continue to normalize the results as before, i.e. with the flow conditions found at the start of the wind tunnel test section, which is also more practical in the TST-27.

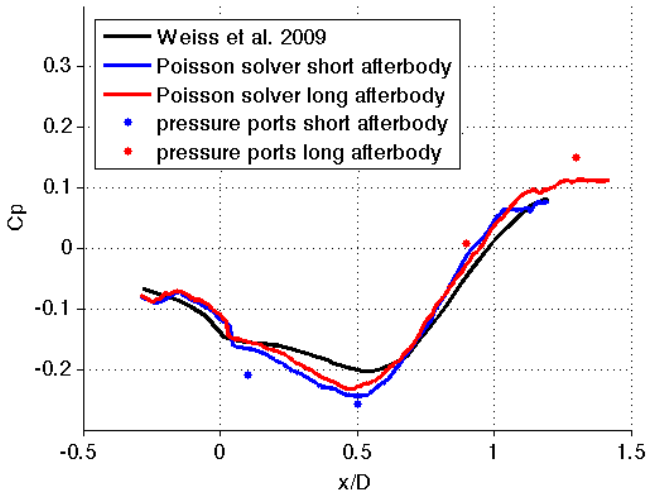

Figure 6.13: C_p surface distribution obtained by normalizing with flow conditions most comparable to literature.

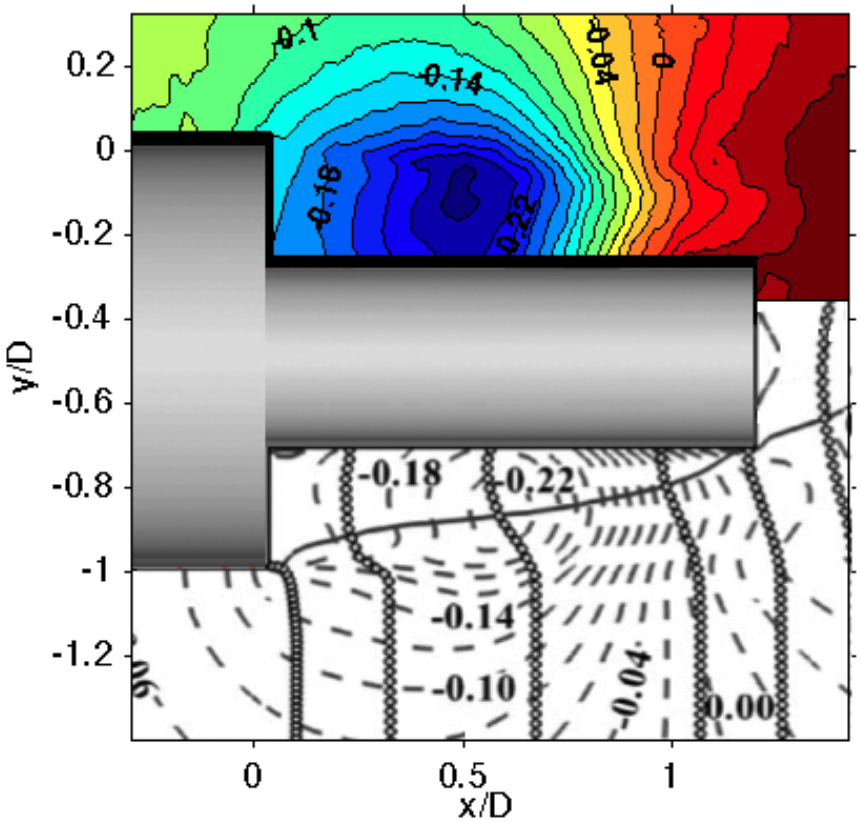

Figure 6.14: Short afterbody C_p contours obtained by normalizing with flow conditions most comparable to literature.

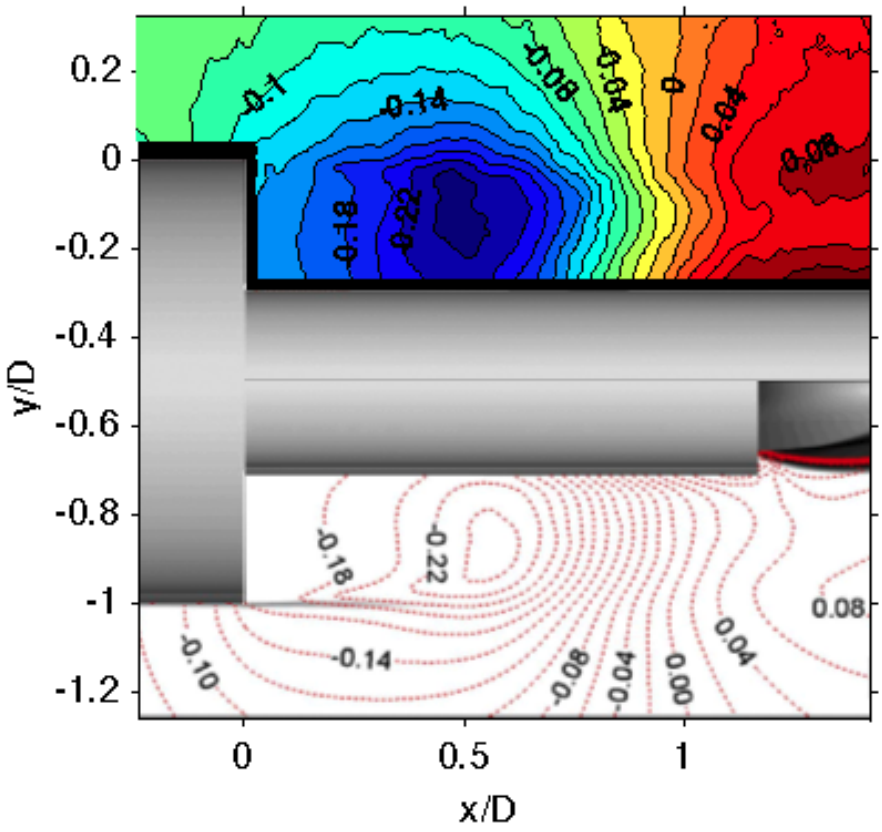

Figure 6.15: Long afterbody C_p contours obtained by normalizing with flow conditions most comparable to literature.

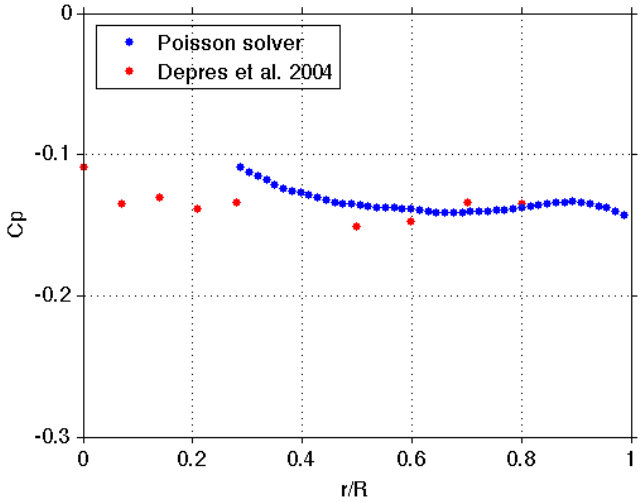

Figure 6.16: C_p distribution across the blunt base by normalizing with flow conditions most comparable to literature.

All in all this demonstrates the potential of using PIV data to compute the pressure field in a highly turbulent wake. The matching data between the Poisson solver and the pressure ports suggests that the current approach is a good alternative to either a purely numerical or experimental study. The advantages of this approach over a CFD study is that input data is obtained from an actual physical measurement and the relative ease of changing variables and configurations in between experiments. Compared to traditional experimental methods for pressure measurements such as pressure ports, the advantage is that instead of the pressure only being determined at specific locations on the model surface, a complete pressure field is obtained at once. Furthermore the advantage over a pitot probe or rake is evidently that the technique is non-intrusive.

6.5 Influence of Reynolds stresses

From turbulence modeling it is known that when a turbulent flow is analyzed in the mean (Reynolds averaged) sense, additional terms in the momentum equations appear known as the Reynolds stresses. Since the current experiment features a highly turbulent flow in the wake of the model, it might be worth evaluating the influence of these Reynolds stress terms on the pressure field. This is performed by changing the Navier-Stokes equations that serve as input to the Poisson solver such that the Reynolds stress terms are ignored. From the pressure field obtained this way (Figure 6.17b) the original solution (Figure 6.17a) is subtracted, the result of which is shown in Figure 6.17c. The differences in C_p are largest in regions of highly unsteady flow where the Reynolds stresses manifest themselves. This is demonstrated in particular in the shear layer. It appears that neglecting Reynolds stress in the Poisson formulation leads to an overestimation of the pressure in the wake. The maximum difference is observed in the shear layer being $\Delta C_p = 0.06$ corresponding to approximately 17% of the absolute C_p range.

An overall comparison of Figure 6.17a and 6.17b suggests that the inclusion of Reynolds stresses in the computation is not crucial to get a qualitative impression of the overall pressure field. Moreover the influence of Reynolds stresses near the surface is more moderate than in the shear layer. From Figure 6.18 it can be seen that the Reynolds stress terms have a relatively small impact on the resulting surface pressure distribution. This is not surprising since the fluctuations near the surface are less intense than in the mixing layer. The distributions generally match quite well, except near the point of minimum pressure where the difference becomes $\Delta C_p = 0.03$ which is about 8% of the total C_p range.

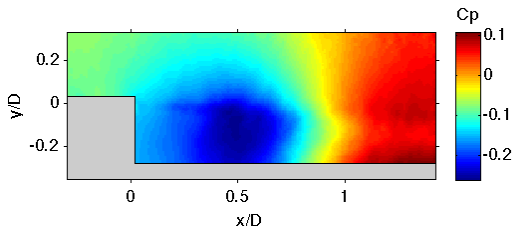

(a) $C_{p,full}$: solution of full Poisson formulation.

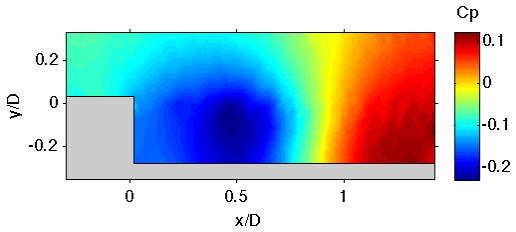

(b) $C_{p,noReynolds}$: solution obtained by omitting Reynolds stress terms in Poisson formulation.

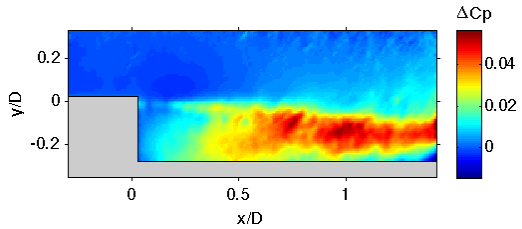

(c) $\Delta C_p = C_{p,noReynolds} - C_{p,full}$

Figure 6.17: Influence of the fluctuating terms (Reynolds stresses)

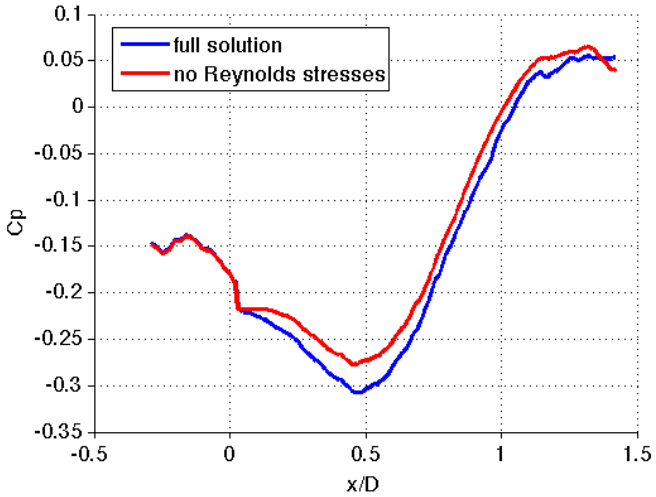

Figure 6.18: Influence of the Reynolds stresses on the afterbody pressure distribution.

6.6 Influence of field of view

For future experiments employing a similar approach i.e. computing the pressure with PIV data as input, it is worth investigating whether the chosen field of view has any effect on the results. The current field of view is chosen in order to be certain that at the upper boundary the flow is isentropic allowing Dirichlet boundary conditions to be applied. It would be good to know however what the minimum field of view is to achieve reliable results. Knowing this would allow zooming in on the region of interest to capture the flow with an optimal resolution. When applying boundary conditions for the Poisson solver, it is required to have a least one boundary condition specifying the pressure directly i.e. a Dirichlet condition in order for there to be closed system of equations that can be solved. Therefore in case of a pure PIV experiment it is necessary to include part of the isentropic flow in the field of view such that at least one Dirichlet boundary condition is available. However when direct pressure measurements are also available such as in the current experiment where the model is equipped with pressure ports, the isentropic flow is not required anymore for providing the Dirichlet boundary condition. It then suffices to just include the model surface with the pressure ports in the field of view, which greatly increases the freedom in choosing a small region of interest that can be imaged at high resolution.

First an analysis is performed using the original boundary conditions, i.e. Dirichlet on the top edge where isentropic flow may be assumed. The FOV is then decreased gradually in y-direction to see how this influences the quality of the Dirichlet boundary conditions. It is expected that as the isentropic flow assumption becomes invalid, the Dirichlet boundary condition will lead to larger discrepancies with the original solution. The differences with the original solution are normalized with a reference value (C_{pref}) corresponding to the absolute C_p range in the model wake. Shown in Figure 6.19 is ΔC_p with respect to the original solution obtained with different FOVs. Note how the errors in Figure 6.19a are the smallest. The chosen FOV here seems still large enough to include the isentropic flow along the top boundary. As the FOV is decreased to the step height shown in Figure 6.19b it is clear that the errors become larger because evidently the isentropic flow assumption is no applicable in this region. In particular near separation, the flow at the top boundary cannot be assumed isentropic since it coincides with the developing shear layer. Further downstream where the shear layer curves towards the wall, the flow at the top boundary is less affected by friction making the isentropic flow assumption more acceptable. In other words, the quality of the boundary conditions is worst near separation but improves in streamwise direction. This is also reflected in the results. Near the base the errors are largest and they decrease going in streamwise direction. Finally the result in Figure 6.19c confirms that as the FOV is reduced even further, the isentropic flow assumption does not hold anymore as the errors become much larger. Hence it can be conluded that in order to obtain the pressure field from only PIV data, one must guarantee the validity of isentropic flow in order to apply Dirichlet boundary conditions.

Next it is investigated how the positioning of boundary conditions affects the result for a given FOV. Assuming the presence of pressure ports on the model, the FOV can in theory be placed over a non-isentropic flow as long as part of the model surface is included where the pressure is known so that a Dirichlet boundary condition can be provided. This is done as shown in Figure 6.20. Dirichlet boundary conditions are extracted from the original solution and specified on the afterbody surface at the locations $x/D = 0.35$, $x/D = 0.75$ and $x/D = 1.15$

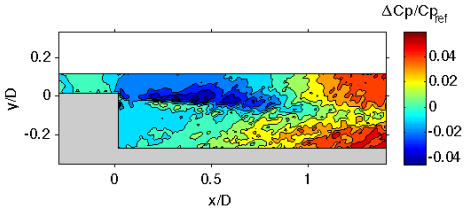

(a) ΔC_p resulting from applying isentropic b.c. on top edge

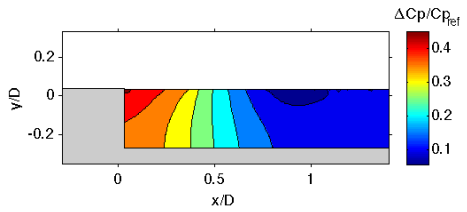

(b) ΔC_p resulting from applying isentropic b.c. on top edge

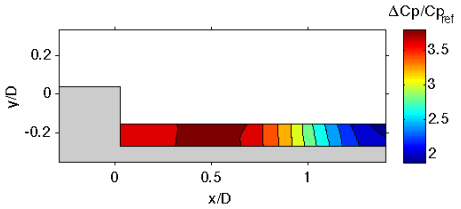

(c) ΔC_p resulting from applying isentropic b.c. on top edge

Figure 6.19: Influence of the FOV on pressure evaluation

which will be refered to as BC1, BC2 and BC3 respectively. Figure 6.20a shows the case with Dirichlet applied on all three locations. The result in (b) is obtained by only specifying BC1. It becomes clear that the errors remain small in the vicinity of the boundary condition (on the order of 5%), but as we move farther away the pressure deviates more from the original solution reaching error levels of 35%. By only applying BC2 as shown in (c), a similar result is obtained where the errors are smallest near the location of the boundary condition. Due to the more central location of BC2 compared to BC1, the maximum error is reduced to 25%. Finally the same trend continues when just BC3 is used as shown in (d). This time the maximum error typically found in the region downstream of reattachment is now reduced to 10%. It should be noted that in going from BC1 to BC3 the overall error in the pressure field seems to diminish. This demonstrates that not all boundary condition locations have the same impact and that certain locations are more effective. Comparing Figure 6.20a and (d) it can be seen that only applying BC3 gives almost the same result as applying all three boundary conditions. This suggests that the positioning of a Dirichlet boundary condition at an effective location is more important than the number of different locations used. The reason for the relative importance of BC3 could be that in that region the flow field exhibits larger variations due to the Reynolds stress terms being more dominant. Since the Poisson solution is essentially a least-squares solution, a flow region featuring larger gradients is more likely to result in deviating solutions. Hence the solution is greatly improved by specifying what the exact pressure should be in that region. Finally in Figure 6.20e the FOV is also reduced in the horizontal direction. Three regions are considered that are each centered around a boundary condition at the wall. The result shows that very small FOVs are acceptable as well.

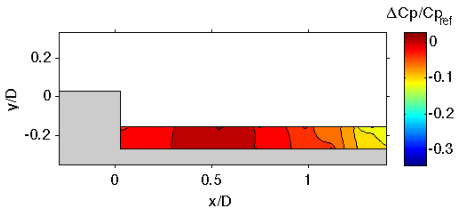

(a) ΔC_p resulting from applying isentropic b.c. on afterbody surface at x/D=0.35, x/D=0.75 and x/D=1.15

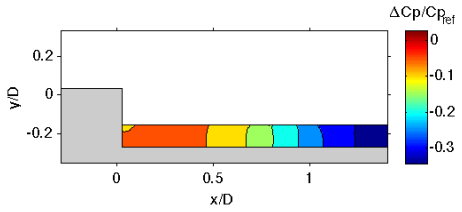

(b) ΔC_p resulting from applying isentropic b.c. at x/D=0.35 on afterbody surface

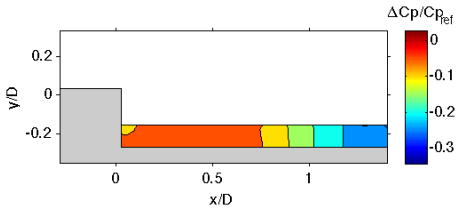

(c) ΔC_p resulting from applying isentropic b.c. at x/D=0.75 on afterbody surface

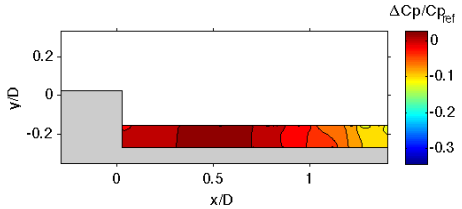

(d) ΔC_p resulting from applying isentropic b.c. at x/D=1.1 on afterbody surface

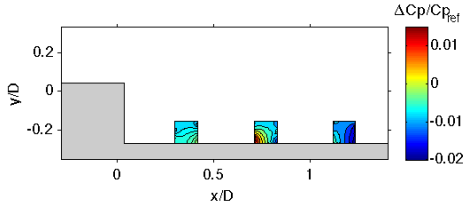

(e) ΔC_p field for several small FOVs centered around the Dirichlet boundary conditions

Figure 6.20: Influence of the FOV/b.c. on pressure evaluation

6.7 Uncertainty analysis

The results of the pressure evaluation are based on statistical experimental data. It is therefore to be expected that the obtained results will not correspond exactly to the actual values for a given experimental configuration and free stream conditions. The statistical convergence of the velocity field is determined in order to assess the uncertainty of the velocity measurement. Furthermore there are additional factors that have an impact on the accuracy of the pressure computation. These are discussed shortly and taken into account as well in an uncertainty analysis performed to assess the error involved with the reconstruction of the pressure field. Due to the strong resemblance in the afterbody configurations only the results for the long afterbody are shown. The analysis is carried out separately for the isentropic part of the flow and the non-isentropic part. Note that from here on the overbar denoting time averaged quantities is omitted e.g. $\overline{u}$ simply becomes u.

6.7.1 Statistical convergence

The mean velocity fields are obtained by averaging approximately 450 instantaneous samples of the unsteady flow field. The accuracy of the computed mean, also known as the ensemble average, depends on the number of statistically independent samples used. At a certain number of samples, the ensemble average will start to converge towards the actual mean becoming more accurate as more samples are used. The actual mean is however defined as the value obtained from averaging an infinite number of samples which is not possible in practice. Since the true mean can never be obtained it is important to make an estimate of how close the ensemble average is to the actual mean given a number of samples N. In other words the statistical convergence needs to be determined in order to assess whether the mean has been computed with acceptable accuracy. In turbulent flows, the degree of statistical convergence of the mean velocity obtained from N samples is measured by the expression:

$$\epsilon = \frac{\sigma}{\mu\sqrt{N}} \sim \frac{1}{\sqrt{N}} \tag{6-19}$$

where ϵ is the normalized error or deviation, μ is the mean and σ is the RMS value of the turbulent velocity fluctuations, called the turbulence intensity when normalized by the mean velocity. In the same way equation (6-19) is used to assess the accuracy of the Reynolds stresses in which case σ denotes the RMS values of the fluctuations in $u'u'$, $v'v'$ or $u'v'$.

Table 6.1 shows the statistical convergence of the mean velocity components and Reynolds stresses for the different test configurations respectively. The statistical convergence is slowest where the largest fluctuations occur i.e. in the shear layer the error ϵ will be largest. Therefore the error of the respective flow variables concerns the error inside the shear layer. It appears that for all test configurations the flow variables converged to within 10 % error.

configuration	ϵ_U	ϵ_V	ϵ_{uu}	ϵ_{vv}	ϵ_{uv}
Blunt base	0.0241	0.0629	0.0595	0.0570	0.0728
Short afterbody	0.0234	0.0644	0.0612	0.0615	0.0774
Long afterbody	0.0246	0.0587	0.0589	0.0585	0.0821

Table 6.1: Statistical convergence in the shear layer

6.7.2 Isentropic flow region

For the uncertainty analysis the concept of *Linear Error Propagation* is used. This allows us to express the error of a certain quantity $A = f(x_1, x_2...x_i)$ in terms of the expected error of the variables x_i which A is a function of. For the special case where all variables x_i are uncorrelated, the expected error ΔA can be expressed as

$$\Delta A = \sqrt{\left(\frac{\partial A}{\partial x_1}\right)^2 \Delta x_1^2 + \left(\frac{\partial A}{\partial x_2}\right)^2 \Delta x_2^2 + ... + \left(\frac{\partial A}{\partial x_i}\right)^2 \Delta x_i^2} \tag{6-20}$$

It is important to note that (6-20) is based on the linear characteristics of the first-order derivatives $\frac{\partial A}{\partial x_i}$. Hence it is only serves as a good estimation of ΔA when Δx_i is small compared to its corresponding partial derivative.

For the current experiment, three variables are identified as the main contributors to the error in computing the mean pressure coefficient C_p and in addition are considered uncorrelated. These variables are the mean free stream pressure p_∞, mean free stream Mach number M_∞ and the mean velocity V as determined from PIV. Note that the overbar used for time-averaged quantities are omitted here.Thus we have the following

$$\Delta C_p = f(\Delta p_\infty, \Delta M_\infty, \Delta V) \tag{6-21}$$

where it should be kept in mind that the variables are treated in the mean sense and hence the errors are related to the statistical convergence. The error in the free stream conditions Δp_∞ and ΔM_∞ are due to small fluctuations inside the wind tunnel and are thus related to the degree of statistical convergence. They can be considered uncorrelated. Note that the error in the velocity ΔV depends not only on the free stream conditions, which means it is correlated with p_∞ and M_∞, but also on random errors introduced by the PIV measurement system and in case of turbulent flow as encountered in the wake also on fluctuations inherently present in the unsteady flow. The latter two sources of error in V are uncorrelated to the wind tunnel performance and are thus represented by ΔV in equation (6-21). Hence in analogy to equation (6-20) ΔC_p can be expressed as

$$\Delta C_p = \sqrt{\left(\frac{\partial C_p}{\partial p_\infty}\right)^2 \Delta p_\infty^2 + \left(\frac{\partial C_p}{\partial M_\infty}\right)^2 \Delta M_\infty^2 + \left(\frac{\partial C_p}{\partial V}\right)^2 \Delta V^2} \tag{6-22}$$

Since the flow is assumed isentropic, the first order derivatives in equation (6-22) can be computed analytically as shown in the following. First rewrite C_p

$$C_p = \frac{p - p_\infty}{\frac{1}{2}\rho_\infty V_\infty^2} = \frac{\frac{p}{p_\infty} - 1}{\frac{1}{2}\gamma M_\infty^2} \tag{6-23}$$

Next the partial derivatives of C_p are determined with respect to p_∞ and M_∞ respectively using equation (6-23). This results in

$$\frac{\partial C_p}{\partial p_\infty} = -\frac{\frac{p}{p_\infty^2}}{\frac{1}{2}\gamma M_\infty^2} \tag{6-24}$$

$$\frac{\partial C_p}{\partial M_\infty} = \frac{4 - 4\left(\frac{p}{p_\infty}\right)}{\gamma M_\infty^3} \tag{6-25}$$

For the derivative with respect to V recall that in isentropic flows the following holds

$$\frac{p}{p_\infty} = \left(1 + \frac{\gamma - 1}{2} M_\infty^2 \left(1 - \frac{V^2}{V_\infty^2}\right)\right)^{\frac{\gamma}{\gamma - 1}} \tag{6-26}$$

Substituting equation (6-26) into (6-23) then allows taking the partial derivative which leads to

$$\frac{\partial C_p}{\partial V} = -2\frac{V}{V_\infty^2}\left(1 + \frac{\gamma - 1}{2} M_\infty^2 \left(1 - \frac{V^2}{V_\infty^2}\right)\right)^{\frac{1}{\gamma - 1}} \tag{6-27}$$

The result of applying equation (6-22) on the flow field is shown in Figure 6.21. The solution is valid in the isentropic flow only. Therefore the values in the wake where the assumption of isentropic flow does not hold are masked.

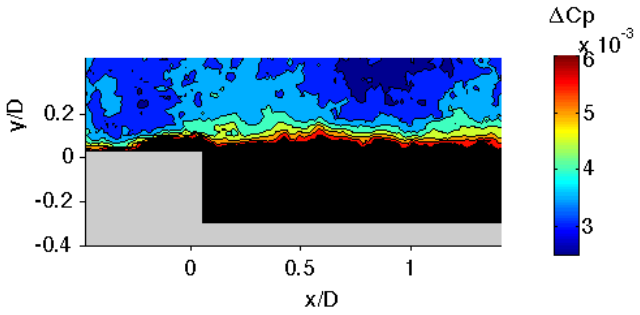

Figure 6.21: ΔC_p resulting from isentropic flow assumptions for the long afterbody configuration.

6.7.3 Wake region

Performing the uncertainty analysis for the wake region i.e. non-isentropic part of the flow requires a slightly different approach because the isentropic relations are not valid anymore. Therefore the first order derivatives of C_p in equation (6-22) cannot be determined in analytical form and a numerical approach is required using the Navier-Stokes equations. Thus the derivatives in equation (6-22) are to be determined numerically. This is done by introducing artificial errors in the input data, then computing the solution using the Poisson solver and finally comparing the results to the nominal case which has no artificial error. The numerical derivative is then simply the difference in the resulting C_p divided by the artificial error:

$$\frac{\partial C_p}{\partial x_i} \approx \frac{\Delta C_p}{\Delta x_i} \tag{6-28}$$

Note that with this numerical approach the errors are now determined by running the Poisson solver. Since the resulting solution can be viewed as a least-squares fit of the pressure throughout the domain which means local variations are smoothed out. This means that local effects of the artificially introduced errors cannot be properly resolved since they are diminished by the least-squares fit. Hence contrary to the case of isentropic flow where the uncertainty can be determined locally (i.e. equation (6-22) is solved for individual points in the flow field), a global approach is required here. Hence, instead of looking at what ΔC_p is at a single point, we look at the overall change in C_p throughout the whole domain as a result of introducing artificial errors. In addition notice that unlike in isentropic flow where C_p can be explicitly written as a function of V, now pressure is dependent on u and v as expressed by the Navier-Stokes equations. Hence equation (6-22) becomes

$$\Delta C_p = \sqrt{\left(\frac{\partial C_p}{\partial p_\infty}\right)^2 \Delta p_\infty^2 + \left(\frac{\partial C_p}{\partial M_\infty}\right)^2 \Delta M_\infty^2 + \left(\frac{\partial C_p}{\partial u}\right)^2 \Delta u^2 + \left(\frac{\partial C_p}{\partial v}\right)^2 \Delta v^2} \tag{6-29}$$

where Δp_∞ and ΔM_∞ are still the same as before. But ΔC_p, Δu and Δv now represent global quantities.

The different terms in equation (6-29) are obtained as follows. First off, the uncertainty throughout the velocity field relating to the statistical convergence is averaged to obtain a value to represent the whole domain. Thus Δu and Δv in equation (6-29) correspond to the spatially averaged values of the domain. To obtain the numerical approximations for $\frac{\partial C_p}{\partial u}$

and $\frac{\partial C_p}{\partial v}$, an artificial noise level is introduced in the velocity field. The noise is created by inserting Gaussian distributed random values into the mean velocity field with zero mean and a standard deviation of 1%. These values are then multiplied with the local velocity of the original velocity field which results in a field of velocity vectors due to artificial noise. The average u and v component in this noise related velocity field are then used for ∂u and ∂v respectively. Additionally the created velocity noise is superimposed on the original velocity field to be used as input to compute the new pressure field. The spatially averaged difference between this new pressure field and the one obtained from the original velocity data is then used for ∂C_p. We thus have obtained both the numerator and denominator for $\frac{\partial C_p}{\partial u}$ and $\frac{\partial C_p}{\partial v}$. In case of $\frac{\partial C_p}{\partial p_\infty}$ and $\frac{\partial C_p}{\partial M_\infty}$, ∂C_p also corresponds to the average value. Note however that the distinction between local and global quantities does not apply to ∂p_∞ and ∂M_∞ used to generate ∂C_p and hence they are exactly the same as in the isentropic case. The results are shown in Figure 6.22 and Table 6.2. The uncertainty is $\Delta C_p = 0.0072$ which accounts for 2% of the total range in the wake. Furthermore it appears that the error terms corresponding to the velocity fluctuations are the largest contributor to the error in C_p.

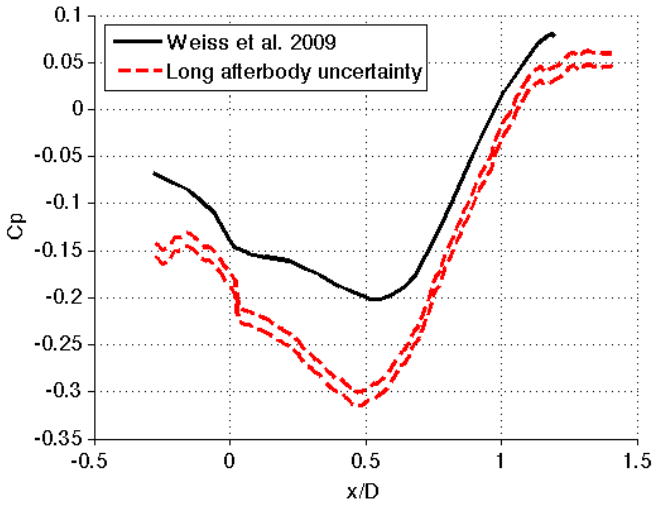

Figure 6.22: Uncertainty in C_p distribution.

	ΔC_p (averaged error)
ΔM_∞	$3.11 \cdot 10^{-5}$
Δp_∞	6.80Pa
$\Delta \overline{u}$	1.13m/s
$\Delta \overline{v}$	0.82m/s
$\frac{\partial C_p}{\partial M_\infty}$	0.22
$\frac{\partial C_p}{\partial p_\infty}$	$1.94 \cdot 10{-}5\mathrm{Pa}^{-1}$
$\frac{\partial C_p}{\partial \overline{u}}$	0.0063s/m
$\partial \overline{u}$	1.57m/s
$\frac{\partial C_p}{\partial \overline{v}}$	0.0013s/m
$\partial \overline{v}$	0.10m/s
$\left(\frac{\partial C_p}{\partial M_\infty}\right) \Delta M_\infty$	$6.80 \cdot 10^{-6}$
$\left(\frac{\partial C_p}{\partial p_\infty}\right) \Delta p_\infty$	$1.32 \cdot 10^{-4}$
$\left(\frac{\partial C_p}{\partial \overline{u}}\right) \Delta \overline{u}$	$7.2 \cdot 10^{-3}$
$\left(\frac{\partial C_p}{\partial \overline{v}}\right) \Delta \overline{v}$	$1.0 \cdot 10^{-3}$
ΔC_p	0.0072

Table 6.2: Estimates for the error in C_p for the long afterbody configuration

Chapter 7

Conclusion

7.1 Conclusions

Wind tunnel experiments have been performed on a model rocket at Mach 0.7. The Reynolds number based on the diameter of the model is equal to $Re_D = 1.3 \cdot 10^6$. Three test configurations of the model base were considered: a) blunt base, b) afterbody extending up to $L/D = 1.2$, c) afterbody extending up to $L/D = 2.0$.

The mean velocity field and Reynolds stresses have been characterized in the wake of the model using PIV. For each test configuration a sample size of 400-500 instantaneous velocity fields was used to obtain the mean flow variables. The statistical error for all flow variables converged to within 10%. A boundary layer analysis of the flow near the separation point at the base confirmed that the boundary layer is turbulent before separation. Furthermore the growth rate of the free shear layer resulting from the boundary layer separation at the base has been investigated. As reported in literature, the growth rate of a free planar mixing layer is found to be approximately 0.17. In the current experiment the separated shear layer up to x/D=0.6 was considered outside the influence of the wall and therefore approximates the classic planar mixing layer. The growth rate was found to be ≈ 0.36 however. This result corresponds to the findings of Deck and Thorigny [2007] who suggested that the larger growth rate is caused by reingestion of turbulent structures from the recirculation region back into the developing shear layer.

Considering the overall flow field it has been found that the maximum backflow velocity in the recirculation region reached up to $35\% - 40\%$ of the free stream velocity. In case of the blunt base the fluidic reattachment point of the separated shear layer is estimated at $x/D \approx 1.1$. The experiments with afterbody configurations show a reattachment point at $x/D \approx 1.0$. Furthermore the case of hybrid reattachment ($L/D = 1.2$) showed that the shear layer reattachment was fluidic 18% of the time. Finally for both afterbody configurations the secondary corner vortex has been revealed. Previous studies carried out at TU Delft were unable to discover this secondary vortex. The current project however has confirmed the existence of the phenomenon.

In addition to characterizing the velocity field, the mean pressure field is computed numerically using the PIV data as input. A Poisson formulation for the pressure in terms of velocity is derived from the Reynolds averaged Navier-Stokes equations. This is solved using a numerical Poisson solver which uses PIV data to provide all the velocity terms. The results are validated with data obtained from pressure ports on the model as well as CFD solutions of Deck and Thorigny [2007] and Weiss et al. [2009]. The maximum difference in C_p between the current results and the CFD data occurs in the center of the recirculation zone and is found to be 17% with respect to the total C_p range in the wake. Between the surface pressure distribution generated by the Poisson solver and the pressure port data a maximum difference of 12% is observed. This difference can be reduced if the pressure port data is applied as Dirichlet boundary conditions in the Poisson solver. This results in a better match between the Poisson solution and the pressure port data, however a point of concern is that near the locations where the Dirichlet conditions are enforced, the solution becomes unphysical showing local peaks. It is expected that increasing the number of Dirichlet conditions evenly distributed across the boundary will smooth out the unphysical peaks in the solution. This could however not be tested in the current experiment due to the limited number of pressure ports available.

The flow considered is highly turbulent which suggests the importance of accurately resolving the Reynolds stresses that appear in the equations to be solved. It is not known however what the exact effect is of including/ignoring the Reynolds stress terms in the computation. To assess this the numerical solver was run using a simplified Poisson formulation where the turbulent stresses were ignored. The result was compared to the original solution. It was found that the effect of Reynolds stresses was most dominant in regions where the turbulent fluctuations are also largest which was to be expected. When the Reynolds stresses were neglected this resulted in an overestimation of C_p in the region of highly turbulent flow with a maximum of 17% of the absolute C_p range. Closer to the surface the intensity of the fluctuations is less, therefore the impact of neglecting the Reynolds stress terms is also diminished. A maximum of 8% deviation was observed at the surface while the overall trend was kept intact. The result suggests that in case only the surface pressure is of interest, it is sufficient to solve for the pressure with the simplified Poisson formulation in combination with the pressure ports to provide the required Dirichlet conditions. This also implies that there is no need to acquire large PIV datasets to ensure statistical convergence of the turbulent stress terms, since they can be omitted.

The field of view (FOV) was chosen such that the pressure computation could be performed on a domain with suitable boundary conditions. The FOV covered the model surface and the full recirculation region while extending into the flow region that could be assumed isentropic. This allowed one of the boundaries to be fixed with Dirichlet boundary conditions for the pressure using PIV data and isentropic flow relations (Note that the Poisson solver requires at least one Dirichlet condition). On the other boundaries Neuman conditions were prescribed. The results obtained in this way were good as discussed in the above. However this approach is also limited in the sense that the user needs to extend the FOV such that he can guarantee the isentropic flow assumption in order to prescribe Dirichlet conditions. Consider the hypothetical case where one wants to zoom in on a particular part in the flow to increase the spatial resolution. This is hindered by the necessity to incorporate part of the isentropic flow for the required Dirichlet condition. Hence an attempt was made to reconstruct the original pressure solution using cropped FOVs that did not incorporate the isentropic flow region but included the model surface. Note that the decrease in FOV by

cropping the PIV data as was done in this case implies that there was no increased spatial resolution. Several Dirichlet conditions based on the original solution were then inserted on the model surface as if they were obtained from pressure port data. The resulting pressure fields indicate that this alternative approach is indeed able to resolve the pressure field with good accuracy. Especially in the vicinity of the prescribed Dirichlet condition the accuracy can be guaranteed which is somewhat to be expected. Errors of just a few percent with respect to the absolute C_p range were achieved.

An uncertainty analysis is performed on the computed pressure field. For this linear error propagation is used. Due to the nature of the Navier-Stokes equations it is not possible to derive the error propagation terms in analytic form. Due to the lack of an analytic formulation the uncertainty cannot be expressed as a function of local variables. Hence a numerical approach is used which estimates the uncertainty of C_p as a spatial average. This yielded an (average) uncertainty of 2% relative to the total C_p range in the wake.

The outcome of the experiments suggests that the current approach of evaluating pressure with PIV data is a good alternative to either a purely numerical or experimental study. The advantages of this approach over a CFD study is that input data is obtained from an actual physical measurement and the relative ease of changing variables and configurations in between experiments. Compared to traditional experimental methods for pressure measurements such as pressure ports, the advantage is that instead of the pressure only being determined at specific locations on the model surface, a complete pressure field is obtained at once. Furthermore the advantage over a pitot probe or rake is evidently that the technique is non-intrusive.

7.2 Recommendations and outlook

The wind tunnel model used during the project has shown to be well suited to simulate afterbody flows. The sting has negligible influence such that the axis symmetry of the wake is maintained. In addition the boundary layer is able to become fully turbulent before separating at the base. Also the back of the model can be conveniently fitted with a blunt base or an afterbody with variable extension. The only downside of the current model is the limited amount of only two pressure ports being available at one time. For future experiments that use a similar approach it is highly recommended to use a model with an array of pressure ports along the surface so that validating the computed pressure can be done more effectively. Moreover it has been found that the best results are obtained by using the Poisson solver in combination with pressure ports to provide Dirichlet conditions at the surface. A key requirement for correctly applying this however is that the mask used in the Poisson solver should correspond to the outlines of the model as much as possible. This can be difficult to achieve if the wind tunnel model shows strong laser reflections off its surface during the PIV measurement. Thus reflections should be kept at a minimum, by coating the model in black and using a laser intensity not higher than necessary.

With the current project it has been shown that integrating the mean pressure field from PIV data can be done for highly turbulent compressible flows and with good results. A natural follow-up to the current project would be to attempt resolving instantaneous pressure fields. Time resolved pressure fields will help gain a better understanding of the dynamics of

afterbody flow. Note that for integrating the instantaneous pressure, the Poisson formulation will differ. Instead of the Reynolds averaged Navier-Stokes equations as used in the current project, the original equations are used. Hence no Reynolds stresses are involved. On the other hand an additional acceleration term appears in the equations. In order to resolve this time derivative term for the velocity with PIV, the equipment must be able to generate three laser pulses in succession as well as record three frames. In practice, considering the properties of the lasers available at the laboratory, this means synchronzing two separate laser systems to generate these three pulses. Also special attention should be paid to achieving a PIV setup where the quality of the instantaneous velocity fields is good (in the current project this was less critical because the velocity fields were analyzed and used in a time averaged sense). A good starting point for the follow-up would be the recent work by De Kat and Van Oudheusden [2010] who investigated the potential of using PIV to determine instantaneous pressure fields in an incompressible flow.

The ability to resolve instantaneous pressure fields can aid us in gaining new insights concerning the dynamic behavior of the flow. It is expected that applying Proper Orthogonal Decomposition (POD) analysis on the instantaneous pressure fields will help offer new insights into the buffeting phenomenon and help identify particular modes in the flow that are most prevalent in contributing to the buffeting phenomenon. The next step would be to find out how these modes respond to certain flow disturbances. As a result perhaps more targeted attempts can be made to reduce the buffeting loads by addressing the most important modes in the flow.

Bibliography

Anderson, J. (2007). *Fundamentals of Aerodynamics*. McGraw-Hill. Boston.

Bitter, M., Scharnowski, S., Hain, R., and Kähler, C. (2010). High-repetition-rate piv investigations on a generic rocket model in sub-and supersonic flows. *Experiments in fluids*, pages 1–12.

Cherry, N., Hillier, R., and Latour, M. (1984). Unsteady measurements in a separated and reattaching flow. *Journal of Fluid Mechanics*, 144:13–46.

Cole, H., Erickson, A., Rainey, A., Aeronautics, N., and Space Administration, Washington, D. (1970). Buffeting during atmospheric ascent- space vehicle design criteria/structures/(aeroelastic spacecraft design to minimize buffeting during atmospheric ascent). Technical report, National Aeronautics and Space Administration, Washington, DC.

De Kat, R. and Van Oudheusden, B. (2010). Instantaneous planar pressure from piv: analytic and experimental test-cases. In *15th Int Symp on Applications of Laser Techniques to Fluid Mechanics Lisbon, Portugal, 06-06 July, 2010*, page 13.

De Kat, R., Van Oudheusden, B., and Scarano, F. (2008). Instantaneous planar pressure field determination around a square-section cylinder based on time-resolved stereo-piv. In *14th Int Symp on Applications of Laser Techniques to Fluid Mechanics Lisbon, Portugal, 07-10 July, 2008*, page 11.

Deck, S. and Thorigny, P. (2007). Unsteadiness of an axisymmetric separating-reattaching flow: Numerical investigation. *Physics of fluids*, 19:065103.

Deprés, D., Reijasse, P., and Dussauge, J. (2004). Analysis of unsteadiness in afterbody transonic flows. *AIAA journal*, 42(12):2541–2550.

Elliott, G. and Samimy, M. (1990). Compressibility effects in free shear layers. *Physics of Fluids A: Fluid Dynamics*, 2:1231.

Fuchs, H., Mercker, E., and Michel, U. (1979). Large-scale coherent structures in the wake of axisymmetric bodies. *Journal of Fluid Mechanics*, 93(01):185–207.

Fung, Y. (2002). *An introduction to the theory of aeroelasticity*. Dover Pubns.

Heenan, F. and Morrison, J. (1998). Passive control of pressure fluctuations generated by separated flows. *AIAA paper*, (36-1014).

Herrin, J. and Dutton, J. (1994). Effects of afterbody boattailing on the near-wake of axisymmetric bodies in supersonic flow. In *AIAA, Aerospace Sciences Meeting & Exhibit, 32 nd, Reno, NV*.

Herrin, J. and Dutton, J. (1995). Effect of a rapid expansion on the development of compressible free shear layers. *Physics of Fluids*, 7:159.

Ho, C. and Huang, L. (1982). Subharmonics and vortex merging in mixing layers. *J. Fluid Mech*, 119:443–473.

Hudy, L. M., Naguib, A. M., and Hunphreys, W. M. (2003). Wall-pressure-array measurements beneath a separating/reattaching SSow region. *Physics of fluids*, 15:706.

Huerre, P. and Monkewitz, P. (1990). Local and global instabilities in spatially developing flows. *Annual Review of Fluid Mechanics*, 22(1):473–537.

Kumar, R., Viswanath, P. R., and Prabhu, A. (2002). Mean and fluctuating pressure in boat-tail separated flows at transonic speeds. *Journal of Spacecraft and Rockets*, 39:430.

Mehta, R. and Westphal, R. (1986). Near-field turbulence properties of single-and two-stream plane mixing layers. *Experiments in fluids*, 4(5):257–266.

Meliga, P. and Reijasse, P. (2007a). Reduction of unsteadiness in the transonic flow past an axisymmetric afterbody with two boosters.

Meliga, P. and Reijasse, P. (2007b). Unsteady transonic flow behind an axisymmetric afterbody with two boosters. In *Proceedings of the 25th AIAA Applied Aerodynamics Conference, Miami*, volume 2007, page 4564.

Meliga, P., Reijasse, P., and Chomaz, J. (2007). Effect of a serrated skirt on the buffeting phenomenon in transonic afterbody flows. In *Proceedings of the IUTAM Symposium Unsteady Separated Flows and their Control, Corfu, Greece*, pages 18–22.

Pope, S. (2000). *Turbulent flows*. Cambridge Univ Pr.

Raffel, M., Willert, C., Wereley, S., and Kompenhans, J. (2007). *Particle image velocimetry: a practical guide*. Springer Verlag.

Ragni, D., Ashok, A., van Oudheusden, B., and Scarano, F. (2009). Surface pressure and aerodynamic loads determination of a transonic airfoil based on particle image velocimetry. *Measurement Science and Technology*, 20(7):074005.

Ragni, D., van Oudheusden, B., and Scarano, F. (2012). 3d pressure imaging of an aircraft propeller blade-tip flow by phase-locked stereoscopic piv. *Experiments in fluids*, 52(2):463–477.

Rainey, A. (1965). Progress on the launch-vehicle buffeting problem. *Journal of Spacecraft and Rockets*, 2:289–299.

Richard, H. and Raffel, M. (2001). Principle and applications of the background oriented schlieren (bos) method. *Measurement Science and Technology*, 12:1576.

Schrijer, F., Sciacchitano, A., and Scarano, F. (2010). Experimental investigation of flow control devices for the reduction of transonic buffeting on rocket afterbodies.

Smits, A. and Dussauge, J. (2006). *Turbulent shear layers in supersonic flow*. Springer Verlag.

Spazzini, P., Luso, G., Onorato, M., Zurlo, N., and Di Cicca, G. M. (2001). Unsteady behavior of back-facing flow. *Experiments in Fluids*, 30:551.

Tennekes, H. and Lumley, J. (1972). *A first course in turbulence*. The MIT press.

Van Oudheusden, B. (2008). Principles and application of velocimetry-based planar pressure imaging in compressible flows with shocks. *Experiments in fluids*, 45(4):657–674.

van Oudheusden, B., Scarano, F., Roosenboom, E., Casimiri, E., and Souverein, L. (2007). Evaluation of integral forces and pressure fields from planar velocimetry data for incompressible and compressible flows. *Experiments in Fluids*, 43:153–162.

Venkatakrishnan, L. and Meier, G. (2004). Density measurements using the background oriented schlieren technique. *Experiments in Fluids*, 37(2):237–247.

Wee, D., Yi, T., Annaswamy, A., and Ghoniem, A. (2004). Self-sustained oscillations and vortex shedding in backward-facing step flows: Simulation and linear instability analysis. *Physics in Fluids*, 16:3361.

Weiss, P. and Deck, S. (2011). Control of the antisymmetric mode (m= 1) for high reynolds axisymmetric turbulent separating/reattaching flows. *Physics of Fluids*, 23:095102.

Weiss, P., Deck, S., Robinet, J., and Sagaut, P. (2009). On the dynamics of axisymmetric turbulent separating/reattaching flows. *Physics in Fluids*, 21.

White, F. (2006). *Viscous Fluid Flow (Third Edition)*. McGraw-Hill Education.

Wong, H., Meijer, J., and Schwane, R. (2005). Experimental and theoretical investigation of base-flow buffeting on ariane 5. In *41 st AIAA/ASME/SAE/ASEE Joint Propulsion Conference & Exhibit*, pages 1–10.